

Table of Contents

Table of Contents	v
List of Figures	vii
Acknowledgments.....	ix
Chapter 1. Introduction.....	10
A. Apologia without apology: Rationale for studying third sound in superfluid ^3He ..	10
B. Outline	11
Chapter 2. Superfluidity in ^3He	12
A. The superfluid phase transition in ^3He	12
B. Fundamentals of the Ginzburg-Landau theory of the superfluid phase transition...	17
C. The BCS theory applied to superfluid ^3He	19
D. The Ginzburg-Landau theory applied to superfluid ^3He	24
E. Phase diagrams for superfluid ^3He	28
F. Experiments on superfluid ^3He in restricted geometries.....	30
G. Potential for future ^3He physics	34
Chapter 3. Third Sound in ^4He	35
A. Superfluidity and two-fluid hydrodynamics	35
B. Third sound	37
C. Other 'sounds' of superfluid helium.....	37
D. Third sound in ^4He and ^3He	40
Chapter 4. Experimental Design	41
A. Experimental cell	41
i. Overview	41
ii. Substrate.....	44
iii. Capacitor plates	44
iv. Capacitive level detector: bulk liquid height and film thickness.....	45
v. Excitation method.....	46
vi. Capacitive detection method	49
B. Cryogenics and thermometry.....	53
Chapter 5. Hydrodynamics of Third Sound in ^3He	56
A. Wave equation and speed of third sound waves	56
B. Standing waves, boundary conditions, and resonant frequencies.....	59
C. Model of film response.....	63

Chapter 6. Experimental Results.....	68
A. Third sound spectra in superfluid ^4He	68
i. First experiment with ^4He films	68
ii. Second experiment with ^4He films	73
B. Film thickness vs height of the bulk liquid.....	73
C. Resonant spectra of third sound in superfluid ^3He	81
i. Method for obtaining third sound spectra.....	81
ii. Third sound spectra	83
Chapter 7. Analysis of Third Sound Resonance Spectra	90
A. Interpretation of third sound spectra as Bessel modes	90
B. Calculation of third sound speed from spectra	97
C. Calculation of superfluid density fraction	97
D. Damping of third sound resonances	103
Chapter 8. Future Directions for Third Sound Research.....	110
A. Enhance ^3He superfluidity with a ^4He coating of the substrate.....	110
B. Swirling ^3He to observe 2D vortices.	116
Bibliography	118
Appendix A. G.E. Volovik's ^3He Heliocentric Universe.....	128
Appendix B. Mathcad model calculation	129

List of Figures

Chapter 2. Superfluidity in ^3He	12
Figure 2.1 The superfluid phase transition in ^3He	13
Figure 2.2 First evidence of $^3\text{He-A}$ and $^3\text{He-B}$ phase transitions	14
Figure 2.3a The low-temperature phase diagram for superfluid ^3He	15
Figure 2.3b P-T-H phase diagram for superfluid ^3He	16
Figure 2.4 Order parameter suppression by a wall	27
Figure 2.5 The suppression of T_c^{film} from T_c^{bulk} vs film thickness	29
Figure 2.6 The phase diagrams for films or slabs of liquid ^3He	31
Chapter 3. Third Sound in ^4He	35
Figure 3.1 The Andronikashvili experiment	36
Figure 3.2 A third sound wave on a substrate	38
Chapter 4. Experimental Design	41
Figure 4.1 Scale drawing of the experimental cell	42
Figure 4.2 Not-to-scale drawing of the experimental cell.....	43
Figure 4.3 Sketch of the volume changer apparatus.....	47
Figure 4.4 Schematic of electronics.....	50
Figure 4.5 Schematic of a symmetric AC capacitance bridge.....	52
Chapter 5. Hydrodynamics of Third Sound in ^3He	56
Figure 5.1 Bessel mode profiles for fixed boundary.....	60
Figure 5.2 Bessel mode profiles for free boundary.....	62
Figure 5.3 Shapes of modes corresponding to the indices (m,n).....	64
Figure 5.4 Sample spectra generated from the model.....	67
Chapter 6. Experimental Results.....	68
Figure 6.1 Spectra of third sound observed in ^4He films at 1.4 K.....	70
Figure 6.2 c_3^2 vs h in ^4He	72
Figure 6.3 Spectra of ^4He third sound near 10 mK.....	74
Figure 6.4 Comparison of ^3He and ^4He spectra.....	75
Figure 6.5 Sketch of the film - bulk liquid interface.....	77
Figure 6.6 Film thickness vs height from the free surface to the film	80
Figure 6.7a Third sound spectra for films with h = 1.053 mm and h = 0.571 mm.....	85
Figure 6.7b Third sound spectra for films with h = 0.394 mm and h = 0.263 mm	86
Figure 6.7c Third sound spectra for films with h = 0.234 mm and h = 0.137 mm.....	87
Figure 6.7d Third sound spectra for films with h = 0.117 mm and h = 0.087 mm	88
Figure 6.7e Third sound spectra for films with h = 0.058 mm and h = 0.040 mm.....	89

Chapter 7. Analysis of Third Sound Resonance Spectra	90
Figure 7.1 Multi-peak Lorentzian fit to a third sound spectrum	91
Figure 7.2 Mode-plots for the thinnest film	94
Figure 7.3 Mode-plots for films with $h = 0.571$ mm and $h = 0.394$ mm	95
Figure 7.4 Mode-plots for films with $h = 0.117$ mm and $h = 0.087$ mm	96
Figure 7.5 The speed of third sound in ^3He	98
Figure 7.6a The superfluid density calculated using $h = H_{\text{filling}} - H$	100
Figure 7.6b The superfluid density calculated using $h' = h + 30 \mu\text{m}$	101
Figure 7.7 Superfluid density and G-L curves	102
Figure 7.8 Linewidths Δf of the α_{01} mode as a function of temperature	104
Figure 7.9 Quality factors Q of the α_{01} mode as a function of temperature	105
Figure 7.10 Data and 'calculation' of second viscosity damping.....	108
Chapter 8. Future Directions for Third Sound Research.....	110
Figure 8.1 Third sound spectra with and without ^4He coating	112
Figure 8.2 c_3 and ρ_s with and without ^4He coating	113
Figure 8.3 Spectra with ^4He coating for a thinner film.....	114
Figure 8.4 Superfluid transition temperature as a function of film thickness	115
Figure 8.5 Swirling experiment	117

Acknowledgments

First of all, I'd like to thank my advisor S³amus Davis, a brilliant physicist and eternal optimist, for holding the beacon high even when the path swerved downward. The success of this project is in no small way due to his patience, persistence, and enthusiasm. It is also due to the financial support of the NSF and ONR, of course.

I'd like to thank all the members of the Davis Group for the laughter and wisdom that was shared around. Kristine Lang and Shuheng Pan are excellent sources of both. I'd especially like to thank two of my close colleagues, the early members of the Davis Group: Ray Simmonds, a California dude turned true scientist, and Eric Hudson, a prince among men. Ray was instrumental in building (and re-building!) the third sound cell and is always game for anything. Eric and I spent many an hour in discussion in front of white-boards, and perhaps even longer in friendly combat on the racquetball court. I hope to continue both in the future. And I also hope that research on third sound presses on from this beginning, with Joan Hoffmann and Konstantin Penanen carrying the torch.

Richard Packard was kind enough to loan me not one, but two dilution refrigerators over the last few years (which I returned in good condition, of course); he also lent me some keen perspective which shot unerringly at the research problems facing me. It has been a pleasure interacting with his entire research group, especially Niels Bruckner, Alosha Marchenkov, Keith Schwab, Scott Backhaus, and Alex Loshak.

Outside of the basement of Birge, I'm incredibly grateful to my family for everything they have done for me, more than I can possibly express in the few minutes before I turn in this dissertation. I hope that, if they found the Nature paper baffling and incomprehensible, this will be sufficient to leave them merely puzzled.

And Sarah, who makes it all worthwhile.

Chapter 1. Introduction

A. Apologia without apology: Rationale for studying third sound in superfluid ^3He

^3He is the most complex material in physics for which a successful theory exists. The theory of ^3He [see Vollhardt and Wolfle 1990] rivals the Standard Model of elementary particle physics in its richness, meaning that ^3He can display an enormous range of physical phenomena, both unique to ^3He and analogous to other phenomena across the spectrum of physics [see Appendix A].

The superfluid transition in liquid ^3He was discovered in 1972 by Osheroff, Lee, and Richardson, [Osheroff 1972] instantly making ^3He the prototype system for studying anisotropic superfluidity. The previously discovered superfluids, liquid ^4He below 2.2 K and metallic superconductors (Hg, Pb, Nb, W, Al, etc), are isotropic, in that they can be described well by a macroscopic wave-function Ψ which is an isotropic scalar. In contrast, the wave-function needed to describe superfluid ^3He is anisotropic, possessing additional internal degrees of freedom. Since this aspect of superfluid ^3He was discovered, related forms of anisotropy have been suggested to describe other very different systems, from the nuclear matter forming the core of neutron stars [Hoffberg *et al.* 1970] and [Pines and Alpar 1985] to high- T_c cuprate superconductors [Van Harlingen 1995], [see Vollhardt and Wolfle 1990 p.21-22].

Due to its complex internal structure, superfluid ^3He is capable of displaying a very wide array of physical phenomena which have been observed in other condensed matter systems. For example, the Josephson junction [Tilley and Tilley 1986] and [Poole *et al.* 1995], a phenomena of fundamental interest first seen in tunneling between superconductors and now widely used as a sensitive probe of magnetic flux, has recently been demonstrated in superfluid ^3He [Pereverzev *et al.* 1997]. The direct mathematical analogy between the behavior of vortices in superfluid ^3He and hypothesized cosmic strings has allowed researchers to study the formation of these strings in the early universe while working in a low-temperature laboratory [Bauerle, *et al.* 1998]. The internal structure of ^3He 's superfluid state has suggested other possibilities which are now being explored: measuring a Hall current in films of ^3He [Mermin, Muzikar 1980], and searching for the analog of the quantum Hall effect [Volovik 1988, 1989].

When superfluid ^3He is placed in a confined geometry, particularly interesting questions arising from size effects [Freeman 1988] can be addressed. The relevant length scale for a superfluid is determined by its coherence length $\xi(T)$; for the wave-function to vary in magnitude over distances shorter than $\xi(T)$ is energetically unfavorable. In the case of superfluid ^4He , $\xi(T) \sim 1 \text{ \AA}$, which makes the physical dimensions of virtually any sample very large compared to the coherence length. In contrast, the coherence length for superfluid ^3He is $\xi \sim 65 \text{ nm}$ at $T = 0$, and increases as T increases. So, it is quite feasible to create films, slabs, cylinders, or other confined geometry systems where the sample size is actually comparable to or smaller than the coherence length of the superfluid. This has allowed researchers to study "2-dimensional behavior" in superfluid ^3He films, and it has suggested the possibility of observing the quintessential 2-D phase transition, the Kosterlitz-Thouless phase transition [Kosterlitz, Thouless 1973] and [Nelson, Kosterlitz 1977], in ^3He [Kurihara 1983].

A variety of tools has been used to study films or slabs of superfluid ^3He , including self-emptying beakers [Sachrajda *et al.* 1985], torsional oscillators [Xu and Crooker 1990], and NMR [Freeman *et al.* 1988]. In this thesis, I present a new tool for use in studying films of superfluid ^3He which has already proven extremely useful in studies of superfluid ^4He . 'Third sound' is the name given to waves which propagate along the free surface of a superfluid film. The behavior of these waves reveals the superfluid properties of the film; for example, the speed c_3 of the waves depends on the superfluid density, ρ_s , which is a critical thermodynamic parameter of the film. We have been able to observe third sound in superfluid ^3He films for the first time. We have measured some of its properties [Schechter *et al.* 1998], for film thicknesses ranging from 90 to 280 nm and for temperatures from $T/T_c^{\text{bulk}} = 0.92$ down to $T/T_c^{\text{bulk}} = 0.35$, where $T_c^{\text{bulk}} = 0.93$ mK is the transition temperature for bulk ^3He . We expect to be able to use third sound as a tool to study a variety of physical phenomena in the near future.

B. Outline

Chapter 2 of this thesis discusses superfluid ^3He , its basic properties, the highly successful Bardeen-Cooper-Schrieffer and Ginzburg-Landau theories, and previous experiments on superfluid ^3He in restricted geometries. Chapter 3 introduces the phenomenon known as third sound, discusses it in the context of other hydrodynamic 'sounds', and reviews its history and uses in superfluid ^4He films. Chapter 4 describes the experimental apparatus which we designed and built to detect third sound waves. Chapter 5 derives the governing equation for third sound waves in ^3He , discusses the standing wave solutions of that equation, and presents a model for the spectra of third sound resonances we measured. Chapter 6 describes the experimental results we obtained. It first describes several initial diagnostic tests of the apparatus carried out with films of superfluid ^4He , then shows our measurements of the film thickness compared to the height of the saturated film above the surface of the bulk liquid, and finally presents the spectra of third sound resonances we observed. Chapter 7 interprets the observed spectra, deducing the speed of third sound and the average superfluid density of the film, and discusses the damping observed in the spectra. Finally, Chapter 8 briefly discusses our efforts to enhance the superfluidity by applying a coating of ^4He to the film's substrate and describes a promising experiment which the existence of third sound should allow us to carry out.

Chapter 2. Superfluidity in ^3He

In this Chapter, we discuss the current state of our knowledge concerning superfluidity in ^3He . We describe the fundamentals of the Ginzburg-Landau (GL) theory of phase transitions and the Bardeen-Cooper-Schrieffer (BCS) theory of superconductivity, and we discuss their application to the case of liquid ^3He . We discuss the different possible superfluid phases made available to ^3He by its 18-component order parameter, and the phase diagrams which result. Finally, we discuss the effects which occur when liquid ^3He is confined to a restricted geometry and describe the previous experiments which have explored this issue.

A. The superfluid phase transition in ^3He

The "high temperature" phase diagram for ^3He is shown in Figure 2.1. ^3He has the lowest normal boiling point of any known substance, at 3.19 K, and like its fellow isotope ^4He , it remains a liquid at saturated vapor pressure all the way down to absolute zero. Some 30 atm of pressure are required to force ^3He into a solid phase. This remarkable property is due to the low mass of the helium atoms, and due to the extreme weakness of the forces binding the atoms together. Since ^3He atoms are neutral, with 2 electrons in a closed shell, they do not bond ionically or covalently; the inter-atomic attraction is due principally to the van der Waals force and the hard-core repulsion of the helium ions [*see* Tilley and Tilley 1986]. The minimum energy configuration spaces the helium atoms about 3 angstroms apart, and this energy minima has a depth of about 10 K. (There is also an even weaker interaction between the magnetic dipoles of the nuclear spins, but this has a strength of only about 10^{-7} K at a separation of 3 angstroms and can be neglected for our purposes.) [Swift 1980]

In 1972, Osheroff, Richardson, and Lee observed the signatures of two phase transitions between the normal liquid state of ^3He and what would turn out to be two superfluid phases of ^3He [*see* Osheroff 1997]. Their experiment studied a mixture of liquid and solid ^3He at the melting pressure in a Pomeranchuk cell, which is designed to lower or raise the temperature by compressing or expanding the volume of the cell [Richardson 1997]. As they lowered the temperature, the pressure changed smoothly except for two kinks, the first at 2.65 mK and the second at 1.8 mK; reversing direction, the two kinks were seen again as the cell was warmed through the same temperatures, as shown in Figure 2.2. With further experiments, they were able to show that these kinks represented phase transitions occurring in the liquid as it transformed from a normal Fermi liquid first to the superfluid ^3He -A state and then to the superfluid ^3He -B state. The "low-temperature" phase diagram for ^3He is shown in Figure 2.3a with no applied magnetic field and in Figure 2.3b as a function of T, P, and H. [*see* Lee 1997]

The experiments described in this thesis study a film of superfluid ^3He , which is necessarily at zero pressure due to its free surface, and without an applied magnetic field. However, it is worth examining the complete superfluid phase diagram because confinement of the ^3He within thin slabs (the size of our films) is known to produce a phase diagram with features reminiscent to the effect of a magnet field [Li and Ho 1988]. We will later discuss this phase diagram in detail. For now, it is sufficient to emphasize

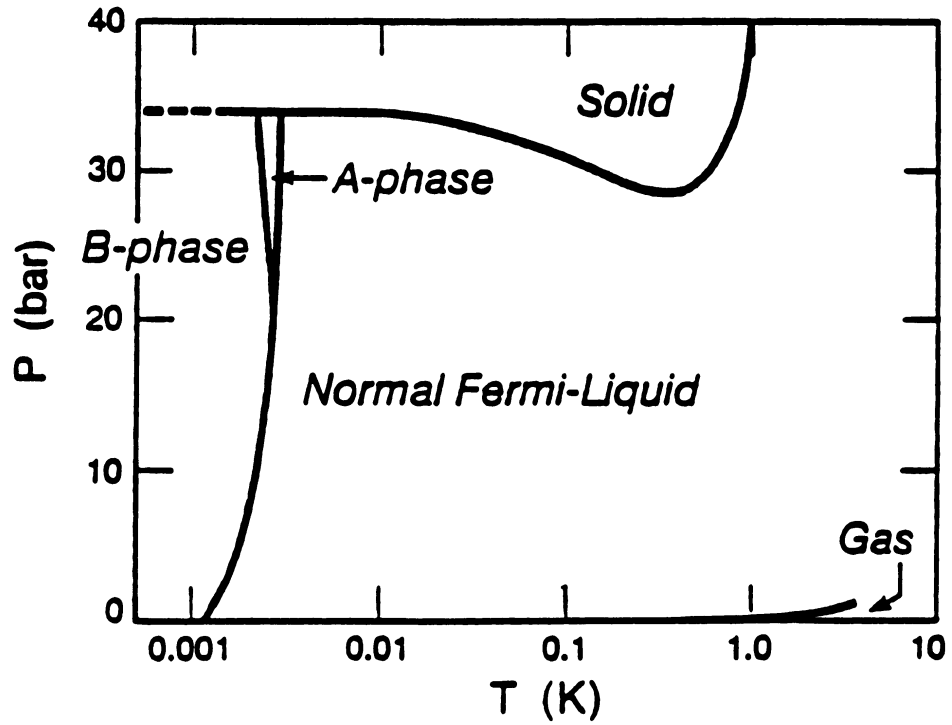


Figure 2.1 Phase diagram for ^3He . ^3He becomes a liquid at 3.19 K at vapor pressure. About 30 bar applied pressure is necessary to solidify ^3He , even at absolute zero. With less pressure applied, below about 3 mK, ^3He becomes a superfluid. [from Swift 1980]

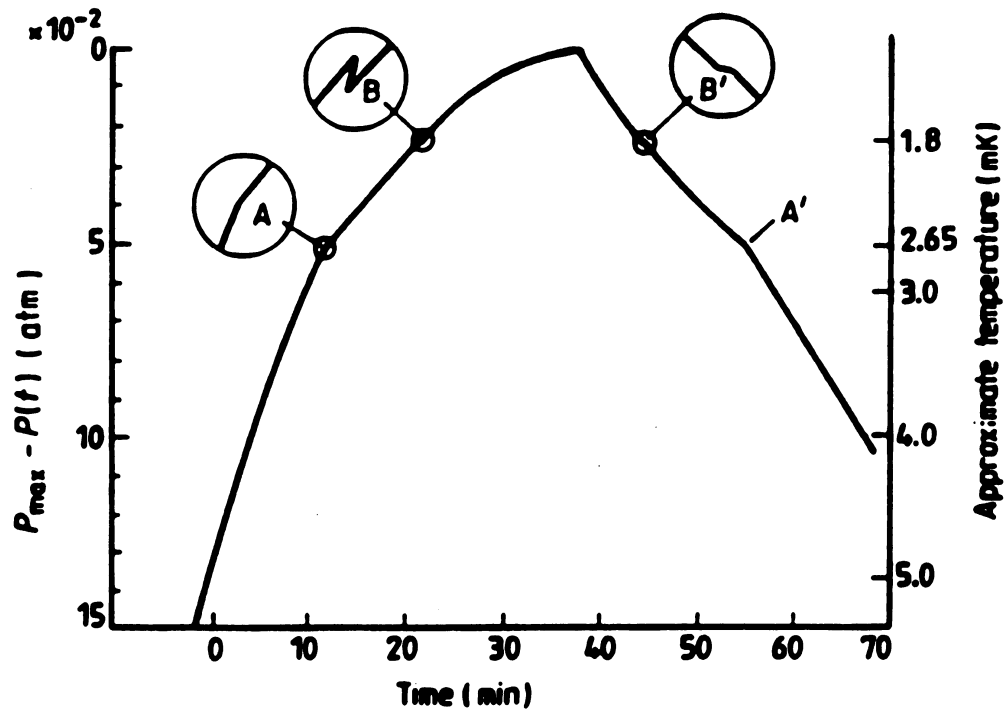


Figure 2.2 First evidence of $^3\text{He-A}$ and $^3\text{He-B}$ phase transitions. Experimental data showing the first evidence for the superfluid transitions in ^3He , found by Osheroff, Richardson and Lee in 1972 [from Osheroff *et al.* 1972]. The ^3He was compressed for the first 40 minutes, causing the temperature to fall, and then the process was reversed. The kinks in the curve, at the same temperatures during cooling and warming, are indicative of phase transitions in the material. A and A' show transitions from the normal Fermi liquid into the A-phase and back; B and B' show transitions from the A-phase to B-phase and back.

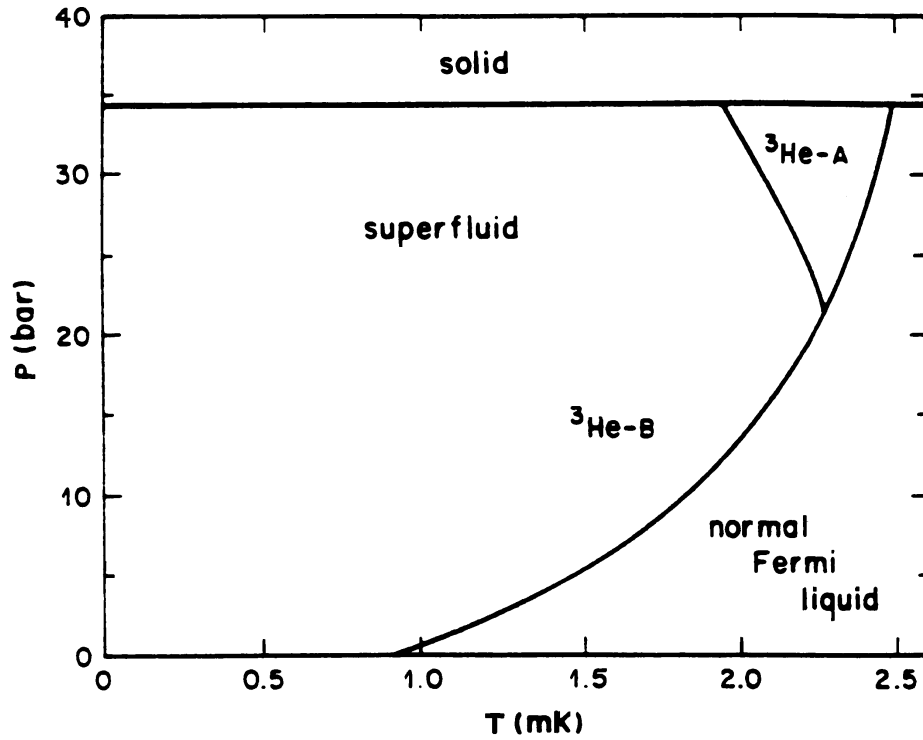


Figure 2.3a The low-temperature phase diagram for superfluid ^3He . Above 34 bar ^3He solidifies. Above 0.93 mK at zero pressure, ^3He is a normal liquid which obeys the Fermi liquid theory. There are two different superfluid states, the A-phase and the B-phase, which are each stable for some range of temperature and pressure. [from Greywall 1986 and Zieve 1992]

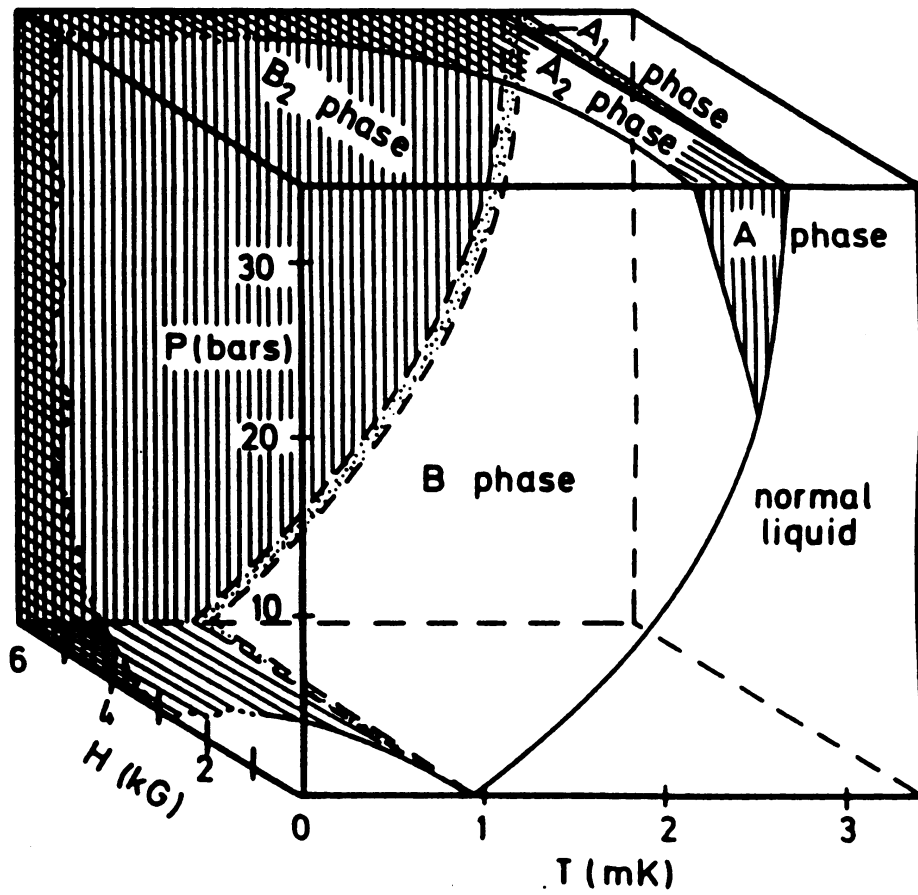


Figure 2.3b P-T-H phase diagram for superfluid ^3He . A large magnetic field increases the stability of an A-like phase at lower temperatures and pressures. [from Zieve 1992]

the fundamental fact that in zero magnetic field and at zero pressure, bulk liquid ^3He undergoes a phase transition to the superfluid $^3\text{He-B}$ state at about 0.93 mK. We will refer to as this temperature as T_c^{bulk} or simply T_c .

B. Fundamentals of the Ginzburg-Landau theory of the superfluid phase transition

Superfluidity, both for the helium isotopes and for superconductors, is a macroscopic phenomenon which is nonetheless fundamentally quantum-mechanical. A superfluid can be described as possessing a single, macroscopic wave-function $\Psi(\mathbf{r})$, analogous to the microscopic wave-functions of quantum mechanics. This wave-function can be derived from the detailed microscopic theory of the superfluid, but it can also be productively viewed from a purely macroscopic standpoint, using the phenomenological approach invented by Ginzburg and Landau [*see* Lee and Richardson 1978]. The idea, sometimes called the Landau theory of phase transitions, applies to any material transition from a disordered state to an ordered state, such as occurs in a ferromagnet at the Curie temperature. It hypothesizes that the material undergoing a phase transition can be well-described by a single "order parameter", which characterizes the alignment, or ordering, or "lack of entropy" of the system. This could be the magnetization M in a ferromagnet, the polarization P in a ferroelectric crystal, or the density in a boiling liquid. Above the transition temperature, T_c , the order parameter is zero or small; for example, above the Curie temperature, the individual spins in an iron bar are randomly oriented and the net magnetization vanishes, $M = 0$. However, below T_c the order parameter takes on a non-zero value which characterizes the macroscopic state of the system. Ginzburg and Landau suggested that the wave-function $\Psi(\mathbf{r})$, with $|\Psi(\mathbf{r})|^2$ being the local density of superconducting electrons or superfluid atoms, could be treated as the order parameter for the superfluid phase transition.

Having chosen an order parameter for the system, the Ginzburg-Landau approach then minimizes the free energy of the system in terms of this parameter. This determines the state of the system as a function of temperature (and any other variables), and it can yield a number of intuitive insights into nature of the phase transition and the behavior of the material. Terms can be included in the free energy which account for the variation of the order parameter through the material, and for the presence of magnetic fields or supercurrents. These terms can define length scales over which the order parameter can vary without a prohibitive energy cost, or they can determine the 'critical' fields or currents which are sufficient to quench the order parameter completely.

As an example, let us review how the Ginzburg-Landau theory is applied to a metallic superconductor; we will deal with the more complex application to superfluid ^3He shortly. In a superconductor like mercury, aluminum, or niobium, which are well-described by the Bardeen-Cooper-Schrieffer (BCS) theory, the order parameter is a complex scalar which can be written $\Psi(\mathbf{r}) = |\Delta|e^{i\phi}$. From the microscopic viewpoint of the BCS theory, superconductivity exists due to the pairing of electrons into Cooper pairs which form a ground state with lower energy than the normal state. An energy gap then separates the Cooper pairs from any available excited quasi-particle states. The amplitude of the order parameter, $|\Delta|$, is just the magnitude of this energy gap; it vanishes above T_c , and below T_c it characterizes the ordering present in the superconducting state.

From the macroscopic Ginzburg-Landau viewpoint, however, this microscopic interpretation is unnecessary. The order parameter's amplitude squared, $|\Psi(r)|^2 = |\Delta|^2$, is simply taken as the local density of superconducting electrons or superfluid atoms, while the gradient of the order parameter's phase, $\nabla\phi$, turns out to be responsible for supercurrents within the material. (The difference in the phase ϕ between two weakly touching superconductors is responsible for the Josephson tunneling current; these Josephson junctions are used to make SQUIDS, superconducting quantum interference devices, which are extremely sensitive magnetometers.) These microscopic and macroscopic viewpoints must yield the same results: in 1959 Gor'kov rigorously derived the Ginzburg-Landau formulation from the microscopic equations of the BCS theory [Gor'kov 1959].

Ginzburg and Landau express the free energy near T_c as a functional of the order parameter and minimize it. The free energy includes terms proportional to powers of $|\Psi|^2$, a term proportional to $|\nabla\Psi|^2$ to account for spatial variation of the order parameter, and other terms involving the presence of magnetic fields [see Poole *et al.* 1995 p.123]. For this discussion, we will ignore magnetic fields and write down the free energy as:

$$F = F_n - \alpha(T) |\Psi|^2 + \frac{1}{2}\beta |\Psi|^4 + \gamma |\nabla\Psi|^2 \quad (2.1)$$

Near T_c , we take $\alpha(T) = \alpha_0 (1-T/T_c)$ and $\beta = \text{constant}$ (these temperature dependencies can be justified by appealing to the microscopic theory, or taken as postulates to be borne out by the results). Let us examine three cases: first, the bulk case inside a superconductor; second, the situation near a wall of the superconductor where the order parameter vanishes; and third, a supercurrent flowing through the material.

Within the bulk, the gradient of the order parameter is zero, and the phase of the wave-function plays no role. Minimizing the free energy with respect to $|\Psi|^2$, we obtain

$$dF/d|\Psi|^2 = -\alpha(T) + \beta |\Psi|^2 = 0 \quad (2.2)$$

or

$$|\Psi|^2 = \alpha(T)/\beta = (\alpha_0/\beta) (1-T/T_c) \text{ when } T < T_c \quad (2.3)$$

Above T_c , the free energy is minimized when $\Psi = 0$; this means there are no superconducting electrons so the material behaves as a normal metal. When T falls below T_c , a second order phase transition occurs, with Ψ rising continuously from zero according to $\Psi = \sqrt{\{(\alpha_0/\beta) (1-T/T_c)\}}$. The density of superconducting electrons, $n_s = |\Psi|^2 \sim (1-T/T_c)$ rises linearly as the temperature falls below the transition.

Near a wall (abutting either vacuum or a non-superconducting material), the density of superconducting electrons must fall to zero, which means the order parameter must have a non-zero gradient. We can see the length scale over which the order parameter changes near the wall (let x be the direction perpendicular to the wall) by making a change of variables:

$$\psi = \sqrt{\{\beta/\alpha(T)\}} \Psi \quad (2.4)$$

is the wave-function normalized to its bulk value,

$$\eta = x/\xi(T) \quad (2.5)$$

where $\xi(T) = \sqrt{(\gamma/\alpha(T))}$ is a dimensionless length, and

$$f = F/F_0 \quad (2.6)$$

where $F_0 = \alpha(T)^2/\beta$ is the reduced free energy. The expression for the reduced free energy becomes

$$f = |d\psi/d\eta|^2 - |\psi|^2 + 1/2 |\psi|^4 \quad (2.7)$$

It should be clear that the length scale over which the wave-function can vary is given by $\xi(T) = \sqrt{\{\gamma/\alpha(T)\}}$, which is called the coherence length, or healing length, of the superconductor. (If this is not clear, it is easy to show this explicitly: minimizing this functional with respect to ψ^* (or ψ) using the Euler-Lagrange equation yields $d^2\psi/d\eta^2 + \psi(1-|\psi|^2) = 0$, which has the exact solution $\psi = \tanh\{x/\xi(T)\sqrt{2}\}$.) The Ginzburg-Landau approach makes the physical meaning of the coherence length $\xi(T)$ crystal clear: it is the length over which the order parameter can vary without incurring too great an energetic penalty from the kinetic energy term in the free energy. Note that $\gamma = \text{constant}$ near T_c , so the coherence length diverges as $(1-T/T_c)^{-1/2}$ as the temperature approaches T_c from below. The length scale for the wave-function to change becomes longer and longer as we near T_c ; equivalently, the region near a wall which has a reduced density of super-electrons gets larger and larger as we approach T_c from below, until it encompasses the entire material at T_c and the superconductor ceases to superconduct.

Finally, a brief comment on supercurrents. The velocity of a supercurrent is proportional to the gradient of the phase of the wave-function. This follows from the quantum-mechanical operator $p = -i\hat{\mathbf{E}}\nabla$ applied to the wave-function (take the magnitude as constant):

$$p\Psi = -i\hat{\mathbf{E}}\nabla\Psi = -i\hat{\mathbf{E}}\nabla(|\Delta|e^{i\phi(r)}) = (\hat{\mathbf{E}}\nabla\phi)\Psi \quad (2.8)$$

So the velocity is just $v_s = (\hat{\mathbf{E}}/m)\nabla\phi$, where m is the mass of the Cooper-paired electrons.

This concludes our basic discussion of the Ginzburg-Landau theory applied to a superconductor with a complex scalar order parameter, $\Psi(r) = |\Delta|e^{i\phi}$. We now discuss the more complex case of superfluid ^3He , which requires a more highly-structured order parameter to adequately describe its superfluid phase transitions.

C. The BCS theory applied to superfluid ^3He

Before discussing how the Ginzburg-Landau theory is applied to superfluid ^3He , it is necessary to introduce its anisotropic order parameter. We can best do this by reviewing how the BCS theory is applied to a p-wave superfluid.

The added complexity of superfluid ^3He arises directly from the nature of the Cooper pairs in the system. In a conventional metallic superconductor, the Cooper pairs are formed from two electrons having opposite momenta (with zero net center-of-mass

momentum) and opposite spins. The spatial wave-function of this combined object is symmetric under interchange of the electrons, so the spin wave-function must be the anti-symmetric spin singlet in order to obey Fermi statistics. Thus, the two electrons with $S=1/2$ combine to form the spin singlet $S=0$ state, $|S=0, S_z=0\rangle = (1/\sqrt{2})(|\uparrow\downarrow\rangle - |\downarrow\uparrow\rangle)$. This state is analogous to an ($L=0$) atomic s-orbital, so it is referred to as "s-wave pairing" and the superconductor is said to have "s-wave symmetry".

The ${}^3\text{He}$ atoms which form Cooper pairs are fermions just like the superconducting electrons; however, due principally to the 'hard-core' Pauli repulsion, the spatial wave-function is analogous to that of an atomic p-orbital rather than an atomic s-orbital. (The lobed structure of the p-orbitals avoids the energy cost of pushing the atoms close together and having their electrons overlap.) Since the p-orbital, with $L=1$, is anti-symmetric under interchange of the atoms, the spin state must be symmetric. This requires the two $S=1/2$ ${}^3\text{He}$ atoms to combine into one of the three spin triplet $S=1$ states:

$$\begin{aligned} |S=1, S_z = +1\rangle &= |\uparrow\uparrow\rangle \\ |S=1, S_z = 0\rangle &= (1/\sqrt{2})(|\uparrow\downarrow\rangle + |\downarrow\uparrow\rangle) \\ |S=1, S_z = -1\rangle &= |\downarrow\downarrow\rangle \end{aligned} \quad (2.9)$$

with the usual notation. There are therefore several possibilities for the structure of each Cooper pair: three spatial p-orbitals ($L=1$ has $m_l = +1, 0, -1$ or p_x, p_y, p_z sub-states) and three spin states. This gives a total of nine degrees of freedom (each complex, so actually 18) which must be present in the wave-function of the system. Thus the order parameter for ${}^3\text{He}$ dwarfs that of the superconductor, with its two degrees of freedom (amplitude and phase), and this leads to the diversity of superfluid phases and phenomena which ${}^3\text{He}$ exhibits. As you would expect, ${}^3\text{He}$ is referred to as having "p-wave pairing" or "p-wave symmetry".

In order to apply a Ginzburg-Landau analysis, we need to write down the order parameter in which to expand the free energy. We will first show how the conventional choice is defined in terms of the natural wave-function for the problem, while briefly commenting on the analogous BCS calculations used to obtain the microscopic wave-functions in the s-wave and p-wave cases. Finally, we will write down the Ginzburg-Landau free energy and discuss the values of the order parameter which minimize it.

We can write the wave-function down in the natural (though not most convenient) way, in terms of the three spin states, each having an amplitude which is a function of the spatial coordinate k :

$$\Psi(k) = \Psi_{\uparrow\uparrow}(k) |\uparrow\uparrow\rangle + \Psi_{\downarrow\downarrow}(k) |\downarrow\downarrow\rangle + \Psi_{\uparrow\downarrow}(k) (|\uparrow\downarrow\rangle + |\downarrow\uparrow\rangle) \quad (2.10)$$

It is convenient to condense these amplitudes into a 2x2 spin matrix where the amplitudes for the different spin states become matrix elements (we will see that the BCS s-wave and p-wave equations become analogous when expressed in this fashion):

$$D(k)_{\text{matrix}} = \begin{pmatrix} \Psi_{\uparrow\uparrow}(k) & \Psi_{\uparrow\downarrow}(k) \\ \Psi_{\downarrow\uparrow}(k) & \Psi_{\downarrow\downarrow}(k) \end{pmatrix} \quad (2.11)$$

Just as the wave-function in s-wave BCS theory is the energy gap which opens between the Cooper-pair states and the available quasi-particle excited states, so the components of the wave-function in p-wave BCS theory are the energy gaps associated with each spin state. For an s-wave superconductor, minimization of the microscopic free energy leads to a self-consistent equation for this energy gap [*see* Tilley and Tilley 1986 p.132]

$$\Delta(\mathbf{k}) = - \frac{1}{2} \sum V(\mathbf{k},\mathbf{k}') (\Delta(\mathbf{k}')/E(\mathbf{k}')) \tanh (E(\mathbf{k}')/2k_B T) \quad (2.12)$$

where $V(\mathbf{k},\mathbf{k}')$ is the attractive interaction potential between the electrons which causes the pairing, and $E^2(\mathbf{k}) = \varepsilon^2(\mathbf{k}) + \Delta^2(\mathbf{k})$, where $\varepsilon(\mathbf{k})$ is the energy with respect to the Fermi energy, and $E(\mathbf{k})$ is the energy of an excited quasiparticle. This equation can be solved explicitly for weak coupling ($N(0)V \ll 1$, where $N(0)$ is the density of states at the Fermi surface) at $T = 0$ yielding the BCS $T=0$ energy gap equation:

$$|\Delta| = 2h\omega_D e^{-1/N(0)V} \quad (2.13)$$

where ω_D is the Debye frequency, and at $T \sim T_c$, yielding the BCS critical temperature

$$k_B T_c = 1.14 h\omega_D e^{-1/N(0)V}. \quad (2.14)$$

For a p-wave superfluid, the calculation follows much the same path [*see* Tilley and Tilley 1986 p.348], leading to the self-consistent matrix equation

$$D(\mathbf{k})_{\text{matrix}} = - \frac{1}{2} \sum V(\mathbf{k},\mathbf{k}') (D(\mathbf{k}')_{\text{matrix}}/E(\mathbf{k}')) \tanh (E(\mathbf{k}')/2k_B T) \quad (2.15)$$

which is, however, more difficult to solve directly. (Here $V(\mathbf{k},\mathbf{k}')$ and $E(\mathbf{k}')$ are numbers, while $D(\mathbf{k})_{\text{matrix}}$ is a matrix.) $D(\mathbf{k})$ could be used as the Ginzburg-Landau order parameter, but it is not the most convenient choice. Instead, we introduce two new quantities, each equivalent to $D(\mathbf{k})$, which are mathematically more amenable and help us to understand the nature of the superfluid states which emerge as solutions of this equation. The first is the vector \mathbf{d} , defined by (different authors follow slightly different conventions)

$$\mathbf{d}(\mathbf{k}) = \frac{1}{2} i \sum (\sigma_y \mathbf{s})_{\alpha\beta} \Psi_{\alpha\beta}(\mathbf{k}) \quad (2.16)$$

where $\alpha\beta$ run over the spin states ($\downarrow\uparrow$), and σ_i are the Pauli matrices. The \mathbf{d} vector can be connected to the natural wavefunction Ψ of the superfluid by writing explicitly

$$\begin{aligned} \Psi_{\uparrow\uparrow}(\mathbf{k}) &= -d_x(\mathbf{k}) + id_y(\mathbf{k}) \\ \Psi_{\downarrow\downarrow}(\mathbf{k}) &= d_x(\mathbf{k}) + id_y(\mathbf{k}) \\ \Psi_{\uparrow\downarrow}(\mathbf{k}) &= d_z(\mathbf{k}) \end{aligned} \quad (2.17)$$

The square of the amplitude of the wave-function is $|\Psi|^2 = |\mathbf{d}(\mathbf{k})|^2$, so we can identify $\mathbf{d}(\mathbf{k})$ with the amplitude of a Cooper pair having a certain direction in \mathbf{k} -space. The Cooper pair amplitude, the wave-function of the Cooper pairs, and the energy gap for a p-wave

superfluid are all interwoven, each having multiple components for the different spin and k-space states.

The second quantity which can act as the superfluid order parameter is the matrix \mathbf{A} , which is made up of the components of \mathbf{d} along the different axes in k-space:

$$d_i(\mathbf{k}) = \sum A_{ij} k_j \quad (2.18)$$

Thus the i component in A_{ij} refers to the x, y , and z components of spin, while the j component of A_{ij} refers to the components in k-space. This is obviously equivalent to the \mathbf{d} vector, and it is customary to use \mathbf{A} to express the free energy in the Ginzburg-Landau formulation.

We can gain some more physical insight into these objects, \mathbf{d} and \mathbf{A} , by considering how they relate to the natural components of the p-wave Cooper pairs, the orbital and spin angular momentum vectors \mathbf{L} and \mathbf{S} . It can be shown [see Lee and Richardson 1978 p.317] that $\mathbf{d} \cdot \mathbf{S} = 0$, meaning that the projection of the spin of the Cooper pair onto the \mathbf{d} vector is zero. In contrast, the relative directions of \mathbf{L} and \mathbf{d} are arbitrary, though particular phases will be characterized by their relationship, as we shall see shortly.

We will now consider three different values of the order parameter, each a solution of the p-wave matrix equation and each corresponding to a different phase of superfluid ^3He : the B-phase, the A-phase, and the planar phase. (All of these can be stable phases because the energy of each phase varies as a function of magnetic field, pressure, temperature, and geometry of the superfluid, so for different parts of the phase space different phases will minimize the free energy.)

B-phase. In bulk ^3He , at zero pressure and zero magnetic field, the superfluid transition at T_c^{bulk} changes the liquid from a normal Fermi liquid [see Baym and Pethick 1978] into the so-called B-phase, which is well-described by the Balian-Werthamer (BW) state. The BW state, in its simplest form, has the order parameter:

$$\mathbf{d}(\mathbf{k}) = \Delta \mathbf{k}/|\mathbf{k}| \quad \text{or} \quad \mathbf{A} = \Delta \begin{pmatrix} 1 & 0 & 0 \\ 0 & 1 & 0 \\ 0 & 0 & 1 \end{pmatrix} \quad \begin{array}{l} \Psi_{\uparrow\uparrow}(\mathbf{k}) = \Delta (-k_x + ik_y) \sim Y_{1,-1}(\mathbf{k}) \\ \Psi_{\downarrow\downarrow}(\mathbf{k}) = \Delta (k_x + ik_y) \sim Y_{1,1}(\mathbf{k}) \\ \Psi_{\uparrow\downarrow}(\mathbf{k}) = \Delta k_z \sim Y_{1,0}(\mathbf{k}) \end{array} \quad (2.19)$$

The \mathbf{d} vector does not have a preferred direction in k-space, but instead points radially outward everywhere. If we calculate the amplitude squared for the wave-function, we obtain $|\mathbf{d}(\mathbf{k})|^2 = \Delta^2$ which has no k-dependence. The Cooper pair amplitude and the energy gap are both independent of k. For this reason, the B-phase is referred to as "isotropic". As we will discuss later, the superfluid density of the liquid is also isotropic.

(The B-phase is not completely isotropic, actually. The most general BW state is given by the \mathbf{d} vector above, rotated about an arbitrary axis \mathbf{N} by some angle ϕ . This has no effect on the calculation of the energy gap, it remains isotropic. However, the \mathbf{d} vector everywhere on the Fermi surface will be rotated with respect to the k-space basis, so that the (previously neglected) magnetic dipole interaction between the spins will contribute a term to the free energy which depends on ϕ . This term, $\cos \phi + 2\cos^2 \phi$, has

a minimum for $\cos \phi = 1/4$, or $\phi = 104^\circ$. The axis of rotation, \mathbf{N} , is arbitrary, though \mathbf{N} tends to orient itself in a magnetic field or near a surface. Nonetheless, for most purposes the B-phase can be treated as an isotropic superfluid like ^4He .)

A-phase. If we were to apply 25-30 bar of pressure to the superfluid B-phase near T_c^{bulk} , the liquid would undergo another phase transition to a lower energy state, called the A-phase. The properties of the A-phase are well-described by the Anderson-Brinkman-Morel (ABM) solution of the p-wave matrix equation. The order parameter of the ABM state takes the form:

$$\mathbf{d}(\mathbf{k}) = \Delta (k_x + ik_y) \mathbf{x}, \quad \mathbf{A} = \Delta \begin{pmatrix} 1 & i & 0 \\ 0 & 0 & 0 \\ 0 & 0 & 0 \end{pmatrix} \text{ or } \begin{array}{l} \Psi_{\uparrow\uparrow}(\mathbf{k}) = -\Delta (k_x + ik_y) \sim Y_{1,1}(\mathbf{k}) \\ \Psi_{\downarrow\downarrow}(\mathbf{k}) = \Delta (k_x + ik_y) \sim Y_{1,1}(\mathbf{k}) \\ \Psi_{\uparrow\downarrow}(\mathbf{k}) = 0 \sim 0 \end{array} \quad (2.20)$$

So for the A-phase, the \mathbf{d} -vector does have a preferred direction, pointing along one axis (here the x-axis) in k-space everywhere. This means that when we calculate the amplitude squared for the wave-function, it will have the form $|\mathbf{d}(\mathbf{k})|^2 = \Delta^2 (k_x^2 + k_y^2)$ with a node along the k_z axis, at $k_x = k_y = 0$. No Cooper pairs will exist at this point in k-space, and the order parameter and energy gap will vanish. This means that there will be excited quasi-particle states which are not separated from the Cooper pair condensate states by a gap, resulting in a heat capacity $C_A \sim T^3$, in contrast to the B-phase heat capacity $C_B \sim e^{-\Delta/kT}$ due to the B-phase's isotropic energy gap.

For this reason the A-phase is referred to as an "anisotropic" superfluid phase. This anisotropy is revealed in the spin-space as well. In the B-phase, all three components of the spin are incorporated into the wave-function, $\Psi_{\uparrow\uparrow}$, $\Psi_{\downarrow\downarrow}$, and $\Psi_{\uparrow\downarrow}$. In the A-phase, only the two components $\Psi_{\uparrow\uparrow}$ and $\Psi_{\downarrow\downarrow}$ are present, and they each have the same k-space dependence (up to a sign). This means that each spin-state is an eigenvector of the angular momentum L_z operator with the same eigenstate, so the superfluid possesses a net angular momentum vector \mathbf{l} , which the B-phase superfluid did not. This vector \mathbf{l} lies along the preferred axis in k-space, k_z ; the \mathbf{d} vector can, but does not necessarily, lie parallel to \mathbf{l} .

Finally, we note that the superfluid density in the A-phase is anisotropic. (We will write down the expression for the superfluid density tensor in the next section.) This will be the case for the planar phase as well, and we expect it to be the case in the thin superfluid ^3He films which we have studied. The meaning of the superfluid density anisotropy is that superflow parallel to \mathbf{l} and superflow perpendicular to \mathbf{l} will occur at different rates, governed by the different components of the superfluid density tensor. This effect will be relevant to our discussion of third sound, since these surface waves are created by fluid moving parallel to the substrate.

Planar phase. If we were to confine the ^3He inside a slab or film, or consider the liquid only very close to a wall, the structure of the superfluid changes, which is reflected in the change of the order parameter:

$$\begin{aligned}
\mathbf{d}(\mathbf{k}) = \Delta(k_x \mathbf{x} + k_y \mathbf{y}) \quad \mathbf{A} = \Delta \begin{pmatrix} 1 & 0 & 0 \\ 0 & 1 & 0 \\ 0 & 0 & 0 \end{pmatrix} & \quad \Psi_{\uparrow\uparrow}(\mathbf{k}) = \Delta(-k_x + ik_y) \sim Y_{1,-1}(\mathbf{k}) \\
& \quad \Psi_{\downarrow\downarrow}(\mathbf{k}) = \Delta(k_x + ik_y) \sim Y_{1,1}(\mathbf{k}) \\
& \quad \Psi_{\uparrow\downarrow}(\mathbf{k}) = 0 \quad \sim 0
\end{aligned} \tag{2.21}$$

While the \mathbf{A} matrix for this so-called "planar phase" superficially appears to resemble that of the B-phase, in fact the order parameter has a character closer to that of the A-phase. The Cooper pair amplitude $|\mathbf{d}(\mathbf{k})|^2 = \Delta^2 (k_x^2 + k_y^2)$ is the same as for the A-phase, so the energy gap has the same structure; in particular it has a node along the k_z axis. This occurs due to the suppression of the $\Psi_{\uparrow\downarrow}(\mathbf{k})$ component of the wave-function. However, unlike the A-phase, the two surviving spin states have opposite orbital angular momentum eigenvalues, $L_z = +1$ or -1 , so there is not necessarily a net orbital angular momentum vector.

D. The Ginzburg-Landau theory applied to superfluid ^3He

We can now combine the two formal structures we have discussed above, adapting the s-wave Ginzburg-Landau theory to the p-wave order parameter \mathbf{A} of superfluid ^3He [see Lee and Richardson 1978]. The expression for the free energy analogous to equation (2.1) is:

$$\begin{aligned}
F = -\alpha(T) A_{i\mu}^* A_{i\mu} + \beta_1 A_{i\mu}^* A_{i\mu}^* A_{j\nu} A_{j\nu} + \beta_2 A_{i\mu}^* A_{i\mu} A_{j\nu}^* A_{j\nu} + \beta_3 A_{i\mu} A_{j\nu}^* A_{i\nu} A_{j\mu} \\
+ \beta_4 A_{i\mu} A_{i\nu}^* A_{j\nu} A_{j\mu}^* + \beta_4 A_{i\mu} A_{j\nu}^* A_{i\nu} A_{j\mu}^* + F_{\text{grad}}
\end{aligned} \tag{2.22}$$

or equivalently

$$\begin{aligned}
F = -\alpha(T) \text{Tr} \mathbf{A} \mathbf{A}^\dagger + \beta_1 |\text{Tr} \mathbf{A} \mathbf{A}^T|^2 + \beta_2 (\text{Tr} \mathbf{A} \mathbf{A}^\dagger)^2 + \beta_3 \text{Tr} (\mathbf{A} \mathbf{A}^T) (\mathbf{A} \mathbf{A}^T)^* \\
+ \beta_4 \text{Tr} \mathbf{A} \mathbf{A}^\dagger \mathbf{A} \mathbf{A}^\dagger + \beta_3 \text{Tr} (\mathbf{A} \mathbf{A}^\dagger) (\mathbf{A} \mathbf{A}^\dagger)^* + F_{\text{grad}}
\end{aligned} \tag{2.23}$$

where \mathbf{A}^T is the transpose and \mathbf{A}^\dagger is the Hermitian conjugate of the order parameter. This expression looks more complicated than it is. In fact, it is just the most general 4th order polynomial in \mathbf{A} , subject to the constraints that it must be invariant under multiplication of the order parameter by the phase factor $e^{i\phi}$ and invariant under rotations in spin space and real space (which is a valid restriction so long as we neglect the nuclear dipole interaction). The first condition requires that each term has as many \mathbf{A} 's as \mathbf{A}^* 's. The i index in $A_{i\mu}$ represents spin space, so invariance under rotation of the spin axes is guaranteed by contracting every spin index which appears in any term to form a scalar product. Similarly, the real space indices μ are contracted in each term. This general form can in fact be obtained from the microscopic BCS theory, which also predicts these coefficients:

$$\alpha^{\text{BCS}}(T) = - (1/3) N(0) * (1-T/T_c) \tag{2.24}$$

$$\beta_1^{\text{BCS}} = - (7\zeta(3)/240) N(0) (\pi k_B T_c)^{-2} \tag{2.25}$$

and

$$-\beta_5^{\text{BCS}} = \beta_4^{\text{BCS}} = \beta_3^{\text{BCS}} = \beta_2^{\text{BCS}} = -2\beta_1^{\text{BCS}} \quad (2.26)$$

where $N(0) = k_F^3 / (2\pi^2 v_F p_F)$ is the single spin quasiparticle density of states at the Fermi surface. Note the analogous temperature dependence between these coefficients and those of the s-wave case. These predictions are only appropriate in the 'weak coupling' limit. In superfluid ^3He , the attractive interaction which produces the Cooper pairing is modified by the onset of superfluidity at T_c ; this is much more important effect in ^3He than in conventional superconductors, and gives rise to a 'strongly coupled' superfluid. If we neglect this effect, we are in the 'weakly coupled' or BCS limit. The effects of the strong coupling can be included in the theory as corrections, $\Delta\beta_i$ to the β_i 's [Serene and Rainer 1978].

The form of the gradient term in the free energy also takes on a more complicated form for a p-wave superfluid. Writing $\partial_\mu f = \partial f / \partial x_\mu$, and appealing to the same invariances as above, we can write:

$$F_{\text{grad}} = k_1 \partial_\nu A_{i\nu} \partial_\lambda A_{i\lambda}^* + k_2 \partial_\nu A_{i\lambda} \partial_\nu A_{i\lambda}^* + k_3 \partial_\lambda A_{i\nu} \partial_\nu A_{i\lambda}^* \quad (2.27)$$

Here k_i are three constants which are equal in the limiting case of weak coupling. It has been shown [Ambegaokar *et al.* 1974] that, neglecting certain surface terms in an integration by parts (which is interestingly not always valid) this expression can be written in the appealing form:

$$F_{\text{grad}}' = K_L |\tilde{\mathbf{N}} \times \mathbf{A}_i|^2 + K_T |\tilde{\mathbf{N}} \cdot \mathbf{A}_i|^2 \quad (2.28)$$

Here $K_L = 2(K_1 + K_2 + K_3)$ and $K_T = 2K_2$ are the longitudinal and transverse stiffness coefficients and \mathbf{A}_i is the vector in real space with components $A_{i\mu}$. Just as we defined a coherence length $\xi = \sqrt{(\gamma/\alpha)}$ in the s-wave case, we can define two coherence lengths in the p-wave case:

$$\xi_L^2(T) = K_L/\alpha = (9/5) \xi_s^2 / (1-T/T_c) \quad (2.29)$$

$$\xi_T^2(T) = K_T/\alpha = (3/5) \xi_s^2 / (1-T/T_c) \quad (2.30)$$

where ξ_s is the $T = 0$ coherence length in the s-wave BCS case,

$$\xi_s = \sqrt{\{7\zeta(3)/48\}} (\mathbf{E}_{vF}/\pi k_B T_c) = 65 \text{ nm} \quad (2.31)$$

at zero pressure. Again as in the s-wave case, these lengths provide the distance scale over which the order parameter can vary without incurring a substantial energy cost from the bending energy terms. The appearance of two different length scales for different components of the order parameter gives a taste of the greater complexity in the p-wave case.

The general expression for the superfluid density tensor in terms of the order parameter is

$$(\mathbf{r}_s)_{ij} = (2m\mathbf{E})^2 [k_1 \text{Tr}(AA^\dagger) \delta_{ij} + (k_2 + k_3) \text{Re}(AA^\dagger)_{ij}] \quad (2.32)$$

where k_i are the coefficients of the bending energy, or gradient term [Xu 1991]. For third sound waves, analogous to long-wavelength surface waves in water, the fluid motion is in the plane parallel to the surface, so the effective superfluid density will be

$$\rho_s = \frac{1}{2} (\mathbf{r}_s)_{xx} + \frac{1}{2} (\mathbf{r}_s)_{yy}. \quad (2.33)$$

It is too difficult in general to minimize the free energy given in equation (2.22), but in certain situations, such as for a film (or slab) or a long cylindrical channel, the order parameter will be simplified by symmetry considerations and the problem becomes tractable. This analysis is discussed in papers by [Jacobsen and Smith 1987], [Pekola *et al.* 1987], and [Fetter and Ullah 1988]. Superfluid densities for these geometries, for both diffuse and specular boundary conditions, are computed by [Li and Ho 1988], who also obtain theoretical phase diagrams based on these calculations for the ^3He as a function of pressure and temperature. For the ^3He -A phase, the average superfluid density of a film is given by

$$\langle \rho_s \rangle = \rho_{s, \text{bulk}}^A 0.6209 (1 - (\pi \xi_T(T)/2d)^2) \quad (2.34)$$

and for thick films

$$\langle \rho_s \rangle = \rho_{s, \text{bulk}}^A (1 - 3.2 \xi_T(T)/2d) \quad (2.35)$$

from the Ginzburg-Landau theory [Freeman 1988]. The second has the simple interpretation that the superfluid density is reduced by the fraction of the film which is within the transverse coherence length $\xi_T(T)$ of the substrate. These expressions are expected to hold only at temperatures close to T_c .

The boundary conditions at the substrate are critical to the understanding of thin films of superfluid ^3He . Ambegaokar, deGennes, and Rainer [Ambegaokar *et al.* 1974] (AGR) discussed the effect of the boundary on the Ginzburg-Landau order parameter. The effect of the boundary is to scatter the quasiparticles which are incident upon it. This scattering can be either specular (preserving momentum transverse to the surface's normal, as a mirror does) or diffuse (again analogous to a mirror). AGR found that for a specularly scattering surface, the transverse component of the order parameter A is unaffected by the presence of the wall, but the perpendicular (longitudinal) component is suppressed to zero at the wall. The length scale over which this component of the order parameter falls from its bulk value to zero is given by $\xi_L(T)$, as is shown in Figure 2.4. For the case of a diffusively reflecting surface, the longitudinal component is again suppressed to zero, and in addition the transverse components are strongly affected as well, over a length scale given by $\xi_T(T)$. The magnitude of the suppression depends closely on the details of the boundary, as can be seen in Buchholtz's study of the ^3He order parameter in contact with a 'randomly rough' wall [Buchholtz 1986].

The suppression of the longitudinal component of the order parameter due to scattering from a boundary (either specular or diffuse), motivates the expectation of a planar-like order parameter for films of superfluid ^3He . In such a system, where the

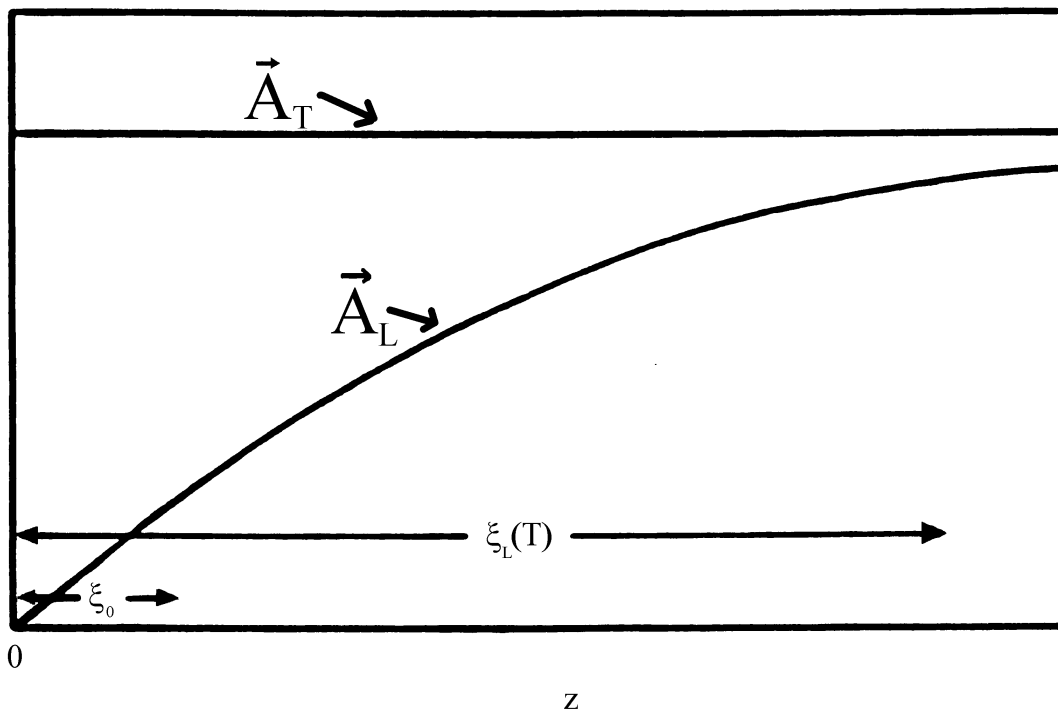


Figure 2.4 Order parameter suppression by a wall. The transverse and longitudinal components of the ^3He order parameter a distance z from a wall, for a specularly scattering surface. The transverse component is unaffected by the wall, the longitudinal component falls to zero over a length scale given by $\xi_L(T)$. [from Ambegaokar, *et al.* 1974]

thickness of the ^3He film is the same order of magnitude as the coherence length, the suppression of the longitudinal component should dominate the physics of the superfluid. For instance, one of AGR's conclusions (for both specular and diffusive boundaries) is that the \mathbf{l} vector of the superfluid is anchored normal to the wall, creating a kind of ferromagnetic ordering which is expected to result in new physics, such as the Volovik-Hall effect [Mermin, Muzikar 1980] and [Volovik 1988a, 1988b, 1989].

Using the approach of AGR, Kjalldman, Kurkijarvi, and Rainer [Kjalldman *et al.* 1978] calculated the transition temperature T_c^{film} as a function of the film thickness, with the results shown in Figure 2.5.

E. Phase diagrams for superfluid ^3He

Due to the many degrees of freedom in its order parameter, ^3He has not just one, but several, stable superfluid phases which have been observed experimentally. These phases have qualitatively different order parameters, energy gaps, and responses to probes, for instance NMR. The phase ^3He prefers depends on the temperature T , the pressure P , and the applied magnetic field H .

In Figure 2.3 we show a sketch of the phase diagram for ^3He , determined by experiment, as a function of temperature and pressure. There are 4 different regions of phase space: solid ^3He , the normal liquid, the $^3\text{He-B}$ phase and the $^3\text{He-A}$ phase.

As we discussed in the introduction, ^3He remains a liquid at its own vapor pressure all the way down to absolute zero, unlike virtually all other materials. However, if we apply a pressure of about 34 bar, we can force ^3He to form a solid, bcc lattice. (Applying more pressure to ~ 100 bar forces it into an hcp lattice.) The function $T(P)$ mapped out by the melting curve is now used as the standard for absolute temperature measurements in the mK range [Pobell 1992 p.214-216].

From 3.2 K down to about 2 mK, ^3He is a normal liquid which is well-described by the Landau theory for Fermi liquids. The Fermi temperature of liquid ^3He is about 1.6 K. At zero pressure, the effective mass of the ^3He quasiparticles is 3.0 times the usual ^3He atomic mass, the Fermi velocity is about 55 m/s, and the Fermi wavelength is about 0.8 nm [Wheatley 1975].

At zero pressure, as the liquid is cooled through the superfluid transition at 0.93 mK, it enters the $^3\text{He-B}$ phase. This superfluid state has equal components of each of the three possible spin states, and each of the three $L=1$ spatial states. This results in an isotropic superfluid; for example, the energy gap Δ has the same magnitude for any excitation, independent of the direction in momentum-space (k -space) of that excitation.

Increasing the temperature and pressure, the liquid can make a transition into the $^3\text{He-A}$ superfluid phase. In contrast to $^3\text{He-B}$, this state is decidedly anisotropic, as we discussed earlier. Its Cooper pairs have only two of the spin components, and only two of the spatial components. This causes the energy gap for excitations to depend strongly on the direction in momentum-space (k -space). In fact, the gap completely vanishes along one axis, which has important consequences for the superfluid's properties affecting, for example, the heat capacity, thermal conductivity, and superfluid density.

The exact phase diagram of films, or slabs, of ^3He is not experimentally known. However, there have been several theoretical and experimental investigations, described

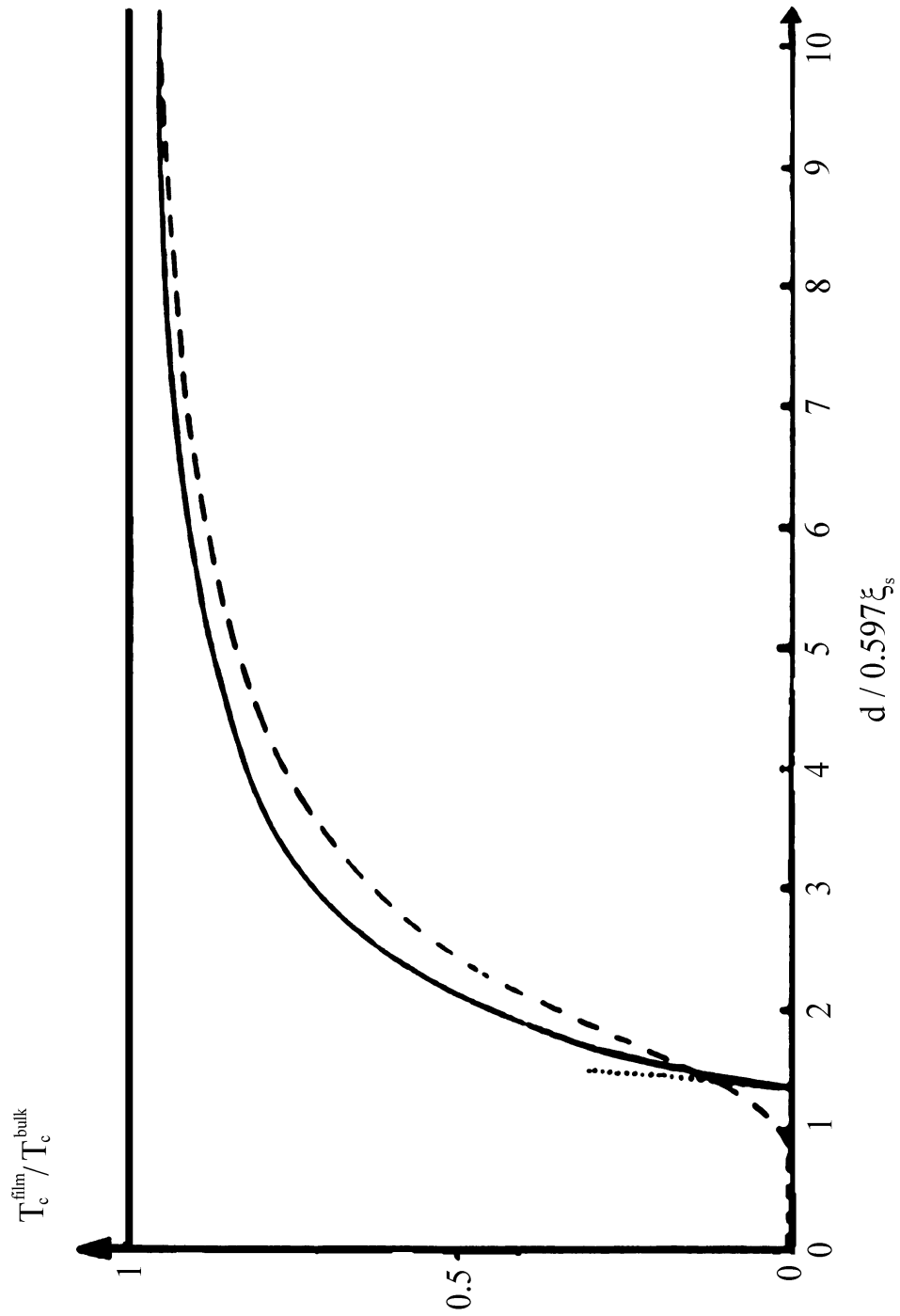


Figure 2.5 The suppression of T_c^{film} from T_c^{bulk} vs film thickness. The film thickness d is given in units of $0.597\xi_s$. The solid line represents the numerical results of [Kjaldman *et al.* 1978]. The dashed line gives asymptotic results in the Ginzburg-Landau range, and the dotted line gives asymptotic results near the critical thickness beneath which superfluidity is quenched.

below, which suggest a phase diagram like that shown in Figure 2.6, which was derived on theoretical grounds by [Li and Ho 1988]. The details of the diagram are expected to vary somewhat depending on the exact boundary condition between the superfluid and the substrate.

As in the case of the bulk liquid, we have a solid phase under pressure, and a normal Fermi liquid above 2 mK. However, below the superfluid transition temperature, we see that the A- and B-phase regions have shifted. For a film of finite thickness, an A-like phase extends all the way down to zero pressure, only giving way to the B-like phase at lower temperatures. This holds for both diffuse and specular boundaries; however, at $P=0$ on a diffusive surface, there should always be an A \rightarrow B phase transition as the temperature is reduced, while a specular surface with thin enough films the A-like phase can be stable down to $T=0$. This is significant for our films, since the existence of the film's free surface means that we are always operating at zero pressure and this phase transition might be accessible. We can understand the reason for this A \rightarrow B phase transition by considering the size of a Cooper pair. When the film or slab is approximately the same size as a single Cooper pair, the $L=1$ component perpendicular to the substrate gets suppressed, favoring an anisotropic A-like phase. However, the size of a Cooper pair is just the coherence length $\xi(T)$, which is strongly dependent on the temperature. As the temperature falls, the Cooper pair gets smaller, so the confinement of the film is less important and a B-like phase is able to become stable.

As we have discussed, the specularity of the surface depends on the nature of the scattering of ^3He quasiparticles off the surface. It can be affected by the roughness of the surface [Buchholtz 1986], and it can be affected by the presence of a few monolayers of ^4He atoms between the surface and the ^3He film [Freeman *et al.* 1988], as we will discuss in Chapter 8.

F. Experiments on superfluid ^3He in restricted geometries

After the discovery of superfluidity in ^3He , research interest turned to the question of ^3He confined to restricted geometries. Initially, it was predicted that ^3He would not exhibit superfluid film flow as ^4He does [Sachrajda *et al.* 1985 and ref. 2 therein]. The principal reason for this was the difference in coherence lengths between the two materials; ^4He 's coherence length (reasonably far from T_c) is about 0.1 nm, while ^3He 's coherence length is on the order of 100 nm. This is the same order of magnitude as, if not larger than, the equilibrium film thickness of a film adhering to a wall above the meniscus of a free surface. Nevertheless, in 1985 researchers at Queens University, Kingston, Ontario [Sachrajda *et al.* 1985] observed superfluid film flow in films of ^3He , an observation which was confirmed by researchers at U.C. Berkeley in 1987 [Davis *et al.* 1987]. There followed a series of experiments and theoretical analyses by several different groups of researchers, establishing the basic properties of superfluid ^3He films and slabs [Davis *et al.* 1988], [Daunt *et al.* 1988], and [Steel *et al.* 1994], mapping their phase diagram [Freeman *et al.* 1988] and [Li and Ho 1988], and observing the enhancement of ^3He superfluidity caused by interposing a few atomic layers of ^4He between the substrate and the ^3He [Freeman *et al.* 1988] and [Harrison *et al.* 1991].

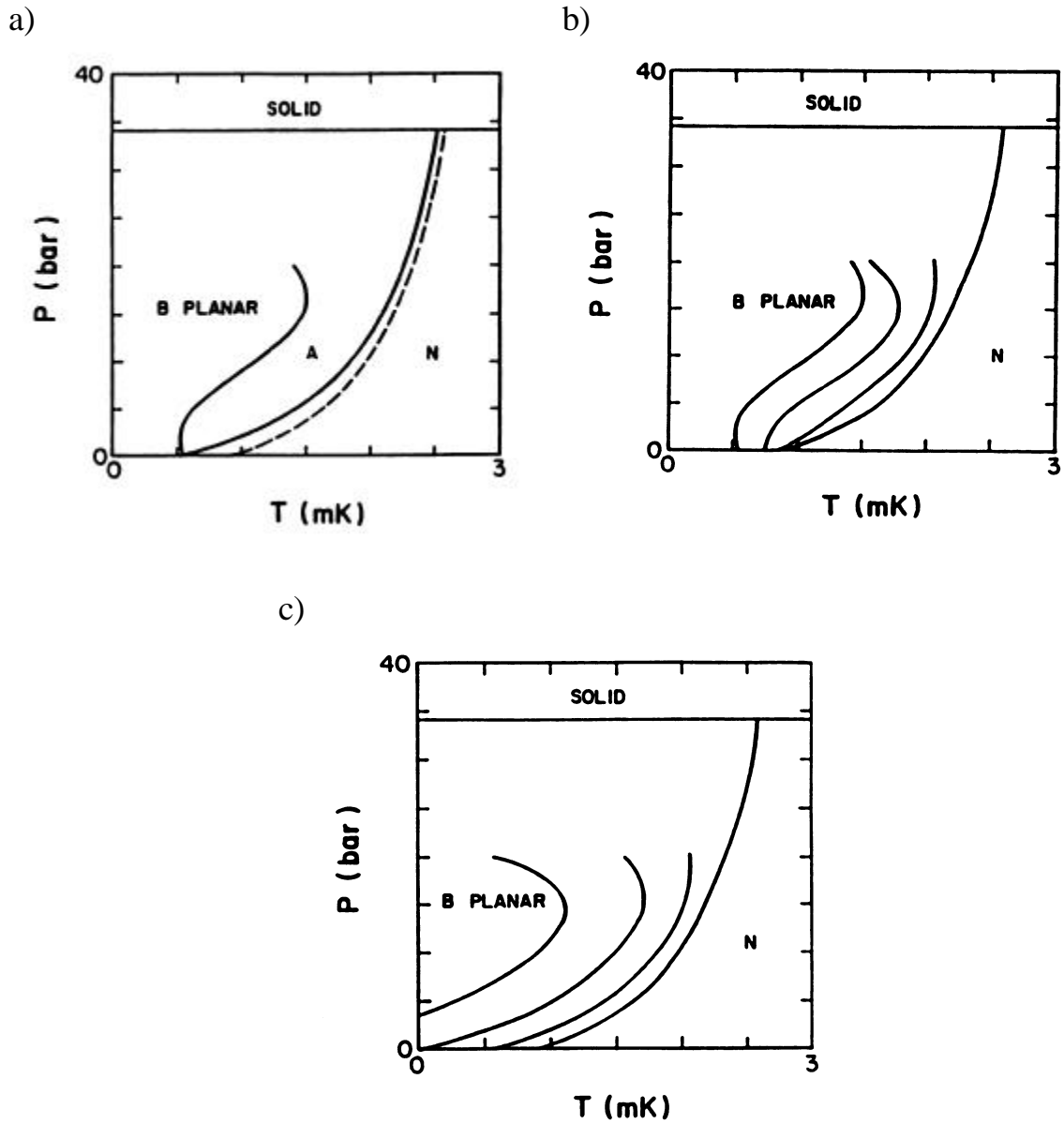


Figure 2.6 The phase diagrams for films or slabs of liquid ^3He . a) shows the phase diagram for a 100 nm thick film with diffusive boundary conditions. The dashed line is the transition line for bulk ^3He . b) shows the phase boundary between A and B-planar phases, for a diffusive boundary as a function of $d = 100, 150, 250$ nm and bulk, from left to right. c) shows the same except for a specular boundary. [from Li and Ho 1988]

These experiments provide the groundwork which underlies the experiments described in this thesis.

One early experiment on superfluid $^3\text{He-B}$ by Manninen and Pekola [Manninen, Pekola 1982] reported the observation of superflow through 0.8 micron diameter channels, up to a critical current at which point a transition to dissipative flow occurred. From the temperature dependence of the measured critical current, the researchers deduced that the superfluid density and the transition temperature were reduced inside the narrow channels. Several experiments, [Pekola *et al.* 1984], [Gammel *et al.* 1984], and [Gammel *et al.* 1985] observed the persistent superflow of both $^3\text{He-B}$ and $^3\text{He-A}$. In Pekola's experiment, an AC gyroscope packed with 20 micron diameter powder carried a mass current without dissipation for at least 48 hours, implying a viscosity 12 orders of magnitude lower than in the normal fluid. This experiment is analogous to a persistent electrical current in a superconducting loop. Another experiment [Pekola *et al.* 1987] measured the suppression of the critical current and superfluid transition temperature of ^3He passing through a single submicron cylindrical channel. The observations were in reasonable agreement with the Ginzburg-Landau predictions for a diffusively scattering boundary.

In 1985, Queen's University researchers [Sachrajda *et al.* 1985] observed film flow in a beaker-emptying experiment. They watched the rate at which liquid flowed over the lip of the beaker, through the film, into the (lower) surrounding bath, as they cooled down the sample. Their initial report indicated that the observed transition temperature of film was near 3 mK, (higher than the bulk transition temperature), but subsequent experiments by the same group found the transition always below T_c^{bulk} , in accordance with the Ginzburg-Landau theory [e.g. Daunt *et al.* 1988].

The anomalously high T_c was attributed to either an error of thermometry or thermally driven normal flow. They observed $T_c = 3.5 \pm 0.5$ mK for their thicker, $h \sim 0.9$ mm film, and $T_c = 2.0 \pm 0.5$ for their thinner, 1.4 mm film with the temperatures measured using the magnetizing field as a thermometer, calibrated with a LCMN thermometer. Assuming the thermometry was properly done, the observed flow could possibly have been normal fluid flow, driven by a temperature gradient between the ^3He outside the beaker, which was directly cooled by a heat exchanger, and the ^3He inside the beaker which was not. This possibility was eliminated in the group's later experiments, by using a second heat exchanger to directly cool the ^3He inside the beaker. In any case, all further work observed only superfluid ^3He film flow when the temperature was below T_c^{bulk} .

In their further work, [Daunt *et al.* 1985] the Queen's University group observed the suppression of the transition temperature, $T_c^{\text{film}}/T_c^{\text{bulk}}$ to vary from 0.93 to 0.7 as the film thickness at the rim of the beaker thinned from 120 to 90 nm. In addition, they observed the temperature dependence of the critical current to vary as $(1-T/T_c^{\text{film}})^{3/2}$, as predicted by the Ginzburg-Landau theory [Jacobsen and Smith 1987], although neither the T_c^{film} values nor the magnitude of the currents observed matched the Ginzburg-Landau results numerically.

The Queen's University experiment was a breakthrough in that film flow was observed for the first time, and it measured several important parameters: the suppression of T_c^{film} from T_c^{bulk} and the temperature dependent critical current of the film flow. However, the experimental method was unsatisfactory in one important respect: as the

beaker self-emptied through film flow, the film's thickness was constantly falling, so the film was never in stable equilibrium.

In 1988, U.C. Berkeley researchers [Davis *et al.* 1988] carried out film flow experiments on stable saturated ^3He films for the first time. Partially submerging a disk in a bath of liquid ^3He , they observed that when they cooled significantly below T_c^{bulk} , a film would form on the exposed surface. The onset of film flow occurred at temperatures T_c^{film} which were always reduced from T_c^{bulk} , in accordance with the Ginzburg-Landau theory. Once the film had formed on the surface, its thickness could be measured capacitatively using a plate suspended above the surface as the second half of a parallel plate capacitor. The film was in stable equilibrium, and its thickness could be controlled by raising or lowering the bath's level. Using the electrode above the film to induce chemical potential gradients, superfluid film flow could be induced. In addition to seeing the suppression of T_c , the Berkeley researchers also observed the Ginzburg-Landau temperature dependence of the critical current, $j \sim (1-T/T_c^{\text{film}})^{3/2}$. The success of this work inspired the search for third sound waves in a stable ^3He film which this thesis reports.

In addition to work on ^3He films, there have also been important experiments on slabs of superfluid ^3He . The restricted-geometry physics of ^3He films and slabs is almost identical, the only difference being the free surface of a film. It is customary for theoretical studies to treat a film as 1/2 of a slab, assuming that the free surface of the film has a specular boundary condition which acts identically to the symmetry plane halfway between the two walls enclosing the slab. When comparing theoretical and experimental work, it is therefore important to keep track of possible factors of 2 in 'effective' film thicknesses.

In the same year that the Berkeley group observed superflow in stable ^3He films, a group at Cornell [Freeman *et al.* 1988] made two important advances relevant to ^3He films. The experiments they carried out were on superfluid ^3He slabs filling the interstices between 3000 1.5 micron thick Mylar sheets held 300 nm apart, making the 'effective film thickness' of the ^3He about 150 nm. First, they used NMR to identify positively the superfluid phase of the ^3He slabs as A-like, filling in part of the restricted-geometry phase diagram. Further, the ^3He acted as the load for a torsional oscillator, whose high-Q resonance frequency shifted to reflect the amount of normal ^3He attached to it. This allowed them to make measurements of the ^3He superfluid density as a function of temperature as well. Their second advance was in demonstrating that covering the substrate with an extremely thin coating of ^4He changes the boundary condition of the order parameter dramatically. This ability to tune the boundary condition, changing the Cooper pair scattering from diffusive to specular, presented researchers with the possible key to studying ^3He superfluidity and quantum size effects in films so thin that the presence of the walls would quench the order parameter completely.

The Queen's University and U.C. Berkeley experiments measured film flow rates and superfluid transition temperatures for a range of film thicknesses; the Cornell experiments measured the superfluid density for only a single effective film thickness. In 1990 researchers at Purdue [Xu and Crooker 1990] reported measurements of the superfluid density of ^3He films over a broad range of film thicknesses. Their experimental setup consisted, as did the Cornell group's, of a torsional oscillator;

however, they developed a technique [Crooker and Xu 1990] of growing a metastable unsaturated ^3He film on the oscillator, allowing them to prepare a range of thin films. By heating a small well of liquid at the base of their cell, ^3He atoms were transferred through the vapor onto the torsional oscillator plate, forming a non-equilibrium film. During this process and afterwards, they measured the thickness of the ^3He film by observing the change in the resonant frequency of the torsional oscillator. After cooling down through the superfluid transition, they found that the films would thin slowly, on the order of 10 nm per day; this drift in the film thickness, of about 1% during a data-collection run, became a virtue by enabling them to measure several film thicknesses during a single demagnetization cycle.

They studied films ranging from 83 to 172 nm, from temperatures ranging from T_c^{bulk} down to $0.35 T_c^{\text{film}}$, observing suppression of T_c^{film} which agreed well with the Kjalman, Kurkijarvi and Rainer calculation. For their thicker films, near $d=160$ nm thick (equivalent to slabs of thickness 320 nm), they reported superfluid density fractions ranging from 0 at T_c^{bulk} to 0.062 at $T=0.35 T_c^{\text{bulk}}$ [Xu 1991].

Interestingly, they observe that the data for superfluid density, when graphed against the reduced film thickness $w=d/\xi(T)$ falls onto two separate curves depending on whether the thickness is above or below 137 nm. This suggested to them that there could be a thickness dependent phase transition in the ^3He film. However, they noted that both experimental and theoretical evidence suggested that the B phase to A phase transition should take place at a higher thickness, and that a transition to a truly 2-D phase would be expected to behave differently with respect to supercooling and superheating. From these observations, they concluded that the transition must be from the A-phase to a non-B, unidentified phase such as the A1 phase.

G. Potential for future ^3He physics

The ^3He film is a relatively unexplored system which has the potential for some very interesting physics, with relevance beyond its own sub-field. It is a 2-D superfluid with an unconventional, p-wave symmetry. The role that 2-D systems play in layered superconductors has just begun to be appreciated; for instance, dynamics resulting from the Kosterlitz-Thouless 2-D phase transition (which was first seen in ^4He films) has just been observed in a d-wave superconductor [Corson *et al.* 1999]. The ^3He film is another system in which the same types of questions can be asked, and similar phenomena observed and understood.

Chapter 3. Third Sound in ^4He

In this Chapter we introduce the phenomena of third sound. After a brief review of superfluidity and the two-fluid model, we give a basic description of third sound and place it in the context of the other hydrodynamic 'sounds'. We then mention some of its uses in studying superfluid ^4He films and touch on its potential for studying superfluid ^3He films.

A. Superfluidity and two-fluid hydrodynamics

Water flowing down a pipe experiences viscous drag, which causes it to lose energy and slow down. Both liquid ^4He at very low temperatures, and liquid ^3He at extremely low temperatures, have the astonishing property that they can flow indefinitely without such energy loss. For this reason they are called "superfluids". This behavior is closely analogous to the superconductivity of electrons in metals at low temperatures. If an electric current is induced in a superconducting loop, the absence of electrical resistance means that the current will never measurably decay. Just so, the absence of viscosity in the helium superfluids will allow a persistent current circulating in a torus to circulate indefinitely if it is not interrupted.

However, other experiments seemed to show that liquid helium does possess some form of viscous dissipation. [see Tilley and Tilley 1986] For instance, in 1946 Andronikashvili suspended a stack of metal disks by a torsional fiber in a bath of liquid helium, as shown in Figure 3.1a. The frequency at which this stack twisted back and forth showed how much of the helium was locked to the motion of the metal disks. The disks were close enough together so that above 2.2 K, when the helium was not superfluid, all the helium between the disks would be dragged along; however, as the temperature was reduced below 2.2 K, the frequency rose, showing that a fraction of the helium decoupled itself, as if that fraction had lost its viscosity.

To account for behavior like this, Tisza suggested in 1938 and Landau developed in 1941 a "two-fluid model" in which helium is thought of as being composed of two interpenetrating liquids, a superfluid component and a normal-fluid component. Each of these components has its own density, ρ_s and ρ_n , respectively, and each moves at its own velocity, \mathbf{v}_s and \mathbf{v}_n , respectively. The total density is just the sum of components' densities,

$$\rho = \rho_s + \rho_n \quad (3.1)$$

and the total mass current density is just the sum of the two mass current densities,

$$\mathbf{j} = \rho_s \mathbf{v}_s + \rho_n \mathbf{v}_n \quad (3.2)$$

The superfluid component is free to flow without viscosity, while the normal-fluid component experiences the viscous drag common to liquids. As the temperature falls, the liquid becomes more superfluid, that is, the fraction of liquid in the superfluid component ρ_s/ρ , gets larger and the fraction in the normal fluid component, ρ_n/ρ , gets smaller.

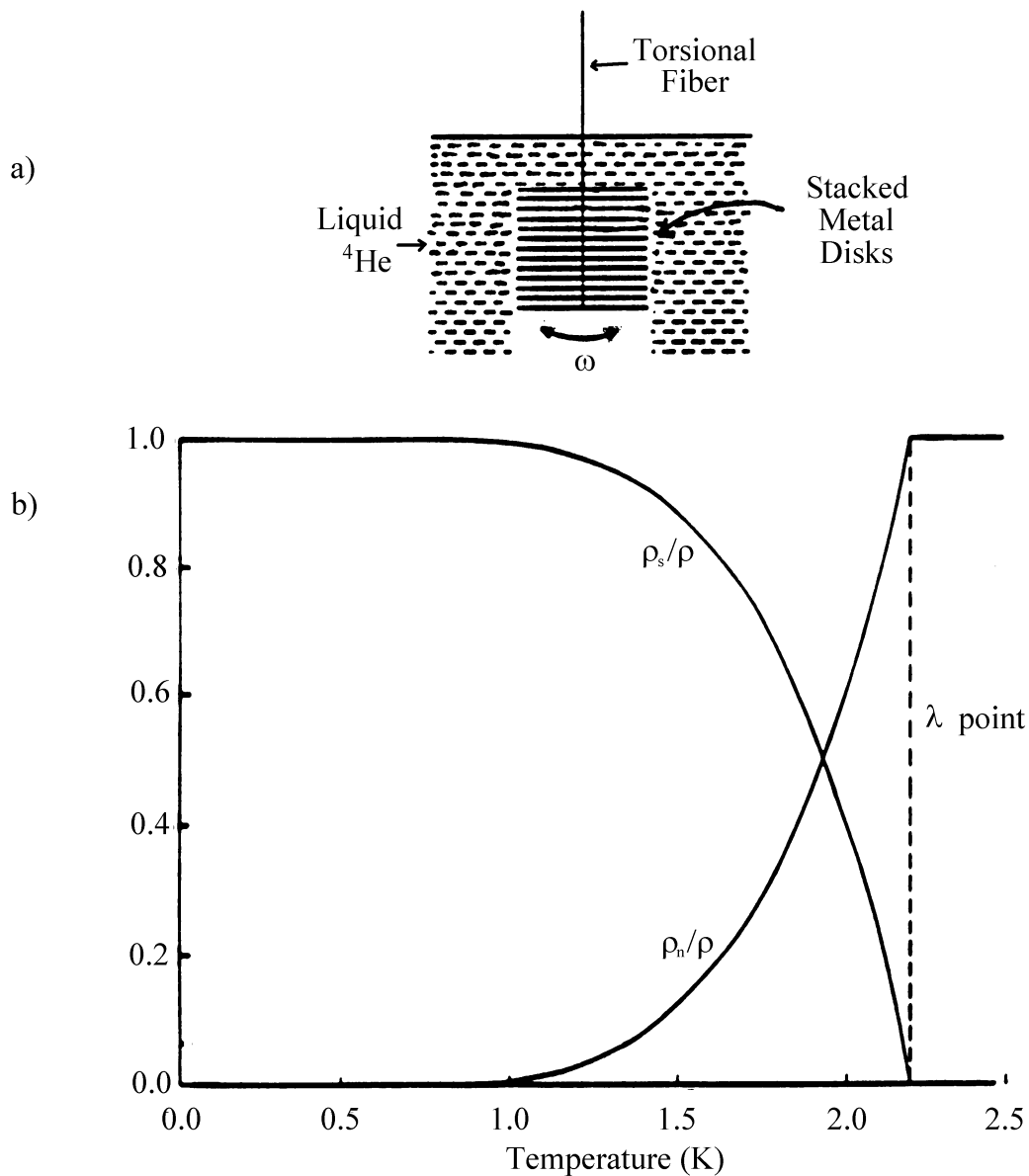


Figure 3.1 The Andronikashvili experiment. a) shows the stack of closely-spaced metal disks hanging from a torsional fiber in a bath of ^4He . Andronikashvili's experiment measured the superfluid density and normal-fluid density as a function of temperature for liquid ^4He , obtaining the results shown in b). [from Tilley and Tilley 1986]

B. Third sound

In 1959, K.R. Atkins [Atkins 1959] pointed out that the "two-fluid" hydrodynamic equations of motion for superfluid helium can, in special circumstances, have a solution in which only the superfluid fraction of the liquid is in motion, while the normal fluid component of the liquid remains stationary. The two special cases he considered were a thin film of helium and a narrow tube filled with helium, and he dubbed the wave motion of the liquid "third sound" and "fourth sound" in these two cases.

Consider a thin film of liquid helium on a substrate, as shown in Figure 3.2. Normal fluid near a wall, such as the substrate above, tends to move with the wall or remain stationary if the wall is stationary. The normal liquid only moves freely when it is farther from the wall than the viscous penetration depth. For our situation, the film thickness $d \sim 100$ nm is much less than the viscous penetration depth (see Chapter 5.A), so the normal-fluid velocity \mathbf{v}_n is zero. The normal-fluid component of the helium is clamped to the substrate.

However, the superfluid component experiences no viscous drag and it is free to move, oscillating parallel to the substrate. This causes vertical motion of the surface, in a manner analogous to shallow-water waves such as you might see at a beach. It is this wave motion that Atkins called 'third sound'.

The speed of a shallow-water wave is given by $c_{\text{water}} = \sqrt{gd}$ where g is the acceleration due to gravity and d is the water's depth. As we will see in more detail later, the speed of third sound is given by $c_3 = \sqrt{\{(\rho_s/\rho) a_{\text{vdw}} d\}}$ where a_{vdw} is the acceleration due to the van der Waals attraction between the helium and the substrate, d is the film's depth, and the factor of ρ_s/ρ is added to account for the fact that only the superfluid component of the helium is moving.

The first observation of third sound in ^4He was made in 1962 by C.W.F. Everitt, K.R. Atkins, and A. Denenstein [Everitt *et al.* 1962, 1964] in which they measured the velocity and attenuation of the surface waves as a function of the excitation frequency, the film thickness, and the temperature. Since then, third sound has been a valuable probe of superfluid films and the physics of surfaces. Third sound had not been detected in superfluid ^3He until the work described in this thesis.

C. Other 'sounds' of superfluid helium

In order to provide a framework in which to understand third sound, we will briefly review the properties of the other "sounds," or forms of wave propagation in superfluid helium which are allowed by the "two-fluid" hydrodynamics of the system.

First and second sound are both waves which can propagate through a bath of bulk helium. (For a derivation of the properties of first and second sound, see [Tilley and Tilley 1986, §3.9].) We can write down the hydrodynamic equations of motion for the system.

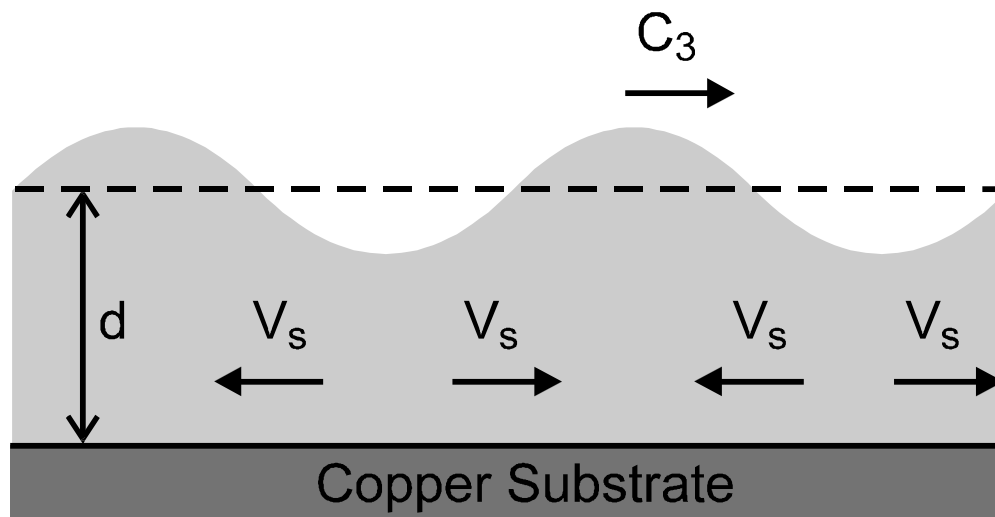


Figure 3.2 A third sound wave on a substrate. The superfluid component of the film oscillates parallel to the substrate, causing small-amplitude surface waves which travel with the velocity c_3 .

Continuity (or mass conservation): A divergence in the mass current must be accompanied by a change in the local density.

$$\partial\rho/\partial t = -\tilde{\mathbf{N}}\cdot\mathbf{j} = -\tilde{\mathbf{N}}\cdot(\rho_s \mathbf{v}_s + \rho_n \mathbf{v}_n) \quad (3.3)$$

Entropy conservation: The entropy in the superfluid is carried by the normal fluid, so a change in the local entropy per unit mass σ must be accompanied by a divergence in the normal fluid current.

$$\partial(\rho\sigma)/\partial t = -\tilde{\mathbf{N}}\cdot(\rho\sigma\mathbf{v}_n) \quad (3.4)$$

Acceleration equations: Gradients in the pressure p or the temperature T will accelerate the superfluid and normal-fluid components.

$$\rho_s \partial\mathbf{v}_s/\partial t = -(\rho_s/\rho) \tilde{\mathbf{N}}p + \rho_s\sigma \tilde{\mathbf{N}}T \quad (3.5)$$

$$\rho_n \partial\mathbf{v}_n/\partial t = -(\rho_n/\rho) \tilde{\mathbf{N}}p - \rho_s\sigma \tilde{\mathbf{N}}T \quad (3.6)$$

Removing the velocities from this set of equations, we can extract two coupled differential (wave) equations relating the pressure and entropy of the fluid. These equations approximately decouple, giving us two different sound modes, first and second sound, whose velocities are given by

$$c_1^2 = (\partial p/\partial\rho)_\sigma \quad c_2^2 = (\rho_s/\rho_n) \sigma^2 (\partial T/\partial\sigma)_p \quad (3.7)$$

First sound is a wave propagation in which the local entropy density is constant, there are no thermal gradients in the liquid, and the normal and superfluid components of the helium move at the same velocity, $\mathbf{v}_n = \mathbf{v}_s$. The propagating wave consists of a fluctuating local density, and the speed of propagation depends on the isentropic derivative of the pressure with respect to the density. In essence, this is just the wave mode which is usually referred to as "sound".

Second sound, on the other hand, is a distinctly superfluid effect. Here the local density of the liquid is constant and there are no pressure gradients. This is accomplished by requiring that the superfluid and normal-fluid components move opposite to each other, or out-of-phase, so that there is no net mass current. The relative motion of the two components creates an oscillation in the local entropy density and temperature, and the speed of the propagating wave depends on the ratio of the superfluid to normal-fluid fraction of the liquid, which is a strong function of temperature below T_c . (It is more precise to say that density oscillations are second-order compared to temperature oscillations in second sound and vice versa in first sound.)

Like third sound, fourth sound is a wave phenomenon in which the normal fluid component of the liquid is clamped rigidly in place by the constricted geometry and its own viscosity, while the superfluid component is free to move. Third and fourth sound were first suggested by Atkins in the same paper [Atkins 1959]. The speed of fourth sound is approximately the first sound speed reduced by the square root of the superfluid density fraction, since only the superfluid fraction is participating in the wave.

All of the above 'sound' modes occur in the hydrodynamic limit, where the wave frequency ω is much less than the inverse of the quasiparticle collision time τ , $\omega\tau \ll 1$. In this limit, the liquid is always approximately in thermodynamic equilibrium, so an increase in density yields an increase in pressure exerted by quasiparticle collisions which yields a restoring force and wave propagation. In contrast, in the 'collisionless' limit when $\omega\tau \gg 1$, any excess quasiparticles will simply diffuse away without exerting a pressure on a nearby element of liquid, so no hydrodynamic wave will propagate. However, if there is an interactions between the quasiparticles not related to collisions, it is possible for these interactions to act as a restoring force, driving a sound mode called 'zero sound'.

All of these sound modes have been observed and studied in superfluid ^3He . This thesis presents the first observation of third sound in superfluid ^3He .

D. Third sound in ^4He and ^3He

Third sound has proven itself to be an excellent probe of superfluid films, partly due to the fact that its speed depends on the superfluid density, a key parameter for understanding superfluid behavior. For example, third sound has been used to study the "critical velocity" of flowing ^4He films [Pickar and Atkins 1969], the persistence of supercurrents [Ekholm and Hallock 1980], phase transitions, including the Kosterlitz-Thouless 2-D transition [Rudnick 1978], the limits of superfluidity in extremely thin ^4He films [Shirron and Mochel 1991], and vortices in two-dimensional systems [Ellis and Li 1993]. More generally, what these experiments and others have shown us is that third sound can be used to do very sensitive, high-Q measurements on the superfluid state in ^4He .

There is also a large number of studies of $^3\text{He}/^4\text{He}$ mixtures with third sound in ^4He [Sheldon and Hallock 1994]. This research relies on the superfluid properties of ^4He to study the mixtures in which (usually) just a small amount of ^3He has been added. It is important not to confuse these experiments with the mirror-image work on ^3He superfluidity, where a small amount of ^4He is often added with the intent of enhancing the superfluidity through coating the film's substrate. We have already discussed the effect of such ^4He coatings on the boundary conditions for the ^3He order parameter, and we will later discuss our attempts to use this technique.

Considering the wide variety of applications for which third sound in ^4He has proved useful, it is perhaps surprising that third sound as a probe of superfluid ^3He films has not been pursued until recently [Eggenkamp *et al.* 1998]. Third sound has great potential as a dynamic probe of the ^3He film, in which the superfluid motion reveals the film's properties directly. Despite the relatively low quality factors observed for third sound modes in this experiment, it is still hoped that high-Q third sound modes can be generated, enabling us, for instance, to measure $\rho_s(d,T)$ with much more precision, exploring the phase diagram for ^3He films and possibly resolving the question of the possible phase transition observed by the Purdue group [Xu and Crooker 1990]. Even without such high-Q modes, it should still be possible to observe frequency shifts to the third sound resonances due to the effects of 2D vortices, in an experiment analogous to Ellis's "quantum swirling" [Ellis and Li 1993].

Chapter 4. Experimental Design

In this Chapter we give details of the design and construction of the experimental cell which has been used to detect third sound in superfluid ^3He . We describe the substrate for the film, the capacitor plates used to generate and detect the third sound waves, the capacitive level detector used to measure the height of the bulk liquid inside the cell, and the excitation and detection methods. Then, we discuss the refrigeration and thermometry which was used to carry out this sub-mK experiment.

A. Experimental cell

As described in the previous Chapter, in 1988 researchers at U.C. Berkeley [Davis *et al.* 1988] carried out a series of experiments on superfluid ^3He film flow examining the stable film which forms on the exposed surface of a disk partially submerged in a helium bath. The success of that experiment, both in observing superflow and in providing a controlled means of varying the film's thickness, suggested that this basic geometry could be used to excite and detect third sound waves on ^3He films.

i. Overview

In this section we will describe the design and construction of the experimental cell used in this work. A scale drawing of the cell is shown in Figure 4.1, and an extremely-not-to-scale sketch to aid understanding is shown in Figure 4.2. A ^3He film is produced by placing a copper disk in a bath of liquid ^3He such that its flat, polished surface rises above the free surface of the bath. After the ^3He bath is cooled below its superfluid transition temperature, the van der Waals attraction between the ^3He and the copper disk pulls ^3He atoms onto the disk's exposed surface, which becomes the substrate for the film. The thickness of the film is governed by the energy balance between the gravitational pull down off the disk and the van der Waals pull onto the disk. The film's thickness can be measured by using the substrate as one side of a parallel plate capacitor; the other side is a second metal plate suspended 30 μm above the substrate; since ^3He has a dielectric constant of about 1.0426, the film increases the capacitance of the parallel plate capacitor linearly with the film thickness. We measure the height h by observing the capacitance change of another parallel plate capacitor, this one formed from two concentric cylinders mounted vertically in the bath, around the substrate. The height h can be varied either by adding more ^3He to the cell, or by actuating a bellows attached to the cell which hydraulically raises or lowers the bath's height.

In order to manipulate the ^3He film, we again utilize its dielectric property. When we apply a voltage difference between the substrate and a 'drive' plate suspended above it, we produce an electric field between the plates which pulls more ^3He from the bath, thickening the film. Applying an oscillating voltage to the drive plate at an appropriate resonant frequency excites standing waves on the film's surface. These waves can be

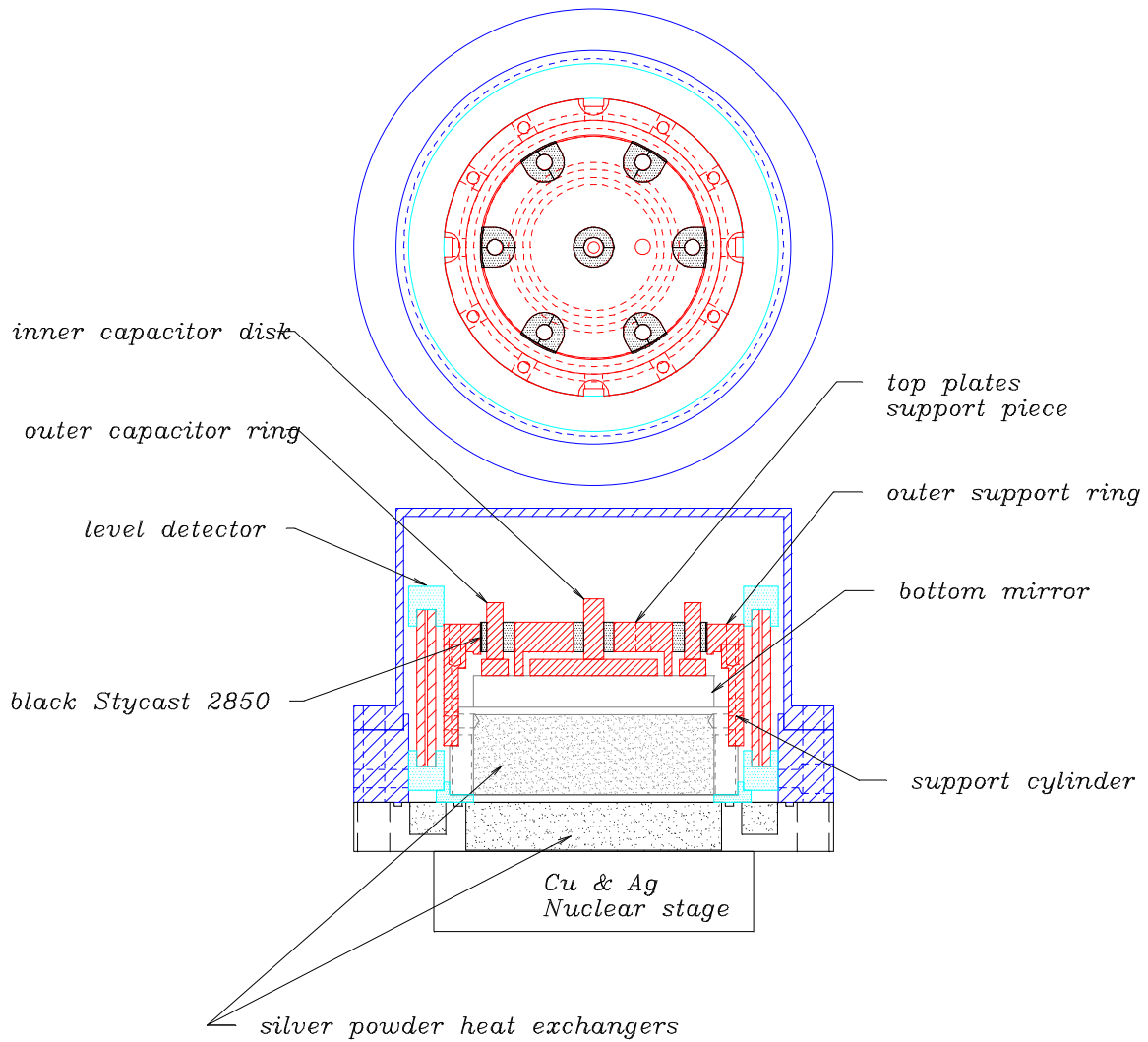


Figure 4.1 Scale drawing of the experimental cell. Top is a view from above, showing the seven Stycast 2850 pieces suspending the drive and detection electrodes above the substrate. Bottom is a profile view of the cell.

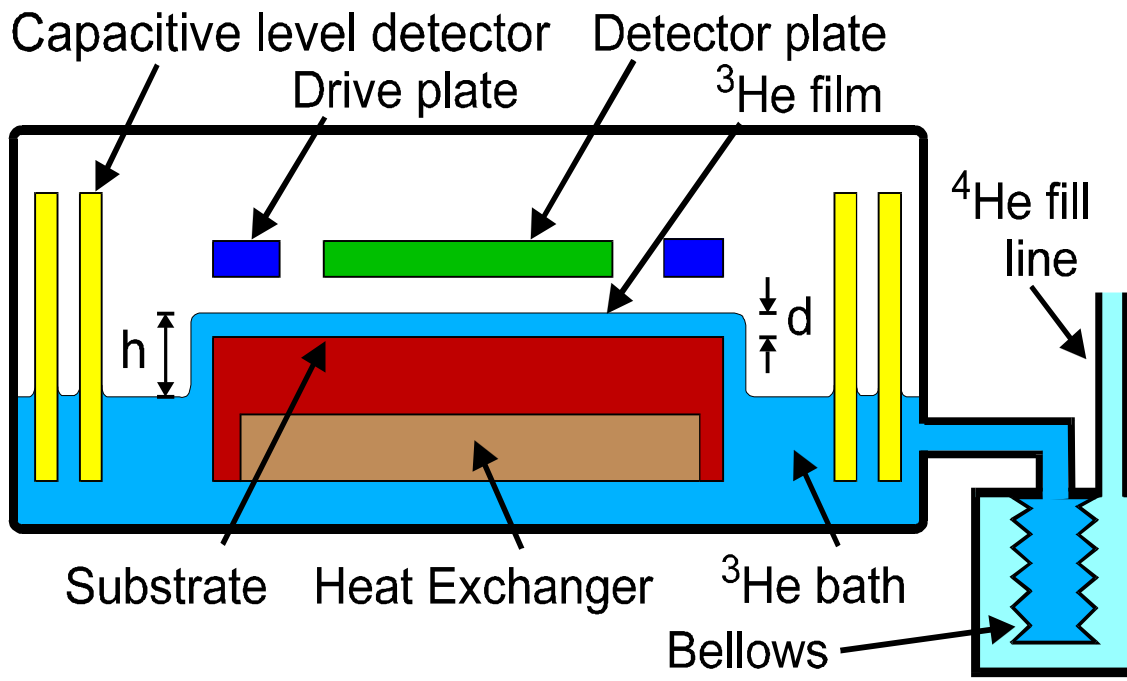


Figure 4.2 Not-to-scale drawing of the experimental cell.

detected by measuring the capacitance change between the substrate and a 'detector' plate suspended over a different section of the substrate than the drive plate. We use a standard symmetric AC capacitance bridge circuit to measure the changes in capacitance. We use a nuclear demagnetization refrigerator, pre-cooled by an Oxford 200 dilution refrigerator, to cool the ^3He sample down below its superfluid transition temperature and measure the temperature of the bulk liquid in the cell with a pulsed Pt NMR susceptibility thermometer.

ii. Substrate

The substrate is the exposed top of a cylindrical copper piece 0.75" tall, and it is 1.5" in diameter. The copper piece maintains this diameter for 0.2" of height, then widens to 1.825" for its remaining 0.55" of height. In earlier experiments, substrates of either silver [Davis 1989] or gold evaporated onto copper [Schechter *et al.* 1998a] were used; here we used a mechanically polished copper substrate. Prior to polishing, the bottom 0.5" of the copper piece was hollowed out and packed with sintered silver powder, to act as a heat exchanger. The effective combined surface area of this heat exchanger and the heat exchanger attached to the nuclear stage copper bar was measured to be $140 \pm 3 \text{ m}^2$ using a BET test. When placed inside the cell, liquid ^3He suffuses the silver powder, establishing good thermal contact between the helium and the internal parts of the experiment, cooling the substrate and the superstructure above the substrate.

After the silver powder was pressed into the heat exchanger on the bottom of the cylinder, the opposite side (which had been machined with a regular cutting tool) was polished to an apparent mirror finish by lapping. A series of diminishing grit sizes down to 0.25 microns was used. This polished surface has a radius of 0.75" and an area of $1.14 \times 10^{-3} \text{ m}^2$.

Since the intent of the design was to create standing waves on the substrate, the condition of the edge of the substrate is significant. The edge appears rounded, with a radius of curvature of about 0.3 mm, and it is rougher than the polished surface. Waves could reasonably be expected to reflect from this edge, either due to the sudden change in roughness at the edge, or to the increasing film thickness as the surface falls towards the bulk liquid.

iii. Capacitor plates

In order to manipulate the film, a set of plates is suspended about 30 microns above the substrate. This superstructure consists of three concentric plates: an inner disk of radius 10.1 mm and area $3.21 \times 10^{-4} \text{ m}^2$ called the detector plate, an annular disk of inner radius 13.6 mm, outer radius 17.8 mm and area $4.13 \times 10^{-4} \text{ m}^2$ called the drive plate, and a 2 mm wide grounded ring separating the drive and detection plates which acts as an electrostatic shield. The dimensions of the drive and detection plates were chosen to optimize both the sensitivity of the detector to the Bessel-shaped modes we expected to create on the substrate and our ability to excite these modes using the drive plate.

These plates are suspended above the substrate using a superstructure made of copper and Stycast 2850 epoxy, as seen in Figure 4.1. Twelve small spacers made of 25 micron thick 100HN Kapton film were placed on the substrate, the plates were positioned on top of the Kapton, and then they were glued to a horizontal supporting piece. The amount of liquid glue used in this process is very small: the bulk of the Stycast 2850 (which acts as electrical insulation, and has a thermal contraction coefficient close to that of copper) is in the form of small machined cylinders. The horizontal supporting piece had previously been screwed tightly to a vertical cylindrical ring which had been screwed, in turn, to the wide section of the substrate cylinder. Once the glue set, the horizontal support piece and plates were lifted, the Kapton pieces were removed, and the plates were returned to their previous position. In construction, the size of the vertical gap may be varied by using different sizes of Kapton film.

One difficulty with this method is the differential thermal contraction which occurs when cooling the plates down from room temperature to 4 K. The design was chosen to minimize this effect, but the plates still moved, on average, several microns with respect to the substrate during this process, as seen by monitoring the capacitance between the substrate and plates during cool-down. Another difficulty, probably related to this thermal contraction, is that the plates may be tilted with respect to the horizontal plane defined by the substrate by as much as 20 microns at either edge. This could occur either when they are positioned, if the plates are themselves spherically deformed for instance, or during cool-down if the thermal contraction is not symmetric. The effect of this would be to break the azimuthal symmetry of the cell design, and as we will discuss in the next Chapter, we do see indications in our data that there is a substantial asymmetry.

iv. Capacitive level detector: bulk liquid height and film thickness

The thickness of the saturated film which forms on the substrate is governed primarily by the energy balance between the gravitational force pulling the liquid down and the van der Waals attraction between the helium and the copper substrate. Since this implies a relation between the film's thickness and the height difference, h , from the free surface of the bulk liquid to the film's surface, it is useful to directly measure the height of the bulk liquid inside the cell. We measure h using a capacitive level detector, which is formed from two concentric cylindrical copper plates. The inner plate is 0.985" high, has an inner diameter of 1.975" and an outer diameter of 2.075". The outer plate is the same height, with a 2.115" ID and a 2.215" OD. Thus there is a 0.020" gap between the plates, which can fill with helium through the opening at the bottom. Two supporting pieces made of Stycast 1266 maintain the alignment of the plates and hold them in position inside the cell. As shown in Figure 4.1, this level detector surrounds the substrate. As the level of the dielectric liquid helium rises in the cell, the capacitance of the detector rises linearly. The level detector capacitance which corresponds to the height of the substrate was determined both by the dimensions in the cell construction and by observing the height at which the region between the substrate and plates fill completely. We can measure changes in the film thickness directly by observing the changing capacitance between the substrate and the plates and the two measurements taken

together allow us to determine the strength of the van der Waals attraction, as we will discuss in Chapter 6.

During the initial phases of the experiment, in order to vary the film thickness we had to add helium to the cell from a keg at room temperature. Apart from the imprecision of this method and the impossibility of thinning an existing film by removing material, the technique is unsatisfactory in that the film thickness could not be changed while staying below T_c . To solve this problem, we added a volume changer to the cell, consisting of a bellows which could be hydraulically compressed or expanded, shown in Figure 4.3. This forces liquid into or out of the cell, thus lowering or raising h and raising or lowering the film thickness d . This process can be done while staying below T_c , allowing us to get a continuous measurement of d vs h to determine the van der Waals attraction coefficient. The volume changer is actually composed of two copper-nickel electro-welded bellows¹ joined by a thermally resistive Vespel rod. The top of the first bellows (1" long, 0.75" OD, complete compression of 0.35") is mounted rigidly on a plate just below the mixing chamber. A fill line, identical to the ^3He fill line to the cell and thermally lagged to the still plate, cold plate, and mixing chamber plate allows us to pressurize the first bellows with ^4He . This causes the bellows to expand, pressing down the 6.5" long Vespel rod, which in turn compresses the second bellows. This bellows, rigidly supported from below, is positioned alongside and slightly lower than the experimental cell. When the cell is filled, this bellows fills completely with liquid ^3He as well; compressing it causes ^3He to be forced from the bellows into the cell, raising the helium level with respect to the plates. The lower bellows is partially filled with a teflon spacer, so that its inner volume is almost zero when it is completely compressed.

v. Excitation method

To excite superfluid motion, we apply electric fields to the film relying on the dielectric property of ^3He . This method has been used before by other researchers [e.g. Ellis and Luo 1989]. Applying a voltage between the substrate and the drive plate creates an electric field within the parallel plate capacitor, and gradients in this field produce an acceleration of the helium film. This can be understood either in terms of the chemical potential balance or in terms of the forces involved.

An electric field between the parallel plates adds a term to the chemical potential per unit mass which is of the form

$$\mu_E = \frac{1}{2} \epsilon \epsilon_0 E^2 / \rho. \quad (4.1)$$

In order to maintain the chemical potential balance between the free surface of the bulk liquid in the bath and the free surface of the film, this chemical potential change must be offset by an increase in the film thickness, reducing the chemical potential due to the van der Waals interaction. Thus, applying voltages between the plates causes a thickening of the film, which depends on the square of the applied voltage. For our third sound drive, we apply a voltage $V_{dc} + V_{ac} \sin \omega t$, where $V_{dc} \gg V_{ac}$, so that the applied chemical potential varies as $E^2 \sim V_{dc}^2 + 2 V_{dc} V_{ac} \sin \omega t$, an offset plus a sinusoidal drive.

¹ FC-15 stock bellows, Servometer Corporation, Cedar Grove, NJ.

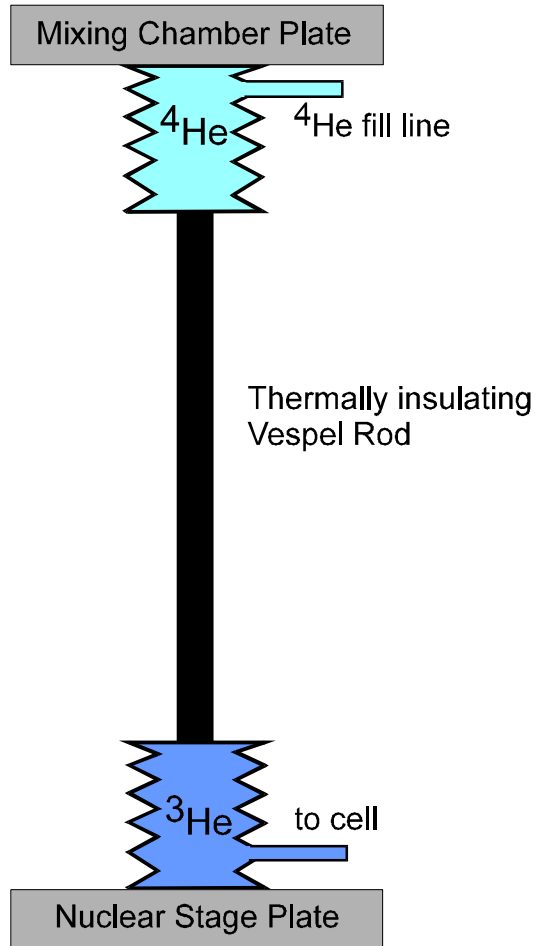


Figure 4.3 Sketch of the volume changer apparatus.

(Note that too large an electric field will cause the film thickness to increase without limit, filling the space between the plates [Cole *et al.* 1978].)

Alternatively, we can look at the equations of motion for the superfluid film, which we discuss in detail in Chapter 5. An electric field between the plates adds a force, or more precisely a pressure, to the superfluid equation of motion. As we will see, a gradient in the electric field produces an acceleration of the superfluid in the film, so that the edge fields of the capacitor push helium between the plates. This means that the applied forces are only near the drive plate's edges, rather than under the entire drive plate. This is important to realize when choosing the plate dimensions, since the efficiency of the drive for a particular third sound mode depends on the mode's amplitude within a very narrow ring directly beneath the edge's of the drive plate. We calculated the electric field for our plate geometry and determined the narrow ring to have a width approximately $1\frac{1}{2}$ times the spacing x_0 between the plates, with $\frac{1}{2}x_0$ the width under the drive plate and x_0 the width just out from under the plate.

In addition to electric fields, helium films can also be excited thermally; for work on third sound in ^4He films, thermal excitation is the standard method. The first observation of third sound by Everitt, Atkins, and Denenstein [Everitt *et al.* 1964] used pulses of infrared radiation to heat a strip of the film 1 mm long across the width of the film. Hallock [Brooks *et al.* 1978] and other researchers put down thin metallic strips on the substrate, which act as local heaters. Either technique creates a pulse of third sound which propagates away from the heated strip. This third sound generation works in either of two ways. First, a small amount of heat will couple to the film via the thermal gradient in the equations of motion [see Chapter 5], causing superfluid acceleration, local thickening, and a propagating wave; or second, a large amount of heat will evaporate away a small amount of film, directly creating a trough which then propagates away [Eggenkamp 1998]. Since it is desirable to introduce as little heating as possible in a sub-mK experiment on ^3He films, we chose to avoid this thermal excitation method and use the capacitive method described above.

Much of the work using third sound in ^4He has been done using thermal excitation to create pulses, or travelling waves. A different approach, creating standing waves in a third sound resonator, has been used by other researchers [Ratnam and Mochel 1970], [Ellis and Hallock 1983], [Volz *et al.* 1985] and has several potential advantages. For instance, the resonances observed in ^4He experiments using this technique are very sharp, with Q's ranging from 10^4 to 10^6 [Ellis and Luo 1992]. This allows for precision frequency measurements of the superfluid's behavior. It allows a range of detection methods not available in pulse experiments. Also, it allows a gentler driving force, which can take advantage of the film's natural resonances. We designed our experiment to look for the Bessel-shaped resonant standing waves which would appear on the circular substrate due to reflection from the edge of the substrate. We measured quality factors for such resonances in ^4He tests as high as $Q = 4000$, and we hoped that we would be able to see similar responses in ^3He films.

vi. Capacitive detection method

Our detection technique, measuring the capacitance change due to changes in the film's thickness, has been used by several other researchers [e.g. Swift 1980]. The relation between a change in film thickness Δd , a change in capacitance ΔC , and an equivalent change in the separation between the plates Δx is given by

$$\Delta C / C = - \Delta x / x_0 = (1 - 1/\kappa) \Delta d / x_0 \quad (4.2)$$

where C is the total plate capacitance, x_0 is the plate separation, and κ is the dielectric constant of the liquid. When the change in the film thickness is not uniform, but varies across the substrate underneath the detector, the change Δd is the average film thickness change underneath the detector, and this can be related simply to the oscillation amplitude of any mode whose shape is known.

There are several alternatives to capacitive detection, which have been utilized by other researchers. In the first work on third sound in ^4He , Everitt, Atkins, and Denenstein [Everitt *et al.* 1964] used ellipsometry - they observed the change in the plane of polarization of a light beam reflecting off the surface of the liquid, which reveals changes in the thickness of the film. An interesting advantage of this technique is that the beam can (in principle) be swept across the surface of the film, mapping out the shape of resonant responses. This method should be considered for future resonance-type experiments in superfluid ^3He . Other workers [Rudnick *et al.* 1968] utilized the thermal oscillations which are present in a third sound wave by putting a thin superconducting strip across the substrate and using it as a bolometer to measure the passage of the third sound wave. Apart from the fact that this relies on thermal waves in the film, which are dissipative and therefore to be avoided if possible, this technique is not suitable for ^3He films.

The electronic circuit which measures the average film thickness change (or simply the capacitance between the inner detector plate and the substrate) is a symmetric AC capacitance bridge. The electronics for both drive and detection are shown schematically in Figure 4.4. The bridge is operated at frequencies on the order of 1 kHz. The AC bridge drive voltage V_d is provided by the internal reference oscillator of a SR830 DSP lock-in amplifier,² and is typically less than 1 V. This voltage signal drives an isolation transformer with a 1:3 turns ratio. The four principal elements of the bridge are the experimental capacitor with $C_{\text{expt}} \sim 99$ pF, a reference capacitor with $C_{\text{ref}} \sim 80$ pF, and an inductor divided into two sections by a grounding tap. The inductor is a 7-digit ratio transformer³ at room temperature, with an output impedance of 5 ohms. In series with this is a resistive balance potentiometer,⁴ which is typically set to ~ 80 ohms. The reference capacitor is a silver mica capacitor glued with Stycast 1266 inside a copper box (thus electrically shielded) and thermally tied to the cold plate just below the 4 K pot (to insure its thermal stability). The coaxial cable reaching down to the experimental

² Stanford Research Systems, Sunnyvale, CA.

³ Model DT 72A, Tegam, Inc., Geneva, OH or Electro Scientific Industries, Portland, OR.

⁴ ESI Decade Resistor Model DB 52B.

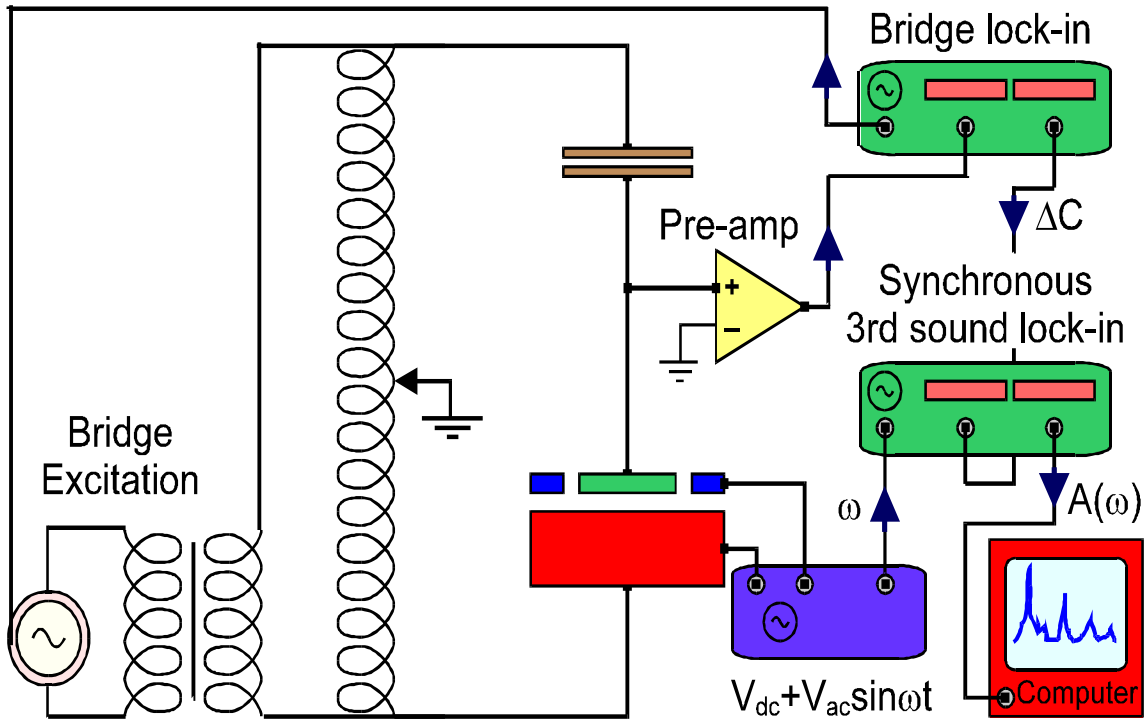


Figure 4.4 Schematic of electronics. The electronics for driving and detecting a third sound resonance. The left-hand side is a symmetric AC capacitance bridge which measures the capacitive signal ΔC due to film motion. We use a two lock-in arrangement to monitor the component of ΔC at the third sound driving frequency ω , which becomes the amplitude $A(\omega)$. Sweeping ω produces the observed third sound spectra.

capacitors is stainless steel core with stainless steel braid.⁵ The cable capacitance is about 30 pF/ft, which added up to about 200 pF for each coax going from room temperature to the experimental cell. On different runs, we used one of three different preamplifiers: an SRS560 preamplifier,⁶ EG&G Model 5183, and EG&G Model 5003.⁷ At the bridge frequency of ~1 kHz, the preamplifiers typically had input noise levels of 4-6 nV/ $\sqrt{\text{Hz}}$, leading to a sensitivity of ~20 pm/ $\sqrt{\text{Hz}}$.

Simple circuit analysis of the idealized circuit shown in Figure 4.5a gives the output voltage reaching the preamplifier as

$$V_{\text{out}} = V_{\text{in}} [\alpha C_{\text{expt}} - (1-\alpha) C_{\text{ref}}] / (C_{\text{ref}} + C_{\text{expt}}) \quad (4.3)$$

so that the bridge is balanced when

$$C_{\text{expt}}/C_{\text{ref}} = (1-\alpha)/\alpha = 1/\alpha - 1 \quad (4.4)$$

The sensitivity of the bridge to changes in the experimental capacitor is

$$dV_{\text{out}} / dC_{\text{expt}} = V_{\text{in}} C_{\text{ref}} / (C_{\text{expt}} + C_{\text{ref}})^2 \quad (4.5)$$

which has its maximum value for $C_{\text{expt}} = C_{\text{ref}}$. For this reason, we match the reference capacitor to the experimental capacitance (precision is not needed since the peak is broad).

The realistic capacitance bridge shown in Figure 4.5b has the same balance point and the need for capacitance matching. However, the signal-to-noise ratio of the realistic circuit suffers a drop by a factor of $(C_{\text{expt}}+C_{\text{ref}})/(C_{\text{cable}}+C_{\text{ref}}+C_{\text{expt}}) \sim 1/2$ due to the stray capacitance to ground of the coaxial cable, which has $C_{\text{cable}} \sim 200$ pF. One partial remedy for this ill would be to place a low-temperature preamplifier inside the vacuum can, so that the cable capacitance leading to it would be cut by more than half. This would change the sensitivity drop factor from 1/2 to about 2/3, a 33% gain in signal. Another approach to improve the signal-to-noise would be to increase the experimental and reference capacitor values, since (when $C_{\text{ref}} = C_{\text{expt}} = C$) the output voltage is

$$dV_{\text{out}} / V_{\text{in}} = 1/4 * (1 + C_{\text{cable}}/2C)^{-1} dC / C \quad (4.6)$$

However, in either case, the improvement would only be a factor of order 1 in the signal-to-noise ratio.

For the swept-frequency experiments we apply a sinusoidal drive voltage between the outer plate and the substrate, using the circuit shown in Figure 4.5. The computer instructs a second lock-in amplifier⁸ to set its reference oscillator to the driving frequency ω . This reference is sent to an amplifier⁹ with gain 10, which adds a DC offset. The resulting voltage applied to between the drive plate and the substrate has the

⁵ Cooner Wire, AS632-1SS or -1SSF for plastic-covered.

⁶ Stanford Research Systems, Sunnyvale, CA.

⁷ EG&G Instruments, Princeton Applied Research, Princeton, NJ.

⁸ SR830 DSP Lock-in Amplifier, Stanford Research Systems, Sunnyvale, CA.

⁹ Bipolar Operation Power Supply / Amplifier, Kepco, Inc., Flushing, NY.

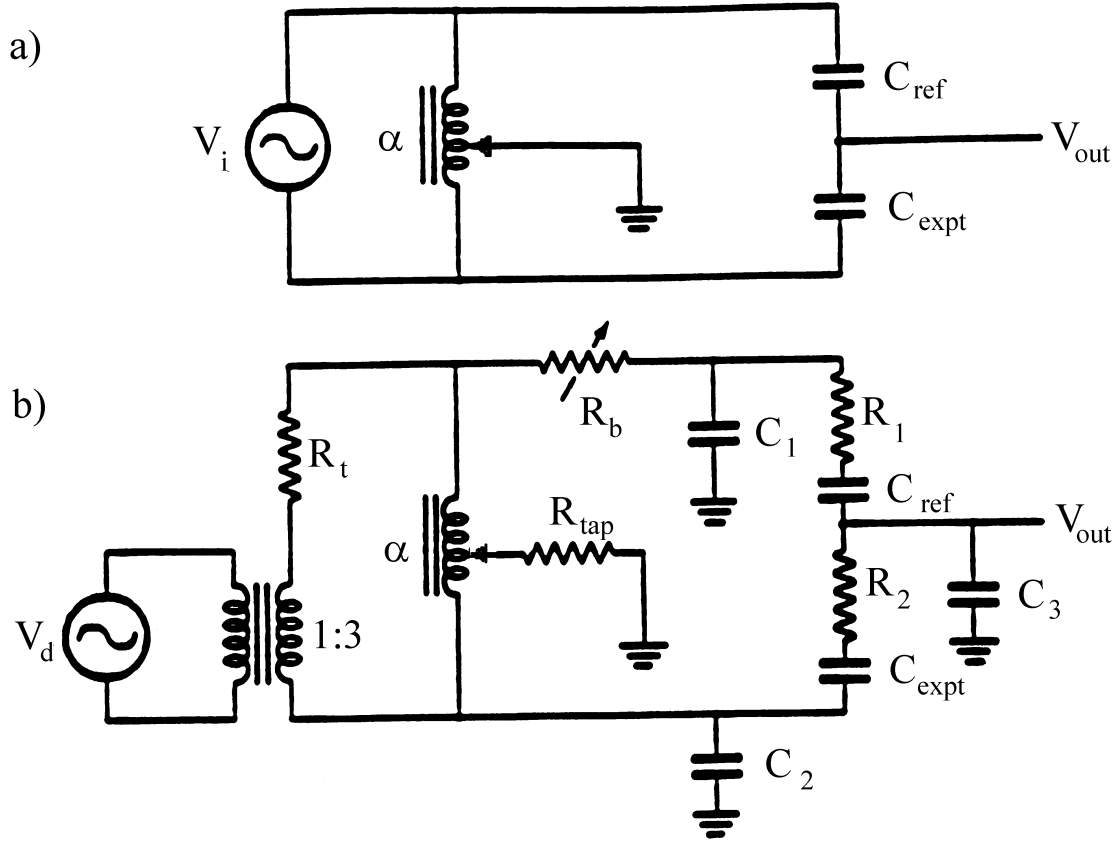


Figure 4.5 Schematic of a symmetric AC capacitance bridge. a) shows an idealized circuit, while b) shows a more realistic representation (*see* [Swift 1980] for detailed discussion). Here the experimental capacitance is C_{expt} , the reference capacitor is C_{ref} , and C_1 , C_2 , and C_3 are stray capacitances to ground due principally to the capacitance of the coaxial cable.

form $V_{dc} + V_{ac} \sin \omega t$. The response from the film is measured by sending the detector capacitance signal ΔC to the input of the second lock-in amplifier, which extracts the amplitude and phase of the response at the driving frequency. The driving frequency is swept, typically from 0.2 Hz to 5 Hz, waiting at each frequency value a sufficient time for the lock-in to stabilize and for a resonance (if present) to ring up. Data taken in this manner produce the 'third sound spectra' which are discussed in Chapter 6.

B. Cryogenics and thermometry

To perform experiments on superfluid ^3He films, it is necessary to reach temperatures well below 1 mK, or $1/1000^{\text{th}}$ of a degree above absolute zero. We use a (now standard) copper nuclear demagnetization refrigerator attached to a conventional dilution refrigerator. The copper acts as an "ice cube" to cool the liquid ^3He , whose thermal contact to the copper is enhanced by two silver-sinter heat exchangers. The temperature of the liquid ^3He is measured using a magnetic susceptibility thermometer, using pulsed NMR signals to monitor the susceptibility of a sample of platinum powder in thermal contact with the liquid. The temperature is then obtained via Curie's law, $M = C/T$, with the constant determined by calibration at the bulk superfluid transition temperature T_c^{bulk} . We have been able to reach a base temperature of $T/T_c^{\text{bulk}} = 0.335$ during the course of these experiments. The ^3He film could be expected to have a slightly higher temperature than the bulk; we will discuss the thermal resistance between the film and the bulk, and the effect of the bridge drive and third sound driving force on the temperature of the film.

An Oxford Instruments 200 dilution refrigerator is used to pre-cool the magnetized nuclear stage and experimental cell to about 13 mK before demagnetization. Dilution refrigeration is the only continuous refrigeration technique available for temperatures below 300 mK. Our refrigerator operates with a base temperature of about 6 mK without an additional external heat load, and a typical pre-cooling cycle requires about 48-72 hours to cool the nuclear stage to 10-13 mK in a 8 Tesla magnetic field. (For further information about dilution refrigeration, see [Pobell 1992], [Betts 1976, 1989] or [Lounasmaa 1974].)

The nuclear demagnetization stage is formed from a single bar of copper, 1" x 1" x 16". In order to reduce the eddy current heating in the copper bar, five vertical slots 0.050" are carved the length of each face, limiting the cross-sectional distances which electrons can travel when there is a changing magnetic flux. Four thermally resistive Vespel rods support the nuclear stage and experimental cell, and a superconducting heat switch allows thermal contact to be made or broken with the dilution refrigerator. When the thermal contact is broken, the heat leak to the nuclear stage is measured to be typically about 1 nW. The heat switch is formed from aluminum diffusion welded to copper [Zieve 1992]. A solenoid¹⁰ made using multi-filament superconducting wire, with a maximum current of 74 amps, is suspended outside the main vacuum can in the helium bath of the dewar. The magnet produces a field with a maximum of ~ 8 Tesla, with an average of $\sqrt{\langle B^2 \rangle} = 5.7$ T over the length of the copper bar, and it is constructed so that the magnetic field dies off to less than 50 Gauss in the region above the copper bar where

¹⁰ American Magnetics, Oak Ridge, TN, order #2003.

the experiment is positioned. This minimizes the effect of the main magnetic field on the experiment, in particular on the operation of the NMR Pt-susceptibility thermometer.

The magnetization, pre-cool, and demagnetization procedures are straightforward. Before magnetizing, the heat switch connecting the nuclear stage and experimental cell to the dilution refrigerator's mixing chamber is closed, so that the dilution fridge may remove the heat of magnetization. The persistent current switch of the main magnet is imperisisted, the current in the magnet is ramped up to 70 A in about 1 hour, and the magnet is persisted. The current is then quickly removed from the external leads. (On the very first magnetization after cooling to 4K, the magnet's persistent current switch may spontaneously imperisist at this point; in this case the magnet must be 'trained' by persisting at progressively higher currents successfully.) The heat of magnetization may be observed warming the resistance thermometer on the mixing chamber and the NMR thermometer monitoring the ^3He inside the cell. After several days of pre-cooling, the temperature of the cell has been cooled to about 10 mK, and the heat switch between the nuclear stage and the dilution refrigerator is opened, thermally isolating the cell and magnetized copper. The current in the external leads is matched to the current persisted in the main magnet, and the magnet is imperisisted. The current in the main magnet is then slowly ramped down over a period of about 8 hours. This slow rate prevents excessive eddy current heating from warming the nuclear stage. Since the power supply is computer-controlled and the demagnetization actually occurs in small steps of about 30 mA, a low resistance shunt is placed across the magnet current leads to smooth out these steps, which would otherwise contribute greatly to the eddy current heating. As the demagnetization proceeds, the temperature of the copper nuclei fall proportionally to the magnetic field.

The thermal contact between the copper nuclei and the ^3He liquid inside the experimental cell occurs in two steps. The rate at which the temperature of the nuclei comes into equilibrium with the temperature of the conduction electrons in the copper is given by the spin-lattice relaxation time, also called the Korringa time, $\tau_1 = \kappa / T_{\text{electrons}}$. For copper the value of the Korringa constant is 18 min·mK. (For platinum, the Korringa constant is 30 sec·mK, which is important for the NMR thermometer.) The conduction electrons of the copper then cool the ^3He liquid through the thermal boundary resistance, or Kapitza resistance. In order to reduce this boundary resistance, the top of the copper bar is e-beam welded to a large silver-sinter heat exchanger which has a large effective surface area. The liquid ^3He in the cell fills in the pores in the packed silver powder, which forms the base of the experimental cell, shown in Figure 4.1. About 0.050" directly above this heat exchanger is another heat exchanger which is built into the base of the experimental substrate and capacitor plates. This allows the ^3He inside the cell to efficiently cool the mass of the experiment itself. The Kapitza resistance is inversely proportional to the surface area of the heat exchanger; using the BET method we measured the surface area of the cell to be $140 \pm 3 \text{ m}^2$. Since the two heat exchangers inside the cell were made by the same technique, it is probable that this area is divided proportionally to the volume of the silver powder in each heat exchanger. Since the volumes of the two heat exchangers are almost identical, the surface area is probably split $\sim 70 \text{ m}^2$ to each.

At the end of each demagnetization, before warming up, we measure the background heat leak into the nuclear stage and experimental cell. The procedure for this

is simply to allow the ^3He in the cell to warm up with zero external field, measuring the temperature $T(t)$. With the main magnet off, the heat capacity of the ^3He in the cell dominates that of the rest of the nuclear stage. Above 1 mK, the heat capacity of ^3He (a normal Fermi liquid) is linear in T so its temperature will go as $T \propto \sqrt{t}$ and the heat leak will be proportional to dT^2/dt . Typically the heat was about 1 nW; however, during the first several weeks after cooling down, a heat leak of up to 10 nW, slowly falling, would appear. This time-dependent heat leak, presumably due to the heat capacities and long thermal time constant for cooling the plastics inside the cell, prevented us from reaching the fridge's base temperature immediately after cooling down from room temperature. The lowest temperature which we measured for the ^3He during this experiment was $T/T_c^{\text{bulk}} = 0.335$, while we routinely reached $T/T_c^{\text{bulk}} = 0.400$. (The addition of small amounts of ^4He to the cell drastically hinders our ability to reach these temperatures; we will discuss this in the section on ^4He coating of the surface.)

The temperature of the bulk liquid ^3He inside the cell was measured with a NMR susceptibility thermometer, measuring a sample of platinum powder in thermal contact with the liquid ^3He . The thermometer was suspended vertically, just below the experimental cell so that it filled with ^3He when the cell was filled. The thermometer was calibrated at T_c^{bulk} by observing the characteristic change in the ^3He susceptibility signal at the superfluid transition. This identifies T_c^{bulk} to within a few μK . The noise on individual measurements of the NMR temperature varies from $\sim 1 \mu\text{K}$ to $\sim 10 \mu\text{K}$ as the temperature varies from 0.35 mK to 1 mK.

The NMR thermometer measures the temperature of the bulk ^3He . The film on the substrate is cooled via thermal conduction through the film itself, and across the large Kapitza resistance to the copper substrate. It is possible that there is a temperature difference between the film and the bulk liquid. In this case, the observed behavior of the film would lag behind changes in the measured temperature of the bulk liquid, an effect we have not seen to a significant degree.

We have observed that increasing either the amplitude or frequency of the capacitance bridge drive can result in a significant heating of the ^3He . As discussed by [Swift 1980], the dominant source of heating is dielectric losses which are linear in applied voltage and go as ω^2 . We operated the capacitance bridge at drive levels where there was typically (almost) no measurable change in the temperature measured by the NMR compared to the temperature with the capacitance bridge off.

We also observed effects on the spectra of third sound as we increased the drive voltages which we attributed to heating of the film, though the NMR temperature did not change measurably. This effect is discussed further in Chapter 6.

Chapter 5. Hydrodynamics of Third Sound in ^3He

In this Chapter, we examine the hydrodynamic equations of motion for ^3He films, discuss how standing waves are generated and present a model for the observed third sound resonance spectra. Analyzing the two-fluid hydrodynamic equations of motion for a ^3He film leads to a simple wave equation for surface waves, when dissipative terms are neglected. This analysis shows that the third sound waves are analogous to long-wavelength waves propagating on shallow water. (We will consider the effects of the dissipative terms in a later section.) On the cylindrical substrate in our experimental cell, the wave equation has solutions which take the form of Bessel functions in their radial shape, and whose exact form depends critically on the wave reflection (or boundary condition) at the edge of the substrate. We can determine experimentally what boundary condition is present by analyzing the ratios of the frequencies of the observed modes. With this information as a starting point, we construct a model which calculates in detail the third sound spectra we would expect from our experiment, obtaining at least qualitative agreement with our observations.

A. Wave equation and speed of third sound waves

The basic two-fluid hydrodynamic equations of motion were written down by Atkins [Atkins 1959] in his original derivation of third sound in ^4He films. A more detailed analysis is carried out by Bergman [Bergman 1969, 1971] and Brouwer [Brouwer *et al.* 1995] in the case of ^4He films and Eggenkamp [Eggenkamp *et al.* 1998] then adapted Brouwer's analysis to the case of ^3He films in certain regimes.

The analysis for films of superfluid ^3He is simplified from that for ^4He due to the absence of vapor above the film. Experiments on superfluid ^4He films are often carried out near $T_\lambda = 2.2$ K, where the vapor pressure is still 40 torr, and even at 1 K the vapor pressure of the ^4He is still 0.1 torr. So, for ^4He , several forms of interaction between the vapor and the film are important: evaporation and recondensation allowing mass transfer between the vapor and film, and matching the hydrodynamic motion of the film and vapor at their shared boundary. On the other hand, ^3He becomes liquid at 3.2 K but does not become superfluid until the temperature is decreased to below 1 mK, where the vapor is essentially non-existent. We can therefore ignore the analysis complications posed by the vapor.

The two-fluid hydrodynamics of a helium film is greatly simplified by the observation that, for most purposes, we can treat the normal component of the superfluid as fixed in place. (However, motion of the normal-fluid at the moving surface of the film can contribute to the dissipation, as pointed out by [Brand and Cross 1982].) The viscous penetration depth $\delta = \sqrt{\{(2/\omega) \cdot (\eta/\rho_n)\}}$ determines the length scale over which the a film's motion is locked to the motion (or lack thereof) of the substrate. Noting our third sound waves are at frequencies below 50 Hz, taking $\rho_n = \rho = 82 \text{ kg/m}^3$ as the worst-case scenario, and using the normal viscosity of $\eta = 0.25 \text{ (kg/m}\cdot\text{sec)} \cdot (\text{mK})^2 / \text{T}^2$, we find that the $\delta = 4.4 \text{ mm}$, much greater than the $\sim 100 \text{ nm}$ film thickness. Thus, the normal fluid component of the superfluid is held tightly in place by its own viscosity, and we can neglect its motion in our analysis.

The relevant restoring force for a wave traveling on the surface of superfluid ^3He is the van der Waals attraction between the ^3He atoms at the surface and the atoms in the film's substrate. This is the same force which is responsible for the formation of the film, pulling helium from the liquid bath onto the substrate. We will discuss this force further in section 2.B of Chapter 6. Two other restoring forces are weak enough to be neglected for the waves we are considering: gravity and surface tension. The acceleration due to the van der Waals restoring force, even for films which are very thick ($d \sim 300 \text{ nm}$) is $a_{\text{vdW}} \sim 10^4 \text{ m/s}^2$, much larger than the gravitational acceleration $g = 9.81 \text{ m/s}^2$. The acceleration due to surface tension, which Eggenkamp [Eggenkamp 1998] (working with Jochemsen and Frossati) focused on, depends strongly on the wavelength of the third sound:

$$a_{\text{surface tension}} \sim k^2 \sigma / \rho \quad (5.1)$$

where k is the wave-vector, σ is the energy per surface area, and $\rho = 83 \text{ kg/m}^3$ is the density. The importance of the surface tension term therefore depends strongly on the wavelength: for short wavelength waves, as Jochemsen and Frossati's group were proposing to excite, the surface tension could be comparable to, or even dominate, the van der Waals force. However, for the cell we constructed to look for third sound waves with $\lambda \geq 1.5 \text{ cm}$, the surface tension acceleration would be $a_{\text{surface tension}} \sim 0.3 \text{ m/s}^2$ using the surface energy per area $\sigma = 1.5 \times 10^{-4} \text{ Jm}^{-2}$ [Roche *et al.* 1997]. Even for the shortest wavelength waves in our cell, the surface tension is only a small perturbation to the van der Waals restoring force, so we will neglect it in the following analysis. (For a further discussion of surface tension in systems like this one, see [Steel *et al.* 1994].)

The hydrodynamic equations of motion for the system (see Figure 3.2) are therefore given by:

Conservation of mass: For a film with low compressibility, a divergence of the mass current must be accounted for a change in the local thickness of the film:

$$(\rho/d) \partial Z(\mathbf{r},t)/\partial t + \tilde{\mathbf{N}} \cdot (\rho_s \mathbf{v}_s) = 0 \quad (5.2)$$

Here ρ is the density of the film, ρ_s is the average superfluid density of the film (averaged over the vertical thickness of the film), $Z(\mathbf{r},t)$ is the vertical displacement of the surface from its equilibrium at the point \mathbf{r} on the surface, and \mathbf{v}_s is the superfluid velocity of the film parallel to the substrate.

(Euler) equation of motion: The acceleration of the superfluid parallel to the substrate is caused by a gradient in the chemical potential. This chemical potential gradient can arise from several sources: the van der Waals restoring force (and gravity) acting on gradients in the thickness, the surface tension acting on gradients in the curvature of the surface, and the temperature gradients in the film:

$$\begin{aligned} \partial \mathbf{v}_s / \partial t - \rho_s \xi_3 \tilde{\mathbf{N}} (\tilde{\mathbf{N}} \times \mathbf{v}_s) &= - \tilde{\mathbf{N}} \mu \\ &= - (a_{\text{vdW}} + g) \tilde{\mathbf{N}} Z(\mathbf{r},t) + (\sigma/\rho) \partial^3 Z(\mathbf{r},t) / \partial x^3 + s \tilde{\mathbf{N}} T \\ &= - a_{\text{vdW}} \tilde{\mathbf{N}} Z(\mathbf{r},t) + s \tilde{\mathbf{N}} T \end{aligned} \quad (5.3)$$

Here μ is the chemical potential, a_{vdW} is the acceleration due to the van der Waals force, σ is the surface energy per area, s is the entropy density per unit mass, and ξ_3 is the coefficient of second viscosity [Landau, Lifshitz 1959 §78]. (Second viscosity appears in processes related to changes in the volume or density of a material, typically vanishing for incompressible fluids. In this case, the ^3He is assumed to be incompressible, but the motion of the film's free surface allows the second viscosity, which is inherently dissipative, to play a role. We discuss this further in Chapter 7.) We have neglected the $(\mathbf{v} \cdot \tilde{\mathbf{N}}) \mathbf{v}$ term which appears on the left hand side of this equation - it is negligible as long as the wave amplitude is short compared to the wavelength [Landau, Lifshitz 1959 §12], which is emphatically the case here.

Heat flow equation: A gradient in the heat flow, which is itself caused by a gradient in the temperature, will cause either a change in the local temperature, a change in the film thickness (to deposit more entropy per unit area), or a entropy current out of the film (into the bulk liquid or the substrate):

$$(d/T_0) \tilde{\mathbf{N}} \cdot (\kappa \tilde{\mathbf{N}} T) = \rho s \partial Z / \partial t + (\rho c d / T_0) \partial T / \partial t + J_{\text{out}} \quad (5.4)$$

Here T_0 is the average temperature of the film, κ is the thermal conductivity of the film, c is the heat capacity per unit mass of the film, and $J_{\text{out}} = J_{\text{thermal}}/T$ is the entropy current out of the film.

The magnitude of the temperature gradients inside a film during a third sound wave is not known a priori. In the isothermal limit $\tilde{\mathbf{N}} T = 0$, third sound is a surface wave without an accompanying temperature and entropy wave. The only dissipative mechanism which would remain explicitly in the equations of motion would then be that due to second viscosity. In the adiabatic limit $J_{\text{out}} = 0$, and there is no entropy flow into or out of the film. However, the thermal waves which are coupled to the surface waves by the heat flow equation then provide a source of dissipation. In Chapter 7 we will discuss the contributions of these intrinsic dissipative mechanisms on the damping of the observed third sound resonances.

Derivation of wave equation: In the simplest case, assuming the isothermal limit and neglecting second viscosity, we obtain a wave equation by taking the time derivative of the conservation of mass equation and the spatial derivative of the equation of motion:

$$\partial^2 Z(\mathbf{r}, t) / \partial t^2 = c_3^2 \nabla^2 Z(\mathbf{r}, t) \quad \text{with } c_3^2 = (\rho_s / \rho) a_{vdW} d \quad (5.5)$$

This is the governing equation for a third sound wave; it is just the usual wave equation describing waves whose speed is given by c_3 .

Still in the isothermal limit, but keeping the second viscosity term, the governing equation takes the form:

$$\partial^2 Z(\mathbf{r}, t) / \partial t^2 = c_3^2 \nabla^2 Z(\mathbf{r}, t) + \rho_s \xi_3 \nabla^2 \partial Z(\mathbf{r}, t) / \partial t \quad (5.6)$$

In the non-isothermal, adiabatic limit, again neglecting the second viscosity term, the governing equation looks like:

$$\partial^2 Z(\mathbf{r}, t) / \partial t^2 = c_3^2 \nabla^2 Z(\mathbf{r}, t) - \rho_s (s^2 T_0 / \kappa) \partial Z(\mathbf{r}, t) / \partial t - \rho_s (s c d / \kappa) \partial T / \partial t \quad (5.7)$$

B. Standing waves, boundary conditions, and resonant frequencies

We have shown that, neglecting dissipative effects, the motion of the film's surface is governed by a wave equation. If we make the assumption (borne out by our observations) that the surface motion is strongly affected by the wave reflection at the edge of the cylindrical substrate, then solutions of the wave equation take the form of standing waves. These standing waves will have shapes given (in the radial component) by Bessel functions, and the resonant frequencies of these modes will depend on the zeros of the Bessel functions. The shapes and frequencies depend strongly on the exact form of the boundary condition at the edge of the substrate, as we will discuss. The problem, neglecting dissipative effects, is exactly analogous to the vibration of a circular membrane under tension supported at its edge $r = R$ [Morse and Ingard 1968]. The membrane's edge can be held rigidly fixed, allowed to move freely, or weighted to obtain some mixed boundary condition. This can also be described as a transmission-reflection problem: outgoing waves produced at the origin are either reflected back from the boundary, forming a standing wave, or transmitted beyond the boundary, carrying away energy.

The general solution of the wave equation in a cylindrical geometry can be expressed as

$$Z(r, \phi, t) = \sum A_{mn} J_m(k_{mn}r) (B_{mn} \cos m\phi + C_{mn} \sin m\phi) e^{i\omega t} \quad (5.8)$$

Here r and ϕ are the radial and azimuthal coordinates on the cylindrical substrate, ω is the frequency of the wave, $J_m(x)$ is the cylindrical Bessel function of order m , and k_{mn} is the wavenumber determined by the boundary conditions. In the case of complete azimuthal symmetry, only solutions having $m = 0$ are allowed; we will retain the $m = 0$ and $m = 1$ terms to account for the asymmetry we observe in the responses from the film. (The design schematic is azimuthally symmetric, but in construction this symmetry was broken, probably by a small tilt of the upper electrodes with respect to the substrate.)

We will first describe the consequences of the different boundary conditions, then discuss arguments for which should hold sway in our system. For a 'fixed' boundary, the displacement of the surface is zero, $Z(R, \phi, t) = 0$. This boundary condition is enforced by requiring $J_m(k_{mn}R) = 0$ which is true when

$$k_{mn} = \alpha_{mn} / R \quad (5.9)$$

where α_{mn} is the n^{th} zero of the $J_m(x)$ Bessel function. For the $m=0$ Bessel function, the first five zeros are given by $\alpha_{0n} = 2.405, 5.520, 8.654, 11.792, 14.931$. For the $m=1$ Bessel function, the first five zeros are given by $\alpha_{1n} = 3.932, 7.016, 10.174, 13.324, 16.471$. The radial profiles of the modes determined by this condition are shown in Figure 5.1. Since the surface displacement is constant at the edge, the equations of motion imply that the superfluid velocity \mathbf{v}_s of the film parallel to the substrate is not zero at the edge; instead, ^3He flows from the film into the liquid bath and vice versa.

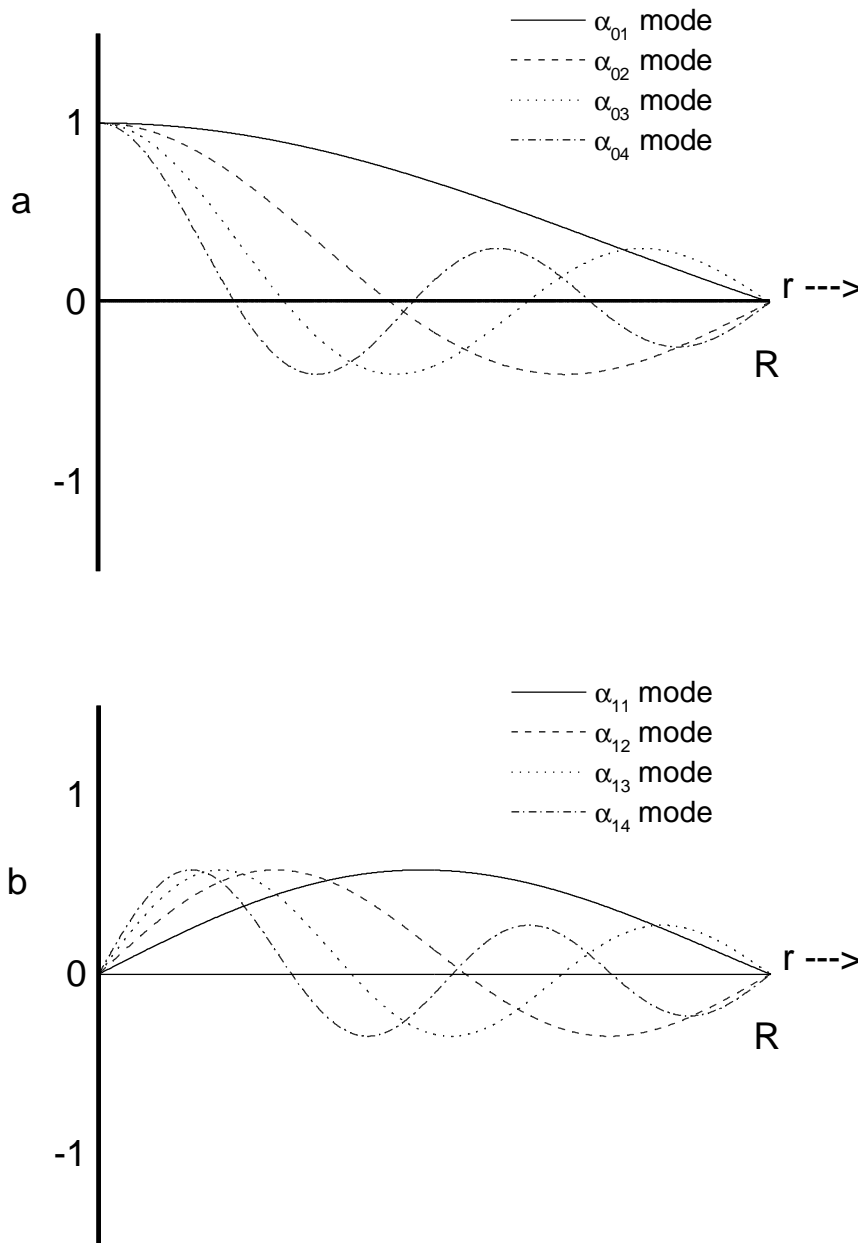


Figure 5.1 Bessel mode profiles for fixed boundary. a) Radial profiles of the $J_0(x)$ modes with a fixed boundary condition. b) Radial profiles of the $J_1(x)$ modes with a fixed boundary condition.

For a 'free' boundary condition, the surface displacement is not constrained but the superfluid velocity is: $\mathbf{v}_s(R, \phi, t) = 0$. From the equations of motion, we see that this requires a constraint on the gradient of the surface displacement, that $dJ_m(kr)/dr = 0$ at $r=R$ or

$$k_{mn} = \beta_{mn} / R \quad (5.10)$$

where β_{mn} is the n^{th} zero of the derivative of the $J_m(x)$ Bessel function. For the $m=0$ Bessel function, the first five zeros are $\beta_{0n} = 3.932, 7.016, 10.174, 13.324, 16.471$, the same as α_{1n} . For the $m=1$ Bessel function, the first five zeros are given by $\beta_{1n} = 1.841, 5.331, 8.536, 11.706, 14.864$. Notice that as n increases, this list becomes identical to α_{0n} , varying by 31% in the first zero, 4% in the second zero, and less after that. This means that the resonant frequencies observed for standing waves with a 'fixed' boundary are nearly identical to that for a 'free' boundary, the largest difference being that the first mode is 31% higher. The radial profiles for these modes are shown in Figure 5.2.

For a 'mixed' boundary condition, as would occur on a membrane if it were weighted, the radial component of the surface displacement is constrained by a linear condition involving Z and dZ/dr , of the form $0 = a Z(R, \phi, t) + b dZ(R, \phi, t)/dr$. This results in solutions whose wave-number is governed by the zeros of a linear combination $0 = c J_m(x) + d J'_m(x)$.

The exact cause of reflection at the substrate edge is unknown. A wave traveling across the film surface will encounter several rapid changes in its environment as it reaches the edge: the substrate's surface becomes rougher near the edge where the polishing did not touch; the film's surface curves; the film's effective thickness increases as it goes over the edge and reaches down to the bulk liquid; and the speed of capillary waves on the free surface of the liquid is orders of magnitude different than the third sound speed. Any or several of these could conceivably contribute to reflection at the boundary and to setting up standing wave modes. For instance, increased roughness could suppress the superfluid order parameter causing the fluid velocity at the edge to vanish, creating a 'free' boundary condition. Conversely, as was suggested by Ellis [Ellis 1998], roughness on the 1 micron scale could have cracks or grooves which fill up with bulk liquid due to capillarity, enhancing the superfluidity at the edge.

The wave boundary problem can also be viewed as a transmission/reflection problem matching the wave motion on the film to that over the edge of the boundary [Backhaus 1998]. The motion over the edge could either be the capillary waves on the surface of the bulk liquid or third sound waves on the rim of the substrate where the thickness of the film is different than on the surface of the substrate. One interesting feature of this idea is that the boundary condition, more specifically the amount of wave reflection, would depend on the speed of the wave and hence on the temperature. This could be responsible for some of the qualitative changes we see in the experimentally observed spectrum as a function of temperature.

Once the wavenumber (or wavelength) of a mode has been enforced by the boundary conditions, the resonant frequency of the mode is determined by the linear dispersion relation (obtained directly from the wave equation):

$$\omega_{mn} = c_3 k_{mn} \quad \text{or} \quad f_{mn} = c_3 k_{mn} / 2\pi \quad (5.11)$$

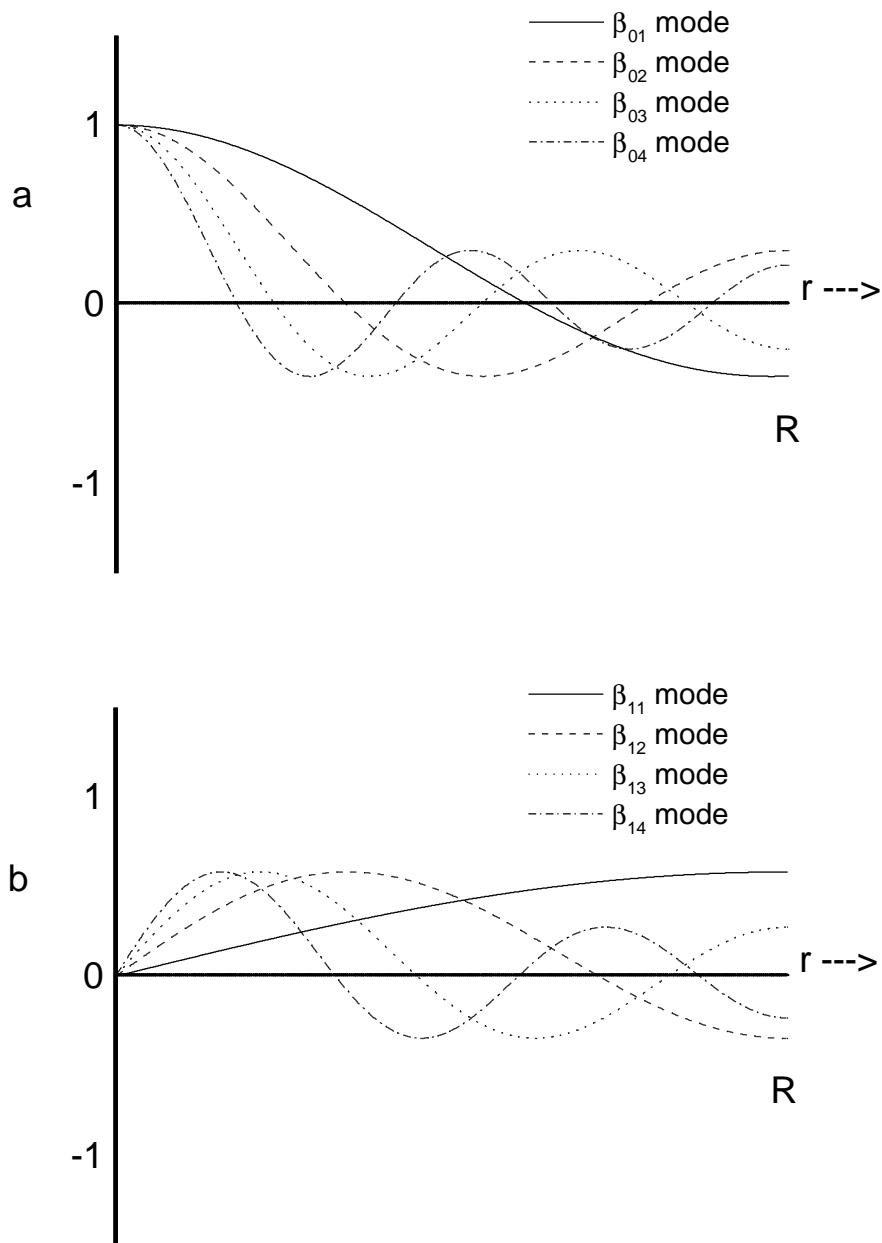


Figure 5.2 Bessel mode profiles for free boundary. a) Radial profiles of the $J_0(x)$ modes with a free boundary condition. b) Radial profiles of the $J_1(x)$ modes with a free boundary condition.

These resonant frequencies will vary as a function of film thickness, temperature, and any other variables which affect the speed of third sound. When c_3 is constant, at a particular temperature and film thickness, the resonant frequencies will be proportional to the spectrum of wavenumbers generated from the boundary conditions. By matching the observed spectra of resonant modes to the possible sets of wavenumbers, we can experimentally distinguish which boundary condition prevails in the cell. However, due to the damping of the modes, our identification of the modes (and hence the boundary condition) is not certain; for thick films at low temperatures, the spectra of modes observed appears to match best the 'fixed' boundary condition, as we will discuss in a later section.

In Figure 5.3 we show the shapes of various resonant modes, based on a 'fixed' boundary condition, for given mode-numbers m and n . The wavenumber $k_{mn} = \alpha_{mn}/R$ is given for each mode.

C. Model of film response

We now describe a model of the film's response to a driving force of the form we employ in our experiment. In the presence of a driving force F and a generalized damping term with coefficient β , the wave equation takes the form:

$$\partial^2 Z(\mathbf{r},t)/\partial t^2 - c_3^2 \nabla^2 Z(\mathbf{r},t) = F(\mathbf{r},t) - \beta \partial Z(\mathbf{r},t)/\partial t \quad (5.12)$$

This equation can be solved exactly by expressing the solution $Z(\mathbf{r},\phi,t)$ as a linear combination of the normal modes, or eigenfunctions, of the unperturbed wave equation. The driving force acting on the film is then broken into components acting on each of the modes separately. After we specify a particular form for the damping term, the equation of motion for each normal mode may be solved separately, and the complete film motion obtained by summing the series. Typically, the driving force only couples strongly to a handful of modes, making the series easily tractable. Finally, knowing the motion of the film allows us to calculate the response at the detector, which we can compare to our experimentally obtained spectra.

One complication is the observation of resonant frequencies corresponding to azimuthally asymmetric modes. In order for the model to produce spectra with such features, we need to introduce an azimuthal asymmetry into the system. We hypothesized that the asymmetry in the experiment comes from the alignment of the plates, so we chose to represent the upper electrodes as tilted with respect to the substrate beneath it by an angle α . The amplitudes of the azimuthal modes is strongly dependent on this tilt angle, which we can use to estimate α by comparing of the observed spectra to our model results while varying α .

The calculations were carried out using Mathcad; a sample calculation for particular parameters is given in Appendix B.

Driving force. In the presence of a driving force and neglecting dissipative terms for the moment, the fluid equations are given by:

$$(\rho/d) \partial Z(\mathbf{r},t)/\partial t + \tilde{\mathbf{N}} \cdot (\rho_s \mathbf{v}_s) = 0 \quad (5.13)$$

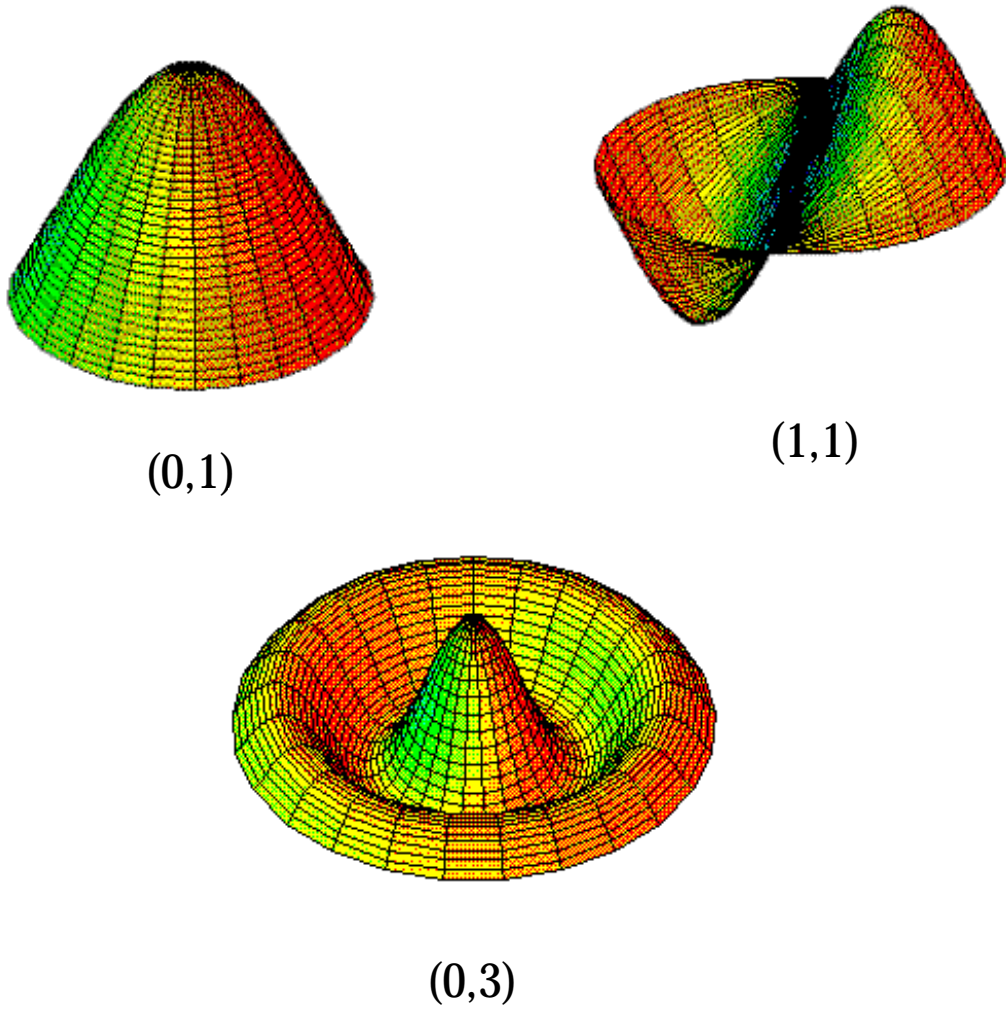


Figure 5.3 Shapes of modes corresponding to the indices (m,n) .

$$\partial \mathbf{v}_s / \partial t = - a_{vdw} \tilde{N} Z(\mathbf{r}, t) - (1/\rho) \tilde{N} p_E \quad (5.14)$$

where $p_E = \frac{1}{2} \epsilon \epsilon_0 E^2 e^{i\omega t}$ is the electric pressure on the film due to the electric field from the sinusoidal voltage applied to the drive plate. Note that a uniform electric field will produce no superfluid acceleration; only a gradient in the electric field will accelerate the liquid in the film. For our geometry, with an annular drive plate, the superfluid acceleration from the driving force will be limited to those regions with an electric field gradient, i.e. near the edges of the drive plate. In fact, when the spacing between the substrate and drive plate is x_0 , the acceleration $(1/\rho) \tilde{N} p_E$ is negligible outside a region of width $2x_0$ directly under the drive plate's edge.

The wave equation including this electric pressure becomes:

$$\partial^2 Z(\mathbf{r}, t) / \partial t^2 - c_3^2 \nabla^2 Z(\mathbf{r}, t) = (\rho_s / \rho^2) d \nabla^2 p_E \quad (5.15)$$

We will therefore define $F(\mathbf{r}, t) = (\rho_s / \rho^2) d \nabla^2 p_E$ and express the surface motion $Z(\mathbf{r}, t)$ and the driving force $F(\mathbf{r}, t)$ in terms of the normal modes of the system [Morse and Ingard 1968]. Here we will assume that only the $m=0$, azimuthally symmetric modes, are driven so there is no ϕ -dependence. The extension to azimuthally asymmetric modes is trivial. Without damping, we have

$$Z(\mathbf{r}, t) = \sum z_n J_0(\alpha_{0n} r / R) e^{-i\omega t} \quad (5.16)$$

$$F(\mathbf{r}, t) = \sum f_n J_0(\alpha_{0n} r / R) e^{-i\omega t} \quad (5.17)$$

where

$$f_n = (2/J_1(\alpha_{0n})^2) \int_0^R F(r) J_0(\alpha_{0n} r / R) (r/R^2) dr \quad (5.18)$$

The wave equation becomes

$$\sum [-\omega^2 z_n + c_3^2 k_n^2 z_n - f_n] J_0(\alpha_{0n} r / R) = 0 \quad (5.19)$$

So

$$z_n = - f_n / (\omega^2 - \omega_n^2) \quad \text{where } \omega_n = c_3 k_n \quad (5.20)$$

And the complete solution is

$$Z(\mathbf{r}, t) = \sum (-f_n / (\omega^2 - \omega_n^2)) J_0(\alpha_{0n} r / R) e^{-i\omega t} \quad (5.21)$$

This shows that the amplitude of motion of any particular normal mode is proportional to the overlap between the driving force and that normal mode, f_n . We have numerically calculated the electric field created between the drive plate and the substrate, and the electric pressure on the film with well-approximated by a constant F_0 within a region of width 44 microns slightly off-center of the edge of the drive plate when the plate separation is 30 microns. When we account for the tilt of the plates, the driving force coefficient will become a function of the tilt angle and the position on the substrate. [see Appendix B.]

Damping term. The hydrodynamic equations of motion for the film permit several different possible forms of dissipation, but for this model we generically write a single dissipation term $-\beta\partial Z(\mathbf{r},t)/\partial t$. The dissipation coefficient β need not be a constant; for instance, for damping due to second viscosity the coefficient would be $\beta_n = \rho_s \xi_3 k_n^2$, different for different normal modes. With damping, equation (5.20) is replaced by

$$z_n = -f_n / (\omega^2 - \omega_n^2 + i\omega\beta_n) \quad (5.22)$$

and the total solution becomes

$$\begin{aligned} Z(\mathbf{r},t) &= \sum (-f_n / (\omega^2 - \omega_n^2 + i\omega\beta_n)) J_0(\alpha_{0n}r/R) e^{-i\omega t} \\ &= \sum (-f_n / \sqrt{\{(\omega^2 - \omega_n^2)^2 + \omega^2\beta_n^2\}}) J_0(\alpha_{0n}r/R) e^{-i(\omega t + \phi_n)} \end{aligned} \quad (5.23)$$

where

$$\phi_n = \tan^{-1} (\omega\beta_n / (\omega^2 - \omega_n^2)). \quad (5.24)$$

Detector sensitivity. Having found the motion of the film, $Z(\mathbf{r},t)$, we can calculate the shape of the observed spectra. Our detector measures the net change of ^3He on the substrate underneath the inner disk. This can be expressed as:

$$\begin{aligned} \text{Signal} &= (1/\pi r_{\text{inner}}^2) \int_0^{r_{\text{inner}}} Z(\mathbf{r},t) 2\pi r dr \\ &= \sum (-f_n / \sqrt{\{(\omega^2 - \omega_n^2)^2 + \omega^2\beta_n^2\}}) e^{-i(\omega t + \phi_n)} \\ &\quad \cdot (1/\pi r_{\text{inner}}^2) \int_0^{r_{\text{inner}}} J_0(\alpha_{0n}r/R) 2\pi r dr \\ &= e^{-i\omega t} \sum (-f_n / \sqrt{\{(\omega^2 - \omega_n^2)^2 + \omega^2\beta_n^2\}}) e^{-i\phi_n} \\ &\quad \cdot 2J_1(\alpha_{0n}r_{\text{inner}}/R) / (\alpha_{0n}r_{\text{inner}}/R) \\ &= e^{-i\omega t} A(\omega) e^{i\theta(\omega)} \end{aligned} \quad (5.25)$$

We can compare the calculated $A(\omega)$ to the amplitude of the response in our swept frequency measurement, and $\theta(\omega)$ to the phase of the response relative to the driving force. In Figure 5.4, we see the spectra predicted by the model using input values of $c_3 = 5$ cm/sec, $\beta = 1$ Hz, and a tilt of $\alpha = 1$ mrad. We will compare this to the observed spectra in Chapter 7, after presenting the experimentally observed spectra of third sound in Chapter 6.

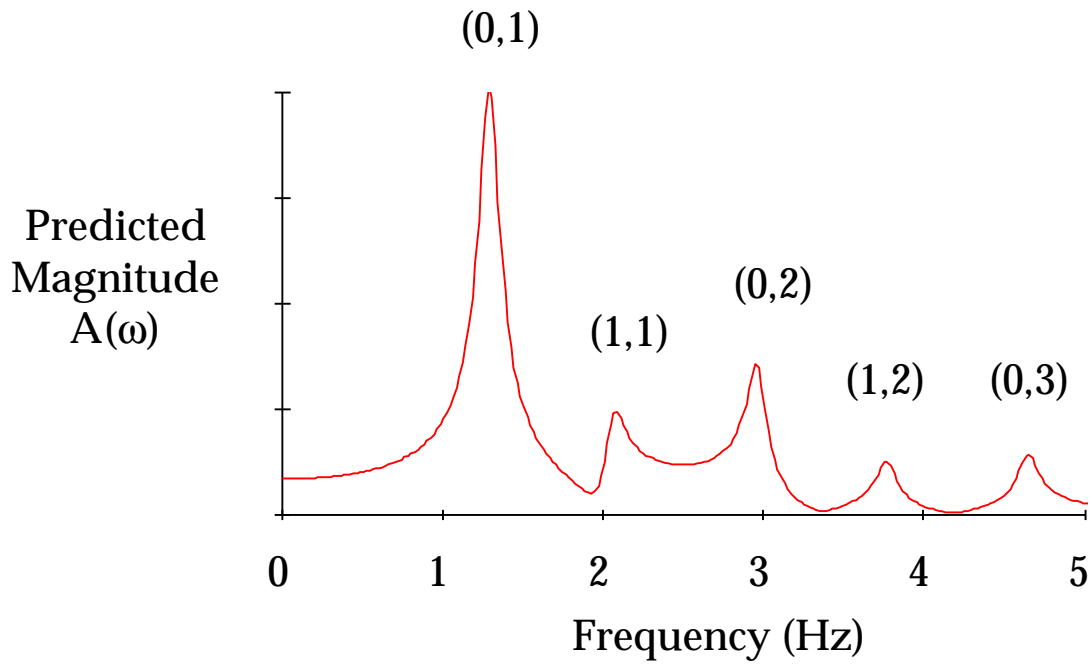


Figure 5.4 Sample spectra generated from the model. The spectra predicted by the model discussed in the text, for $c_3 = 5$ cm/sec, $\beta = 1$ Hz, and a tilt of $\alpha = 1$ mrad.

Chapter 6. Experimental Results

In this Chapter, we will describe the experimental results obtained. First, we describe experiments performed on saturated films of superfluid ^4He to test the apparatus and lay a groundwork for our observations in ^3He films. Second, we discuss measurements of the film thickness as a function of the height from the film to the free surface of the bulk liquid. Third, we present and discuss the spectra of third sound resonances obtained in superfluid ^3He films as a function of film thickness and temperature.

A. Third sound spectra in superfluid ^4He

As a prelude to our experiments on superfluid ^3He films, we first carried out two experiments on ^4He films. These served as a proof-of-method and helped us to understand the responses we observed from ^3He films. Third sound in ^4He films is well-understood, forming a useful basis of comparison for our observations in ^3He films. The first experiment [Schechter *et al.* 1998a] (using a slightly different experimental cell than the following ^3He experiments), measured a set of spectra in a pumped bath at 1.4 K for a range of film thicknesses. The dominant peaks in the spectra fit well to the expected ratios for Bessel-shaped modes, and the speed of third sound obtained from the modes appeared to fit the expected function of h well. The second experiment was carried out in the ^3He experimental cell on the dilution refrigerator, using a heater to vary the film's temperature from ~ 10 mK to 2.2 K. At the very low temperatures, the small dissipation caused several modes to appear with very high quality factors; these enabled us to identify clearly the natural boundary conditions for ^4He third sound resonances on our substrate. As we raised the temperature, the Q 's of the resonances fell, and the spectra acquired several unexpected features which we also observed in later ^3He spectra.

i. First experiment with ^4He films

The first experiment was intended to test the operation of a circular third sound resonator with saturated ^4He films. The experimental cell was cooled on a probe in a ^4He pump bath down to 1.4K, but the major significant differences between it and the ^3He cell relate to the substrate surface and thermal contact inside the cell. The substrate in the first ^4He test was a copper disk whose top surface had been machined with a diamond-tipped cutting tool and then covered with a flat gold coating between 0.1 and 0.2 microns thick.¹¹ The gold coating was intended to prevent the formation of oxides on the substrate. AFM images of this surface showed it to have an rms roughness of about 10 nm. The coating extended to within 0.5 mm of the circular edge, which was rounded with a radius of curvature of 0.3 mm. In contrast to the substrate surface, the rounded edge was rough, having scratches on the 10 micron scale. The thermal link to this piece was made by pressing the bottom surface of the copper disk tightly against a gold-plated

¹¹ II-VI Incorporated, 375 Saxonburg Blvd, Saxonburg, PA.

copper holder. The pressure was applied by tightening 4 brass screws into threads in the bottom of the copper disk. The holder was supported by a 3" long, 1/4" OD post which was itself clamped to a silver-sinter heat exchanger which was submerged in the liquid helium of the bath.

While the tests of this first experimental cell in ^4He were successful, the first trials using it with ^3He at sub-mK temperatures were not. We were unable to generate voltage-driven film flow in this cell, despite cooling the liquid bath below the expected value of T_c^{film} . We did observe a spontaneous out-flow of material from the substrate below T_c^{bulk} , presumably ridding the film of excess helium deposited during the cell-filling process, but we were unable thereafter to excite motion in the resulting (thinner) film. We observed no film flow in response to applied voltages, either from the bulk liquid onto the substrate or from one part of the substrate to another. The reason for this is unclear. One possibility is that the residual film was left in a superfluid phase with a near-zero critical current [Thuneberg 1987], which prevented our observing film motion. Another possibility is that after the initial out-flow, the film was never cooled enough to become superfluid. The initial out-flow occurred just below T_c^{bulk} , since the critical temperature for the very thick film approaches the bulk temperature; thereafter the film was thin enough to suppress T_c^{film} greatly and increase the thermal resistance through the film to the bulk. However, this model fails to explain the point at the end of the out-flow, when the film has either just reached equilibrium or the film has just thinned through T_c^{film} . Cooling further from this point should then have allowed us to manipulate the film, which we were not able to do. Whatever the reason, this failure motivated a modification of the cell innards with two aims: improve the thermal contact to the components inside the cell and return to a substrate surface on which we had observed superfluid ^3He film flow. We discarded the diamond-tool lathed, gold-covered substrate in favor of a simple mechanically polished copper substrate on a disk with a large silver-sinter heat exchanger built into its opposite side, as described in Chapter 4. With this change to the experimental apparatus, a superfluid ^3He film was successfully produced and superfluid film flow measurements were carried out, as noted in our paper [Schechter *et al.* 1998a] on the third sound resonator. It would be interesting to return to the diamond-tool lathed, gold-covered substrate at some point in the future to study the peculiar behavior we observed.

The results of the first ^4He experiment were important, however. Figure 6.1 shows a set of resonance spectra taken at 1.4 K for a range of film thicknesses from 43 nm to 85 nm. These thicknesses were determined directly from the change in the plate capacitance when adding ^4He to the cell. This is thinner than the thinnest pure ^3He film in the later experiments; the range of heights from the film to the bulk surface was 2 mm to 55 mm, outside the range explored with ^3He films. It would have been desirable to work with thicker films, since we were aware that superfluidity in ^3He films was suppressed for thin films; however, the low viscosity of the superfluid ^4He and the vibrationally noisy environment of the pump bath caused the experimental plates to fill completely with ^4He whenever the height of the liquid bath was raised to within 2 mm of the film substrate. We assumed correctly that for the ^3He , mounted on the dilution refrigerator, we would be able to raise the liquid level much closer to the film substrate without such a catastrophic filling of the plates occur. (In ^4He , U-tube oscillations of the

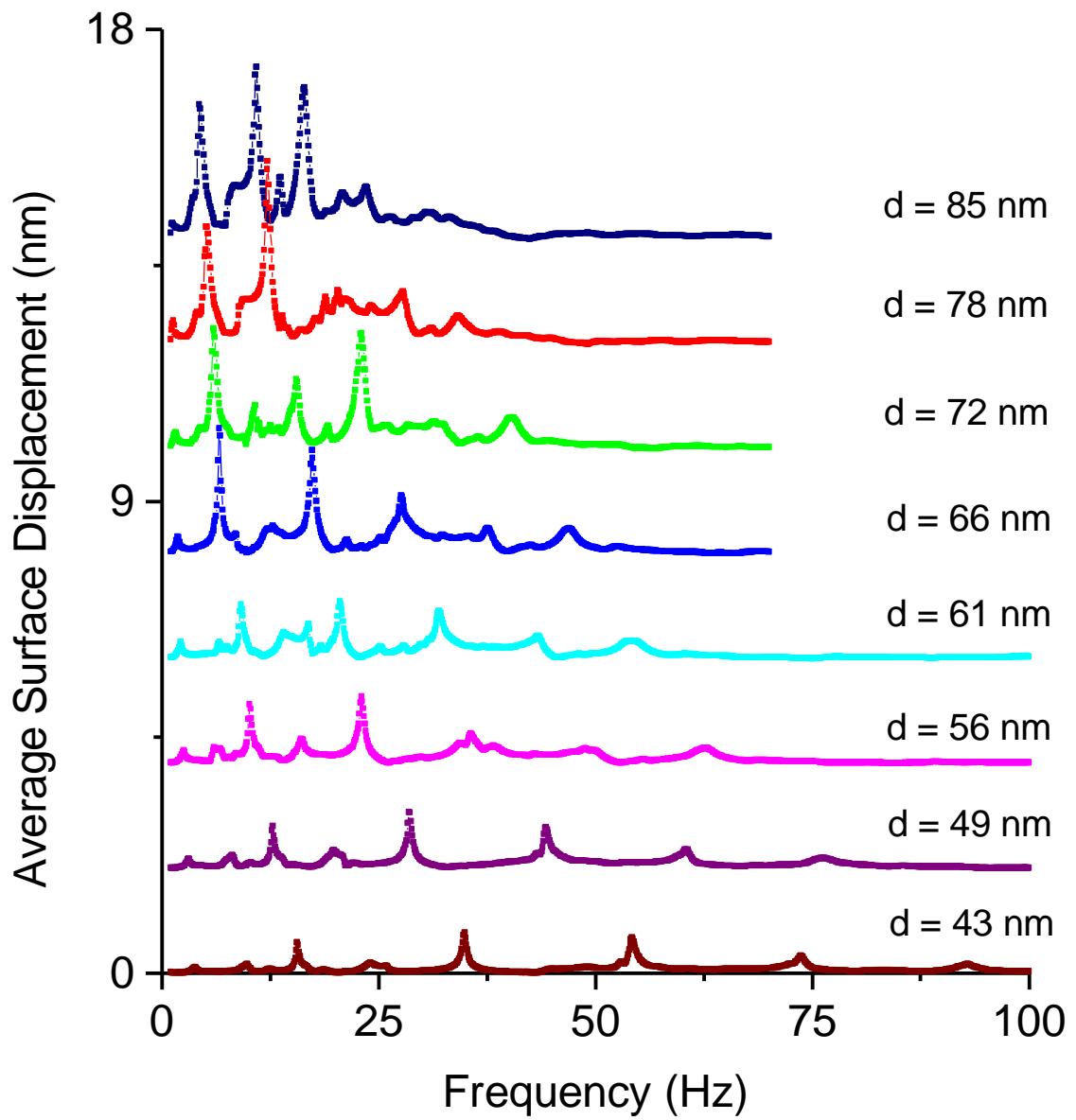


Figure 6.1 Spectra of third sound observed in ^4He films at 1.4 K.

surface have extremely little damping, so the bulk liquid can slosh up onto the substrate; in ^3He , the damping mechanism related to motion of the normal fluid at the surface [Brand and Cross 1982] makes any such sloshing highly over-damped.) For each of these spectra, we were able to identify a set of peaks whose frequencies correspond to the zeros of the $J_0(x)$ Bessel function; in other words, the ^4He third sound standing waves on this substrate were governed by a 'fixed' boundary condition. Using these frequencies and linear dispersion relation (from equations 5.9 and 5.11)

$$f_{0n} = (\alpha_{0n}/2\pi R) c_3 \quad (6.1)$$

we were able to determine the velocity of third sound for the ^4He film as a function of film thickness. Figure 6.2 shows this result by graphing the square of the third sound velocity vs the height h . (Note that Figure 6.2 includes additional data that is not shown in Figure 6.1, taken at lower film coverages and correspondingly larger heights h .) This data fits well to the expected relation given by equation

$$c_3^2 = (\rho_s/\rho) n g h \quad (6.2)$$

where $n = 4$ is the exponent of the van der Waals power law. (This relation will be derived later, in section 2.B.)

At the time we published this data, the $n = 4$ power law did not strike us as very surprising. The Lifshitz theory of the van der Waals force [Dzyaloshinskii *et al.* 1961], including the effects of retardation, predicts that as films become thicker the exponent should vary from $n = 3$ to $n = 4$, with the transition film thickness being about 40 nm. For unsaturated ^4He films only a few monolayers thick (which are used in many third sound experiments) the theory's prediction of $n = 3$ is well established. Sabisky and Anderson [Sabisky, Anderson 1973], in their experimental work verifying the Lifshitz theory for these very thin films, showed clear deviations from the $n = 3$ law for films thicker than 10 nm. [Cheng and Cole 1988] found an empirical relation for $h(d)$ between these two regimes. Since our films were much thicker, we expected the $n = 4$ power law which we observed, and we expected that our data for ^3He films would also show an $n=4$ power law for the van der Waals force, since we would necessarily be working with even thicker films of ^3He to achieve superfluidity. As we will discuss, this did not turn out to be the case exactly.

This first test with superfluid ^4He films showed us that we could capacitively generate and detect third sound resonances in saturated films of helium, using the experimental technique we have described. The spectra of resonances obtained from the film matched the expected ratios of Bessel zeros and allowed us to measure the speed of third sound waves in these films. The speed obtained agreed with Everitt's original data [Everitt *et al.* 1964] on thick films of superfluid ^4He , and varied with height from the bulk surface in the expected manner. Furthermore, with a slight modification of the cell to improve the thermal contact between the nuclear stage and the substrate, we were shortly thereafter able to observe superfluid ^3He film flow in this apparatus.

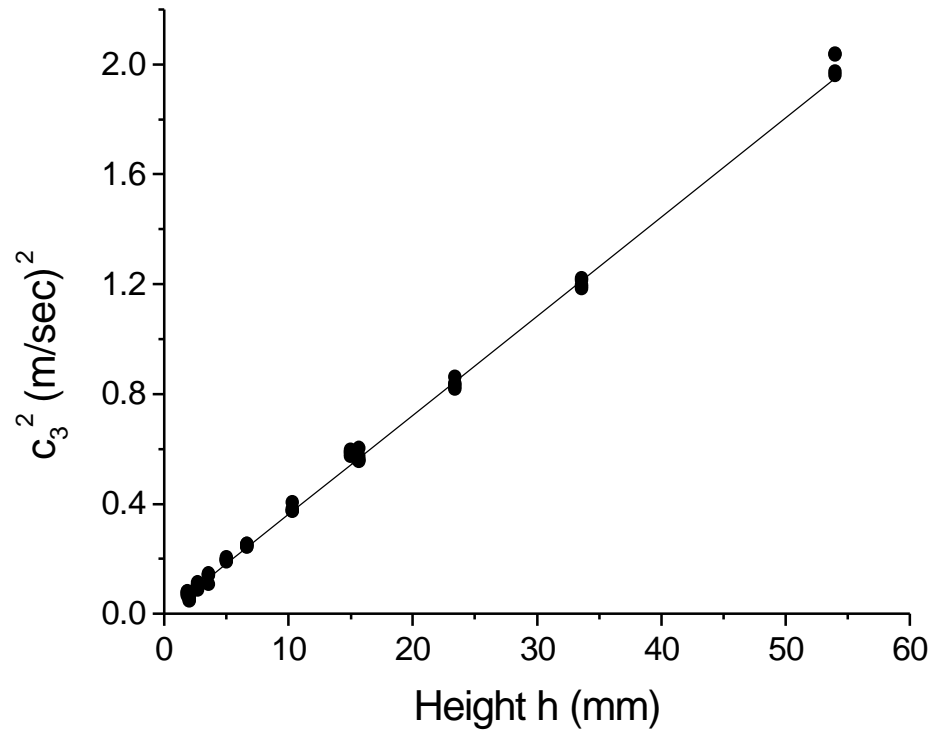


Figure 6.2 c_3^2 vs h in ^4He . Speed squared of third sound in ^4He vs the height from the film to the bulk surface. The line shows the expected relation (equation 6.2) when the van der Waals exponent takes the value $n = 4$.

ii. Second experiment with ^4He films

After mounting the experimental cell on the dilution refrigerator, we filled it with liquid ^4He to form a film with $d = 128$ nm and measured the third sound spectra as a function of temperature from 10 mK up to 2.2 K.

Figure 6.3 shows the spectra of third sound taken at about 10 mK. At this temperature, the superfluid fraction $\rho_s/\rho = 1$ for ^4He , and the speed of third sound is expected to be about $c_3 \sim 14$ cm/sec (using Daunt's value for the van der Waal's coefficient [Daunt *et al.* 1988]). Overlaid on the spectra are vertical lines representing the expected frequencies of the resonant modes. The strongest peaks in this spectrum fall on the values given by equation 6.1, however, in addition there are clear (smaller, but still above the noise floor and separate from identified noise peaks) peaks in between each pair of the strongest peaks. These fall on the frequencies which are given by (from equations 5.9 and 5.11)

$$f_{1n} = (\alpha_{1n}/2\pi R) c_3 \quad (6.3)$$

where the zeros correspond to the $m = 1$, azimuthally asymmetric modes instead of the $m = 0$ symmetric modes. The data from the first experiment, in the pump bath, also shows these modes though they were not recognized as such at the time.

Figure 6.4 shows the spectra of third sound in ^4He near 2 K, where the damping has become significant. Overlaid is a spectra taken for a ^3He film at 0.35 mK, where the frequency axis has been scaled so that the fundamental modes overlap. The spectra have important similarities. The modes identified with the α_{11} and α_{02} zeros are present in both materials, as is the structure between "6" and "7" Hz. The α_{03} mode appears to be present in both, although greatly suppressed in the ^3He film. Most interesting, the structure on the left shoulder of the α_{03} mode is entirely absent in the ^3He film. The expected frequency of the α_{12} mode is actually between the peak at 7 Hz and this shoulder; the peak only appears in the spectra for high temperatures in ^4He and very low temperatures in ^3He . This is still not well-understood.

B. Film thickness vs height of the bulk liquid

Thickness measurements for films on rough surfaces are known to be problematic [Brewer 1978 p.577-594]. The substrate on which we observed third sound waves has roughness on the scale of 250 nm, comparable to the thicknesses of the films. This is unfortunate, since the most natural parameter with which to characterize films is their thickness, and their properties, like the average superfluid density, depend relatively strongly on the film thickness. Nonetheless, previous work [Davis 1989] with saturated films on substrates comparable of roughness, even going back to the discovery of third sound in ^4He by Everitt, Atkins, and Denenstien [Everitt *et al.* 1964], have relied on the alternative parameter h , the height from the free surface of the bulk liquid to the film. We have followed this precedent; however, in this section we discuss our effort to measure the dependence of the observed film thickness on h .

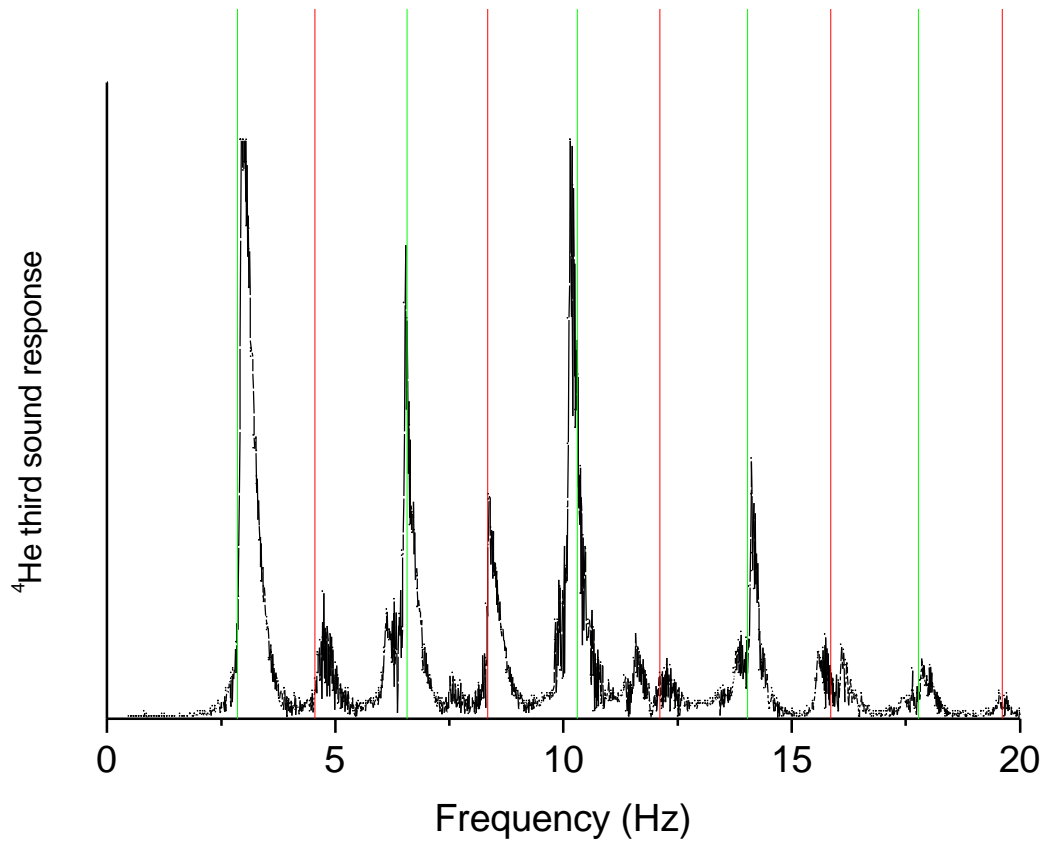


Figure 6.3 Spectra of ^4He third sound near 10 mK. The odd-numbered (from the left) vertical lines represent the α_{0n} Bessel modes (fixed boundary, azimuthally symmetric) and the even-numbered lines represent the α_{1n} Bessel modes (fixed boundary, azimuthally asymmetric).

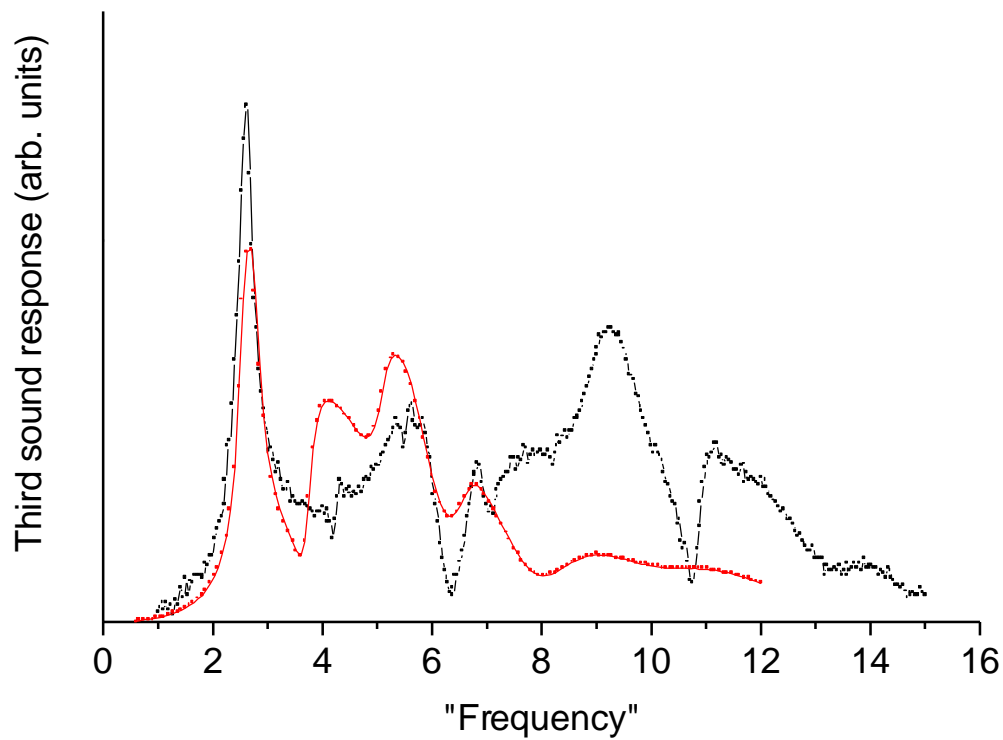


Figure 6.4 Comparison of ^3He and ^4He spectra. The curve extending to higher "frequency" shows the third sound response in a 140 nm film of ^4He near 2 K; the x-axis shows the proper frequency for this curve. The other curve shows the third sound response in ^3He at 0.33 mK, in a 233 nm film; the data has been scaled along the frequency axis so that the fundamentals of the two data sets line up. The vertical scaling of the two curves is arbitrary and different for each.

As we have discussed, we use a capacitive level detector to measure the height of the liquid inside the cell and use the capacitance between the substrate and the detection electrode to measure the thickness of the ^3He film. In measuring the thickness, we neglect the effect of surface roughness and assume that the film thickness is equal on the substrate and on the detection electrode. (Since the film on the upper electrodes is actually 30 microns higher than the film on the substrate, we would expect it to be thinner. However, for the heights used in this test, this leads about a 1-2% correction in the film thickness, which we have neglected.)

The film is formed on the copper substrate below the drive and detection electrodes by filling the cell with liquid ^3He until the level of the free surface of the bath is just below the level of the substrate. The liquid at this point is out of equilibrium, but cooling down below T_c will allow superflow to redistribute the liquid in the cell to reach its desired equilibrium. As discussed in Tilley and Tilley [Tilley and Tilley 1986 p.93], the situation can best be analyzed in terms of the chemical potential per unit mass, which must be a constant everywhere on the liquid's surface. The chemical potential per unit mass can be written as

$$\mu/m = p/\rho - \sigma T + gz - g(\alpha/d)^n \quad (6.4)$$

where p/ρ is the pressure divided by the density, σT is the entropy density per unit mass times the temperature, gz is due to gravity, and the last term is due to the van der Waals attraction between the helium liquid and the wall [Tilley and Tilley 1986 p.93]. The van der Waals constant α is material dependent, and the gravitational acceleration g is included in this term as a convenience. (This constant is defined differently by various authors.) The exponent n of the van der Waals potential is predicted [Dzyaloshinskii *et al.* 1961] to vary from 3 to 4 as will be discussed shortly.

Consider the chemical potential at points A and B in Figure 6.5. At point A, on the free surface of the liquid bath far from the wall, we have $z = 0$, $d = \infty$, $p = 0$ and $T = T_0$. (We are also far enough away to neglect the effect of surface tension, which only contributes to the chemical potential where the surface has curvature. See [Steel *et al.* 1994] for a discussion of surface tension in these films.) At point B, on the film's surface on the substrate, we have $z = h$, $d =$ the film thickness, $p = 0$, and $T = T_0 + \Delta T$, where ΔT is the temperature difference between the film and the bulk liquid. We neglect this temperature difference, which we believe is small. (The entropy density per unit mass σ falls rapidly as we go down in T from T_c ; near T_c , a temperature difference of 10 μK gives a contribution to the chemical potential equivalent to about a 10 micron change in the height.) Setting $\mu_A = \mu_B$, we find that

$$0 = gh - g(\alpha/d)^n \quad \text{or} \quad h = (\alpha/d)^n \quad (6.5)$$

Measuring $h(d)$ therefore allows us to determine the van der Waals attractive potential per unit mass, $U_{\text{vdW}}(x) = g(\alpha/x)^n$ and of particular importance, the van der Waals acceleration given by

$$a_{\text{vdW}} = - dU_{\text{vdW}}/dx = ng\alpha^n/d^{n+1} = ngh/d. \quad (6.6)$$

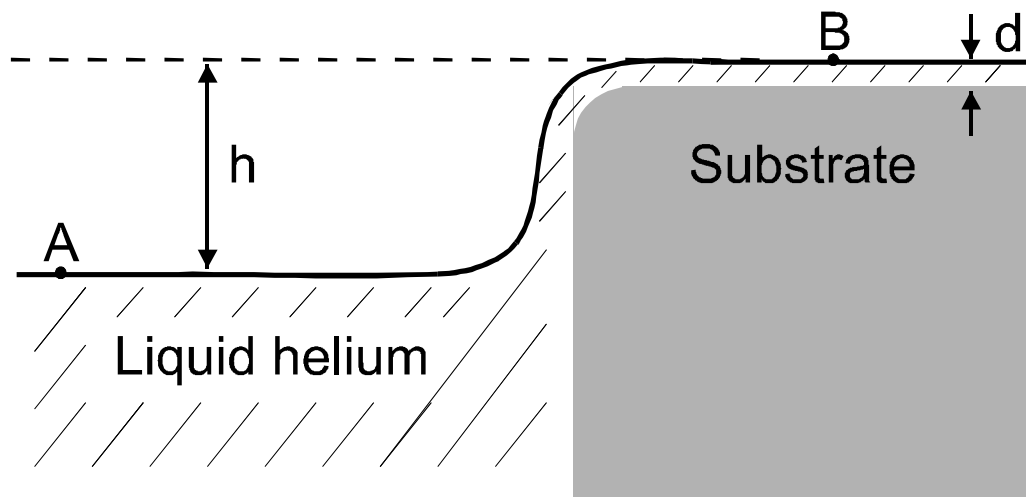


Figure 6.5 Sketch of the film - bulk liquid interface. Profile of the helium film rising a height h from the free surface of the bulk liquid at point A to the surface of the film at point B, where the film has thickness d .

This implies, as long as the attractive force holding the film to the substrate can be well-described by a simple power law, that the speed of a third sound wave will take on the simple form

$$c_3^2 = (\rho_s/\rho) a_{vdw} d = (\rho_s/\rho) n g h \quad (6.7)$$

which removes the explicit dependence on the film thickness and on the magnitude of the attractive force, replacing it with an overall factor n which is the exponent of the power law of the attractive force.

A review of the theory and experiments on the thickness of helium films and on the van der Waals attraction is given by [Brewer 1978]. The most successful theory of adsorbed helium films was given by Dzyaloshinskii, Lifshitz, and Pitaevskii [Dzyaloshinskii *et al.* 1961] predicting the relation $h \sim d^{-3}$ for very thin films ($d < 10\text{nm}$) and $h \sim d^{-4}$ for thick films ($d > 40\text{nm}$), due to the effect of retardation on the electromagnetic interaction. They gave an expression in the intermediate range depending on the dielectric functions of the helium film and the material of the substrate. The subsequent experiment by Sabisky and Anderson [Sabisky, Anderson 1973] with thin-to-intermediate ^4He films ($d < 25\text{ nm}$) on an atomically smooth alkaline-earth fluoride (SrF_2) substrate agreed with considerable accuracy for thicknesses from 1 nm to 25 nm, and since that time the Lifshitz theory has been generally accepted.

The film thickness of a ^4He film and a ^3He film on identical substrates, the same distance above the bulk liquid, are expected to be not quite identical. Assuming that the van der Waals potential per atom is the same for ^3He or for ^4He , the only difference would be the mass of the two isotopes, so the van der Waals coefficients α_3 for ^3He and α_4 for ^4He would be related by $\alpha_3 = (4/3)^{1/3} \alpha_4$. Many researchers have measured α_4 for ^4He , using $U_{vdw}(x) = g(\alpha_4/x)^3$ and finding values of about $10^{-8} \text{ m}^{4/3}$ for a variety of surfaces, copper, glass, and stainless steel of various conditions [Daunt *et al.* 1988]. However, difficulties persist in using the Lifshitz theory to predict film thicknesses quantitatively. The details of the surface preparation and roughness can have enormous effects on the observed film thickness; highly polished surfaces tend to have apparent film thicknesses closer to the Lifshitz value, while roughened or contaminated surfaces may have apparent film thicknesses several times larger [Brewer 1978].

In our initial report on the observation of third sound, we reported a value of $\alpha_3 = (10.0 \pm 0.4) \times 10^{-9} \text{ m}^{4/3}$. This was obtained by fitting the $h(d)$ data to the van der Waals potential with the power law $n=3$, with 1 point acquired for each film thickness at which we performed a third sound measurement. This method was not ideal, since it obtained only a handful of data points, and it was susceptible to the DC drift of the capacitive measurements of the film thickness over long periods of time. In order to improve this measurement, we added to the cell a bellows volume changer, described in Chapter 4, which is capable of changing the height h of the liquid inside the cell continuously while remaining below T_c^{film} . With this apparatus, the procedure for carrying out the measurement of $h(d)$ was as follows. We would fill the cell with liquid ^3He to some level. We would then cool below the superfluid transition temperature of the film, so that superflow would allow the film thickness to come quickly into the equilibrium governed by the van der Waals force and gravity. Actuating the bellows, we would slowly (over several hours) lower the liquid height while monitoring the change in the film thickness.

We could thereby make the measurement continuously and over a short enough period of time that DC drift is not a problem.

The data that we obtained, Δh vs Δd , can be converted into an $h(d)$ curve. The level detector capacitance ΔC is related to the height of liquid inside it ΔH , by $\Delta C/\Delta H = 0.0991$ pF/mm, determined by measuring the total height of the level detector and the total capacitance change when it is filled with ^3He . The height from the bulk surface to the substrate is given by $h = H_0 - H$, where H is the vertical height of the liquid in the cell measured from the bottom of the capacitive level detector, and H_0 is the height of the film on the substrate. To determine H_0 , we raised the liquid level slowly until we observed the plates abruptly fill with liquid at $H_{\text{filling}} = 16.128 \pm 0.004$ mm. However, this is only a minimum value for H_0 , due to a possible systematic error: if the plates are not horizontal with respect to gravity, then the height H_{filling} at which the liquid overflows onto the substrate would be lower than H_0 . For each film, we record the height $h = H_{\text{filling}} - H$, but the actual value $H_0 - H$ could be slightly higher. To estimate how large this effect could be, we note that the copper bar of the nuclear stage is at an angle of 1.5 mrad with respect to a vertical plumb-line; if the substrate was perpendicular to the nuclear stage, this would result in the center of the substrate being about 30 μm higher than its lowest edge. This effect introduces a systematic error on our measured values of n and ρ_s/ρ , as we will discuss below. (The substrate slanting in this manner would also cause a gradient in the film thickness across the substrate. In future experiments with multiple capacitor plates covering the substrate, it should be possible to remove the slant by adjusting the heights of the legs of the cryostat table until the observed film thicknesses under each plate agree with each other.)

The initial thickness d_0 of the film was measured as the difference in the capacitance of the empty plates and the capacitance of the plates after filling with ^3He . This difference was $d_0 = 214 \pm 5$ nm, with the uncertainty arising from the potential for DC drift between the two measurements. The film thickness d is then given by $d = d_0 + \Delta d$. A second run of the experiment, two days later, covering an overlapping-to-smaller range of heights h , measured values for the film thickness which were 6.75 nm larger than on the first run in the overlapping range; this was attributed to DC drift in the capacitance bridge and the offset was subtracted from the second data set. Figure 6.6 shows this data on a log-log scale. The data fits to a power law of $n = 3.44 \pm 0.08$, and the relationship between h and d is found to be $h = ((176.8 \pm 0.2) / d)^{3.44}$ where h is measured in mm and d is measured in nm. The uncertainty in the value of n arises from the uncertainty in d_0 . The uncertainty in H_0 discussed above due to a possible tilt of the plates leads to a decrease in n of about 0.06 for each 10 μm of height difference between the center and lowest edge of the substrate.

However, more fundamental problems which researchers have had in measuring film thicknesses come into play as well. The film thicknesses observed during this later run do not agree well with the previous run (during which the third sound spectra were obtained) for similar values of h . For the initial value of $h = 0.518$ mm, we observed $d_0 = 214$ nm whereas in the previous run the thickness would have been about 125 nm. In the interim, the cell had been warmed to room temperature and the bellows volume changer had been attached to it. This required opening and resoldering the fill line, though not directly exposing the inner components of the cell. One possible explanation for the discrepancy in the measured film thicknesses could be that during the

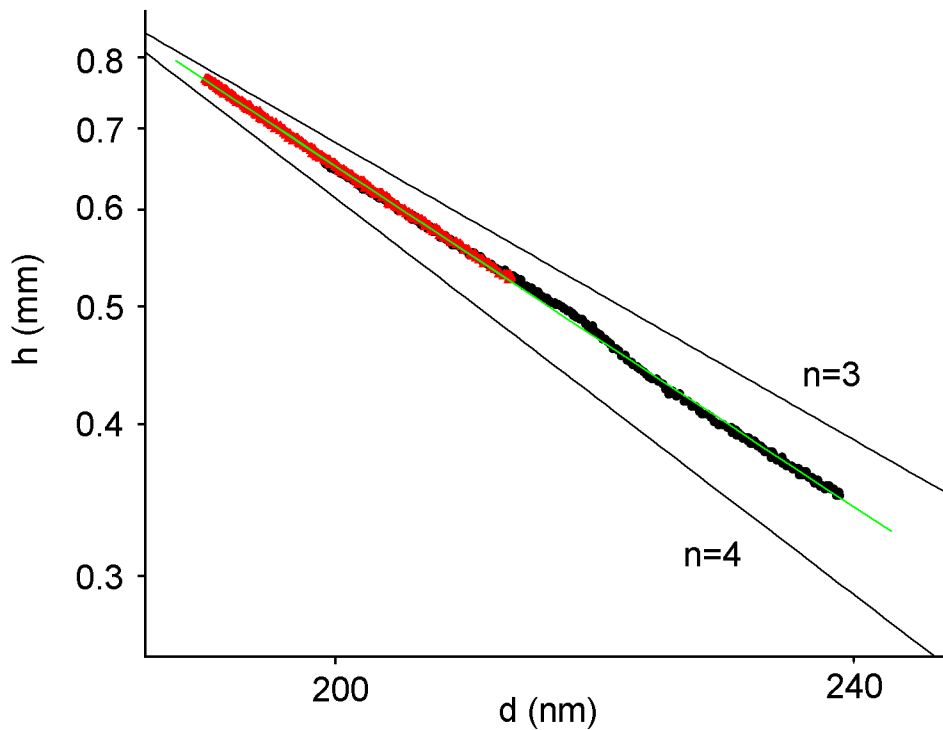


Figure 6.6 Film thickness vs height from the free surface to the film. (Log-log graph.) Two data sets, taken on different days, are shown: the first from $h = 0.53$ mm to $h = 0.77$ mm, then two days later from $h = 0.35$ mm to $h = 0.66$ mm. Curvature in second data set from $h = 0.4$ mm to $h = 0.5$ mm is due to the film being slightly out of equilibrium, with h changing more rapidly than d can change by critical-current-limited film flow. The fit shown gives a power law of $n = 3.44$. For comparison, lines with slope $n = 3$ and $n = 4$ are shown.

soldering process contaminants were deposited on the substrate which acted to increase the effective surface roughness; in the experiment of [Fehl and Dillinger 1974] it was observed that rougher surfaces could have twice the apparent film thickness as smoother ones. (Another difference in the second run was a small amount of ^4He in the cell, as part of the experiments described in Chapter 8, section A, but this should not cause such a large effect.)

This makes characterizing the third sound wave in terms of the measured film thickness problematic. Using the height h as the key parameter, and relying on equation (6.2) for the speed of third sound evades the difficulty by concealing the explicit film thickness dependence, but it does not remove the dilemma completely since the third sound speed depends on the actual film thickness, not an effective film thickness derived from h . Nonetheless, we will characterize our films in this manner, as has been done in work on saturated films since the first observation of third sound in ^4He by [Everitt *et al.* 1964]. We will use the value $n = 3.44$ derived from the experiment using the bellows to obtain the average superfluid density of the film using equation (6.2), keeping in mind that this could introduce a consistent error of up to $\sim 15\%$ in the derived quantity.

C. Resonant spectra of third sound in superfluid ^3He

We will now present the spectra we obtained showing resonant standing waves of third sound in superfluid ^3He , after describing the procedure used to acquire them during a typical data-taking run.

i. Method for obtaining third sound spectra

We will now describe a typical run recording third sound spectra. We would first cool the dilution refrigerator and the empty experimental cell to about 6 mK, then fill the cell with the desired amount of liquid ^3He keeping the temperature at the cell below a few hundred mK where the ^3He vapor pressure is very small (to minimize vapor deposition onto the substrate). We would next magnetize the copper bar of the nuclear stage, pre-cool for 1-3 days until we reached some 10-13 mK, and demagnetize. Just before arriving at T_c^{bulk} , we would transfer liquid helium into the main bath of the dewar, check the calibration of the NMR thermometer, and then demagnetize further through T_c^{film} . At this point superfluid flow would spontaneously begin, bringing the film's thickness into equilibrium with the height of the liquid in the bath. Once this equilibrium was established, we would record third sound spectra while slowly ramping the temperature down the refrigerator's base temperature and back up to T_c^{film} . After a satisfactory set of spectra had been obtained, we would close the heat switch to the dilution refrigerator, add some more ^3He to the cell to obtain a thicker film, and repeat the process starting at the magnetization. In later experiments with the bellows volume changer in place, the film thickness could be varied while remaining below T_c^{film} , without the need to remagnetize which adding ^3He from room temperature inevitably entailed.

We monitored the cell-filling process by tracking the volume of ^3He gas going into the cell, the warming of different stages in the refrigerator by the condensing gas,

and the arrival of liquid ^3He at the cell on the capacitive level detector and the experimental plates. The filling process would begin with us allowing pure ^3He gas to enter the cell's filling line, after passing through a liquid nitrogen cold trap. The rate at which the gas entered the fill line was controlled with a needle valve. The fill line in the liquid helium bath outside of the vacuum can has a coiled section of 1/4" OD, 1/8" ID copper tube whose width prevents any solidified air or other contaminant from dangerously blocking the fill line. Inside the vacuum can, the fill line is composed of sections of copper nickel tubing (of various sizes from 50 mil down to 10 mil OD) connecting a series of silver sinter heat exchangers. The heat exchangers are on the still plate, the cold plate, and the mixing chamber plate, and the copper nickel tube from this last heat exchanger delivers the ^3He to an entry-point at the base of the experimental cell. Resistance thermometers mounted on these stages would show the passage of the ^3He , and once the liquid level had reached high enough in the cell, its arrival could be detected by the capacitive level detector. During this process, the capacitive sensors of the experimental plates would react, either from bursts of ^3He gas arriving at the cell or from temperature changes (perhaps affecting the bridge's reference capacitor, thermally lagged to the ^4He pot). The net change in the plate capacitance at the end of cell-filling was generally only a few nm of film thickness, presumably from vapor deposition. However, we observed during the pre-cool that the plate capacitance would increase by $\sim 30\text{-}40$ nm of ^3He film (on each plate) as normal-fluid flow would slowly creep onto the plates at a rate of about 12-16 nm/day. This normal fluid flow rate was about 200 times slower than the spontaneous superfluid in-flow which appeared as we cooled through T_c^{film} .

We have already discussed the magnetization, pre-cool, and demagnetization procedures in an earlier section. One difficulty we faced was a long thermal time constant to cool the liquid down below $0.5 T_c^{\text{bulk}}$, caused by a combination of the inefficiency of the nuclear stage heat exchanger and the modest thermal heat leak to the nuclear stage. As a result, it would take 15-20 hours to reach the base temperature of the refrigerator after demagnetizing to a very low field. Meanwhile, the length of time which we could stay below T_c^{bulk} was limited by another difficulty: even the most gentle transfer of liquid helium into the bath stood a good chance of causing the superfluid ^3He to completely fill the plates. So to maintain the film, we had to warm above T_c^{bulk} every 1 1/2 days to transfer.

After cooling below T_c^{film} , a film of thickness d forms on the substrate. The third sound drive is applied and the film is cooled further until peaks in the spectra can be clearly seen and their frequencies identified. (The circuit used to take spectra of third sound resonances has already been discussed in the Chapter 4.) At this point the amplitude of the drive was varied to look for a non-linear response in the spectra. A typical applied drive was $V = 10V + 1V \sin\omega t$; increasing the amplitude of either the DC or AC component of the drive beyond these typical values would cause the response amplitude to increase less than proportionally and cause the resonant frequencies to shift to lower values. We attributed these effects to over-heating the film and chose a drive level as large as possible without departing too far from a linear response.

The frequency was stepped from 0.2 to 8 Hz in increments of 0.015 or 0.025 Hz. At each frequency the amplitude of the surface response was measured after a sufficient time had elapsed for any resonances to ring up and for the lock-in to settle. The amplitude vs frequency graph obtained in this fashion constitutes one spectrum for the

film at the temperature given by the weighted average of the (several) NMR thermometry readings taken during that sweep. These sweeps were repeated as the temperature of the film was continuously lowered by a slow demagnetization. Consecutive spectra have average temperatures which are typically about 15-20 μK different.

ii. Third sound spectra

Third sound spectra were recorded for a range of heights ranging from $h = 40$ microns to 1.053 mm, over a range of temperatures from T_c^{bulk} down to $T/T_c^{\text{bulk}} \sim 0.37$. These spectra are shown in Figure 6.7a, b, c, d and e for progressively thicker films. Each graph shows a set of spectra, with the highest temperature spectrum at the bottom and successive spectra (at approximately even intervals) offset vertically up to the coldest temperature spectra.

Above T_c^{bulk} , the films show no response to the applied driving force. At some temperature T_c^{film} (below T_c^{bulk}), which varies for each film, we begin to detect a response from the film at very low frequency. The typical noise level for these spectra when above T_c^{film} is about 5-10 pm average surface displacement; we see film motion exceeding the background noise at low frequencies well before discernable resonances begin to appear. This is the expected behavior, since the amplitude and resonance frequencies should both be zero just as T falls below T_c^{film} . As the temperature falls, we see three things: a well-defined set of resonant modes appear, the amplitude of these modes increases, and the resonant frequencies increase.

The resonant modes which we observe vary continuously as a function of both temperature and film thickness. Within any of the spectra, it is clear that the resonances vary smoothly (though not always in a simple manner) from higher temperatures just below T_c^{film} down to the lowest accessible temperature. To see the continuous change as a function of film thickness, proceed sequentially through the graphs observing that low-temperature features in a thin film become higher-temperature features in a slightly thicker film. For instance, a miniaturized version of the $h = 0.394$ mm spectra is contained in the higher-temperature half of the $h = 0.263$ mm spectra. We will rely on this continuity when we interpret the spectra in the next Chapter.

The amplitude of film motion for all the films increases as the temperature falls and as the films get thicker. For the thinner films, shown in Figure 6.7a and b, the maximum average surface displacement near 0.35 mK grows from $\sim 1 \text{ \AA}$ to $\sim 5 \text{ \AA}$ as the thickness of the film grows. (Smaller heights h imply thicker films.) For the thicker films, shown in Figure 6.7d and e, the low-temperature amplitudes of the highest modes ranges from $\sim 10 \text{ \AA}$ to $\sim 50 \text{ \AA}$ (note that for $h = 0.087$, the low-frequency mode has its amplitude chopped at 25 \AA). This is in accord with the Ginzburg-Landau view of the film's motion, having a higher superfluid density and more superfluid motion as T falls and d increases. Also, even the largest amplitude motion is only about 5 nm, so this wave can appropriately be considered small compared to the thickness of these films, which are on the order of (at least) 100 nm thick.

The frequencies of the resonances uniformly grow as the temperature falls, which is the expected behavior since the frequency is proportional to the third sound speed which increases as the superfluid density rises for lower temperatures. Acquiring the amplitude

of surface motion at very low frequencies (viz. less than 0.2 Hz) is prohibitively time-consuming for our detection system, which may slightly distort the appearance of some low-frequency features of the spectra. However, as the film thickness rises and the temperatures fall, the resonant frequencies never exceed more than a few Hz. We will discuss in the next Chapter why this is the case.

These spectra do contain unexpected features. First, there seems to be a qualitative shift in the resonant modes halfway down the $h = 0.263$ spectra. The features below (at higher T) dominate the observed spectra of the thinner films, while the features above (at lower T) dominate the observed spectra of the thicker films. The reason for this shift is not completely understood; it appears to coincide with a temperature- and thickness-dependent change in the boundary condition for the standing waves. Second, we observe that the resonant peaks appear to mix with each other as a function of temperature. It is not clear what would cause the coupling between different eigenmodes of the surface motion. It could simply be an result of the above-mentioned shift in the boundary condition, but there are other ways of coupling the different standing wave modes. One candidate is the possibility of the film thickness varying over the substrate, $d = d(r, \theta)$. Another is the existence of the orbital angular momentum vector \mathbf{l} which points normal to the substrate for an A-like phase. The dynamics of superfluid ^3He are complicated enough to support the analog of the Hall effect, where the superfluid velocity moving radially couples through the \mathbf{l} vector (playing the role of the \mathbf{B} field in the Hall effect) to an azimuthal motion [Mermin and Muzikar, 1980] (though this particular effect does not seem large enough to account for the observed behavior). Finally, it is clear that the spectra is dominated by the damping in the system; the resonance-broadening effect of heavy damping could also cause mode-mixing effects.

Nevertheless, from these spectra it is clear that well-defined surface wave modes do exist in the superfluid ^3He film. Their amplitudes and frequencies behave qualitatively as we would expect for third sound waves, and the phenomena disappear for $T > T_c^{\text{film}}$. These spectra provide, to our knowledge, the first evidence for the existence of third sound in superfluid ^3He . In the next Chapter we will interpret these resonant modes and obtain values for the speed of third sound and the average superfluid density of the film, and the discuss the damping mechanisms for this wave motion.

Chapter 7. Analysis of Third Sound Resonance Spectra

In this Chapter we show that the observed spectra can be interpreted in terms of the Bessel modes. The boundary condition determining the wavevectors for these modes varies: for sufficiently thin films, or close to T_c^{film} , it is a 'free' boundary and for very thick or cold films it is a 'fixed' boundary. For a given thickness, the transition occurs over a small temperature range, which rises with increasing thickness. Using this understanding of the resonant modes, we determine the speed of third sound and the average superfluid density of the film as functions of temperature and film thickness. We then discuss the damping of these resonant modes.

A. Interpretation of third sound spectra as Bessel modes

Thick film resonance spectra. Let us first show that for very thick films at very cold temperatures, the resonance spectra are consistent with the 'fixed' boundary condition. As an example, let us consider a thick film ($h = 0.058$) for which we reached about $T/T_c^{\text{bulk}} = 0.34$. The spectra observed for this film is shown on the left in Figure 6.7e. As the temperature falls, there is a qualitative change in the appearance of the spectra which sets in near $T/T_c^{\text{bulk}} \sim 0.65$. The lowest-temperature spectrum is shown in Figure 7.1. The dashed line represents a six-peak Lorentzian fit to the spectrum, with the component Lorentzians shown as solid lines. The peak frequencies of these six Lorentzians are 0.89, 1.39, 1.80, 2.31, 3.04, and 3.70 Hz. As we described in Chapter 5, the frequencies of the resonant modes for a fixed boundary condition are given by

$$f_{mn} = (c_3/2\pi R) \alpha_{nm} \quad (7.1)$$

The peak frequencies obtained from the multi-Lorentzian fit are all within 8% of the frequencies given by equation (7.1), when we allow $m = 0$ and $m = 1$ modes and align f_{03} with the 3.04 Hz mode. In this regime the fixed boundary condition prevails.

In addition to the peak frequencies, the multi-peak Lorentzian also gives us the linewidths of the component modes, which are $\Delta f = 0.15, 0.27, 0.39, 0.30, 0.58,$ and 0.92 Hz respectively. Roughly speaking, these increase linearly with the resonant frequencies, so the Q's of these modes appear to be nearly frequency independent.

The amplitudes of the component modes behave qualitatively as we expected from our earlier discussion. The radial ($m = 0$) modes fall in amplitude as we go to higher frequency, as do the azimuthal ($m = 1$) modes; the relative strength of the radial and azimuthal modes depends on the symmetry-breaking in the experimental cell.

Thin film resonance spectra. Conversely, if we examine a spectrum from a thin film, the peaks closely align themselves with the β_{mn} Bessel zeros, indicating a free boundary condition. We will see this clearly in a moment, when we show mode-plots of the peak frequencies as a function of temperature.

Model of resonances. In Chapter 5 we presented a model using fixed boundary conditions which calculated the response of the film to the applied driving force. Figure 5.4 shows the spectra predicted by this model using the input values of $c_3 = 5$ cm/sec, $\beta = 1$ Hz, a tilt of $\alpha = 1$ mrad, and a fixed boundary condition. We can compare, for

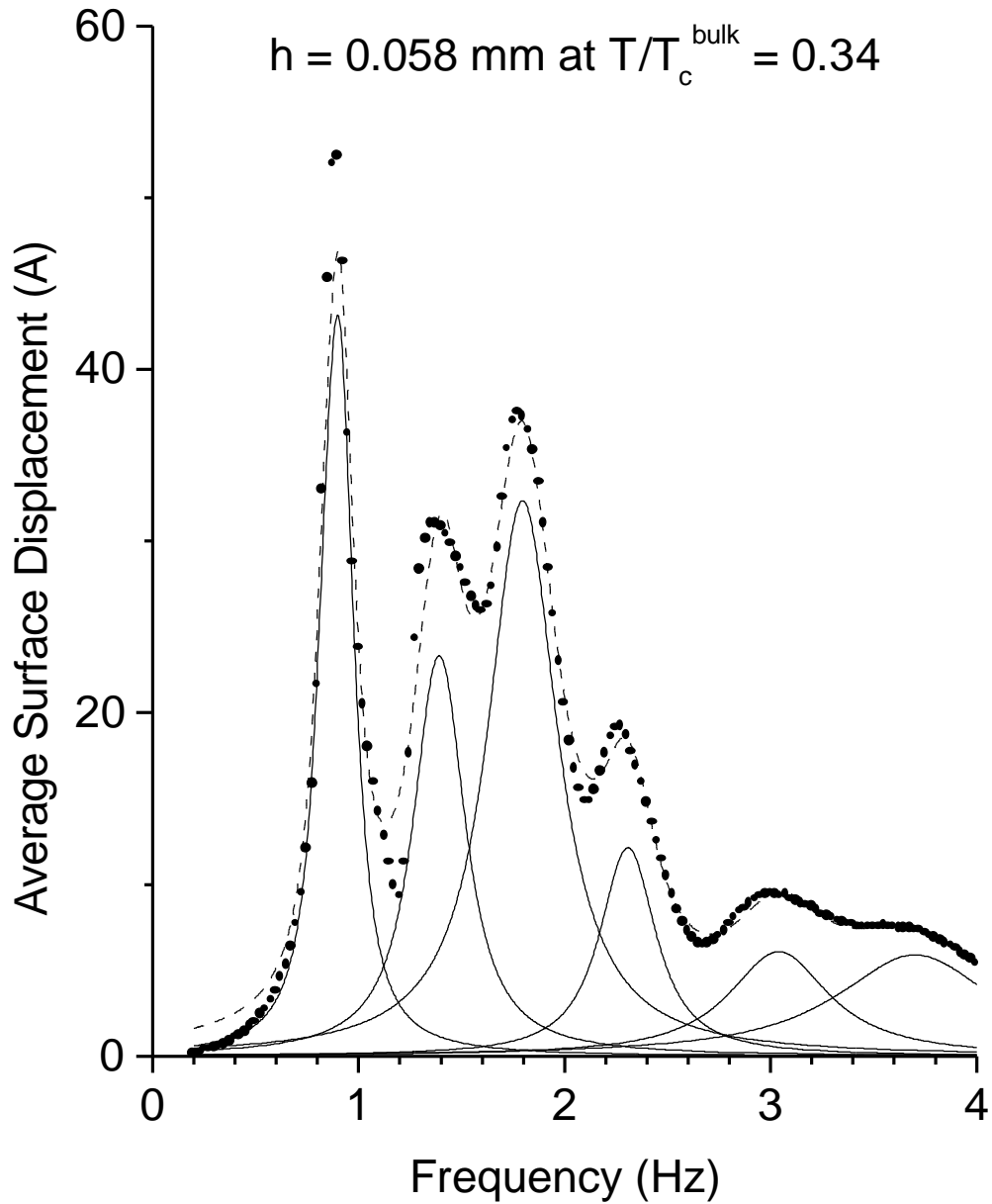


Figure 7.1 Multi-peak Lorentzian fit to a third sound spectrum. Third sound spectrum for $h = 0.058 \text{ mm}$ film at $T/T_c^{\text{bulk}} = 0.34$. The dashed line is a multi-peak Lorentzian fit to the spectrum, with the component Lorentzians shown in solid lines. The peak frequencies of these components match the α_{mn} Bessel zeros well, indicating a fixed boundary condition for the third sound standing wave.

example, this predicted result with the experimentally observed spectrum shown in Figure 7.1 for a film of height $h = 0.058$ mm at $T/T_c^{\text{bulk}} = 0.34$. While the result of the model does not agree precisely, there are marked similarities. Five peaks are clearly present in each spectrum, with the odd-numbered peaks falling in amplitude 1 to 3 to 5, and the even-numbered peaks falling in amplitude 2 to 4 but being smaller than peaks 3 and 5 respectively. In the model, the higher frequency modes are smaller than the lower frequency modes due both to higher efficiency driving and higher sensitivity detection; the difference between modes 1, 3, and 5 and modes 2 and 4 arises from poor coupling to the azimuthally asymmetric modes (modes 2 and 4 only exist in the model due to the plate tilt breaking the symmetry of the system). Further, the shape of the model spectra between modes 1 and 2, and the elevated amplitude between modes 2 and 3 are present in the observed spectra as well.

While this model is not able to quantitatively reproduce the observed spectra, it does aid us in two respects. First, the qualitative similarity between the model and the observed spectra gives us confidence that the observed resonant frequencies do indeed correspond to the particular modes we have identified for them; that is, the $m = 0$ and $m=1$ Bessel modes for a fixed boundary condition. Second, it gives us an estimate of the tilt angle, $\alpha \sim 1$ mrad, needed to observe resonances for non-azimuthally symmetric modes; this is a plausible figure, given procedure by which the plates were constructed. This gives us confidence that we really are detecting azimuthal modes of film motion.

Mode-plots: peak frequencies vs temperature. For a given film, the observed resonant modes exhibit a relatively complicated behavior as the temperature is varied. The Ginzburg-Landau theory says that the average superfluid density of the film should rise linearly in temperature below T_c^{film} (cf. equation (2.3))

$$\langle \rho_s \rangle / \rho = 1 - T/T_c^{\text{film}} \quad (7.2)$$

Since the temperature dependence of the third sound speed, and hence the resonant frequencies, comes only from the superfluid density, we expect that the frequencies should vary as the square root of $1-T/T_c^{\text{film}}$

$$f_{mn} = A_{mn} \sqrt{(1-T/T_c^{\text{film}})} \quad (7.3)$$

where A_{mn} is proportional to the Bessel zero of that particular mode. In fact it is not the case that the modes vary with precisely this temperature dependence;¹² nor do we use this function explicitly in determining any quantities from the spectra. Our purpose is to

¹² In fact, if we express the superfluid density fraction in terms of the temperature as

$$\langle \rho_s \rangle / \rho = (1 - T/T_c^{\text{film}})^p \quad (7.4)$$

then the exponent p which characterizes the temperature dependence varies from $p = 1$ (the Ginzburg-Landau value) to $p = 2$ (which results in a linear temperature dependence for the frequencies). The power law also depends sensitively on the value of T_c^{film} . These spectra do not determine the thermodynamic T_c^{film} precisely; we have observed superfluid film flow up to 0.1 mK above the temperature at which third sound became undetectable.

compare the ratios of the resonant frequencies in the spectra as T varies, for which it is sufficient that there is some function of temperature which is universal to all the observed modes within a spectrum. Once we have determined this function, we can construct a graph (for each film thickness) showing the observed resonant frequencies vs T , with a superimposed set of curves proportional to the Bessel zeros of either the free or fixed boundary condition. From this graph, or mode-plot, the form of the boundary condition (free or fixed) can be placed on firm footing, and the observed modes can be identified with particular eigenmodes with particular Bessel zeros. Once this is done, the speed of third sound can be determined as a function of temperature.

Two mode-plots are shown in Figure 7.2 for the thinnest film we studied ($h = 1.053$ mm). The lower graph shows a set of curves proportional to β_{mn} (consistent with a free boundary condition) for $m = 0$ and $m = 1$ which agree well with the observed peak frequencies. In contrast, no attempt to overlay a set of curves proportional to α_{mn} (consistent with a fixed boundary condition) will find such an agreement. A typical mismatch is shown in the upper graph. For the other thin films, shown in Figure 7.3, the agreement between the observed peak frequencies and the solid lines given by the free boundary β_{mn} Bessel zeros is good.

However, as the films get thicker, we reach a series of mode-plots (and spectra) which are not well-described by either a free or a fixed set of peak frequencies. Looking at the spectra in Figure 6.7, it is evident that the spectral structure seen in the thinnest films, which we identified with a free boundary condition, is gradually compressed into the high temperature section of the graph, while a new behavior emerges in the low temperature section. As we have discussed at the outset of this Chapter, the low temperature, thick film spectral features are consistent with the fixed boundary condition given by the α_{mn} Bessel zeros (cf. Figure 7.1).

We can see the transition from this free regime to fixed regime in the mode-plots of Figure 7.4 which are overlaid with solid lines corresponding to the fixed boundary condition. Near T_c^{film} , these solid lines do not match the observed peaks particularly well, but as the temperature falls, the peak frequencies tend towards the fixed boundary condition.

We now have firm identifications for the eigenmodes (meaning the α_{mn} or β_{mn}) of the observed resonances for the thinner films and the low temperature part of the thicker films. We extend the identification into the intermediate transition region, which introduces only a small error in the derived quantities. We obtain the wave speed c_3 , and then use c_3 and our determination of n from the $h(d)$ measurement to obtain the average superfluid density fraction of the film, ρ_s/ρ . Finally, we can discuss the observed damping of these resonances in terms of the various dissipative mechanisms available in superfluid ^3He .

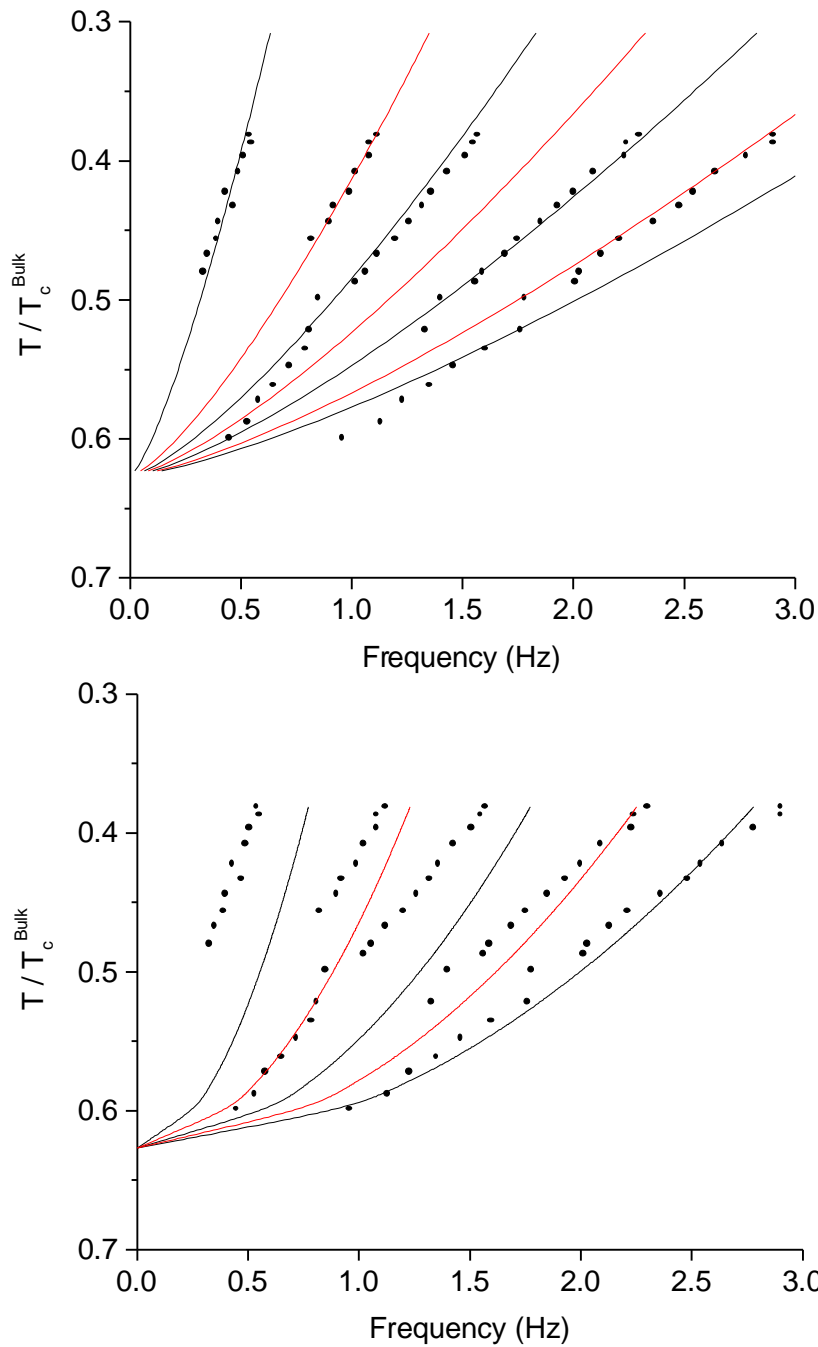


Figure 7.2 Mode-plots for the thinnest film. Mode-plots showing peak frequencies as a function of temperature. The solid lines on the upper graph display the good match between the peak frequencies and the β_{mn} Bessel zeros of a free boundary condition. The lower graph shows a failure to achieve a good match with a fixed boundary condition and the α_{mn} Bessel zeros.

B. Calculation of third sound speed from spectra

Based on our identification of the observed resonances as the $m = 0$ and $m = 1$ Bessel modes for an appropriately identified boundary condition, we can calculate the third sound speed as a function of the temperature and height h . We will use the highest frequency mode in each graph of Figures 7.2-7.4 as a benchmark. This choice has several virtues. First, the peak is identifiable over nearly the entire temperature range spanned by the experiment for any film thickness. Second, as the film thickness changes, this peak is always present and clearly identifiable. Third, it is apparently immune to the splitting and mixing which affects the lower frequency modes. For the thinner films, this mode falls on the solid line identified with the β_{13} Bessel zero mode; for thicker films it is identified with the α_{03} Bessel zero.

We measure the frequencies of the peaks of the benchmark mode as a function of temperature, and then determine the speed c_3 by using equations (5.9-11). The result is shown in Figure 7.5.

The resulting speed of third sound, c_3 , is slightly different than that given in [Schechter *et al.* 1998b] where it was assumed that the benchmark was the α_{03} mode for all films; the speed is reduced by a factor of $\alpha_{03}/\beta_{13} = 0.851$ for all films with h greater than 0.117 mm. This has only a slight qualitative effect on the data. For films which show the transition between the two boundary condition regimes, there is a small systematic error in the transition region which is on the order of about 10%.

The speed of third sound varies from 0 to 5 cm/sec, which is the range we expect from prior measurements of the average superfluid density for ^3He films and of the van der Waals restoring force. For each film thickness, the speed of third sound increases monotonically as T decreases. This is what we expect, since the superfluid density increases monotonically as the film cools, and this causes the wave speed to increase. The dependence of c_3 on the film thickness d , or film height h , is more complicated. (Thickness increases from solid to hollow points.) At $T/T_c^{\text{bulk}} = 0.6$, the speed increases rapidly as h decreases for thin films, then stalls after reaching $h = 0.394$ mm. This behavior is the result of two competing influences on the third sound speed c_3 as the film thickness is increased. The first is the van der Waals force: the greater distance from the film's surface to the substrate causes the van der Waals restoring force to fall, tending to reduce c_3 . The second is the suppression of superfluidity near the substrate: the superfluid density is strongly suppressed for the part of the film within $\xi(T)$ of the substrate. As d becomes larger than $\xi(T)$, a smaller fraction of the film is subjected to this effect, so the average superfluid density rises, tending to increase c_3 . In the range of thicknesses we studied, the speed tends to be fairly immune to changes in film thickness.

C. Calculation of superfluid density fraction

We can obtain the average superfluid of the film by inverting equation (6.7) to obtain

$$\rho_s/\rho = c_3^2/ngh \quad (7.5)$$

where we have calculated c_3 in the previous section, measured $h = H_{\text{filling}} - H$ for each

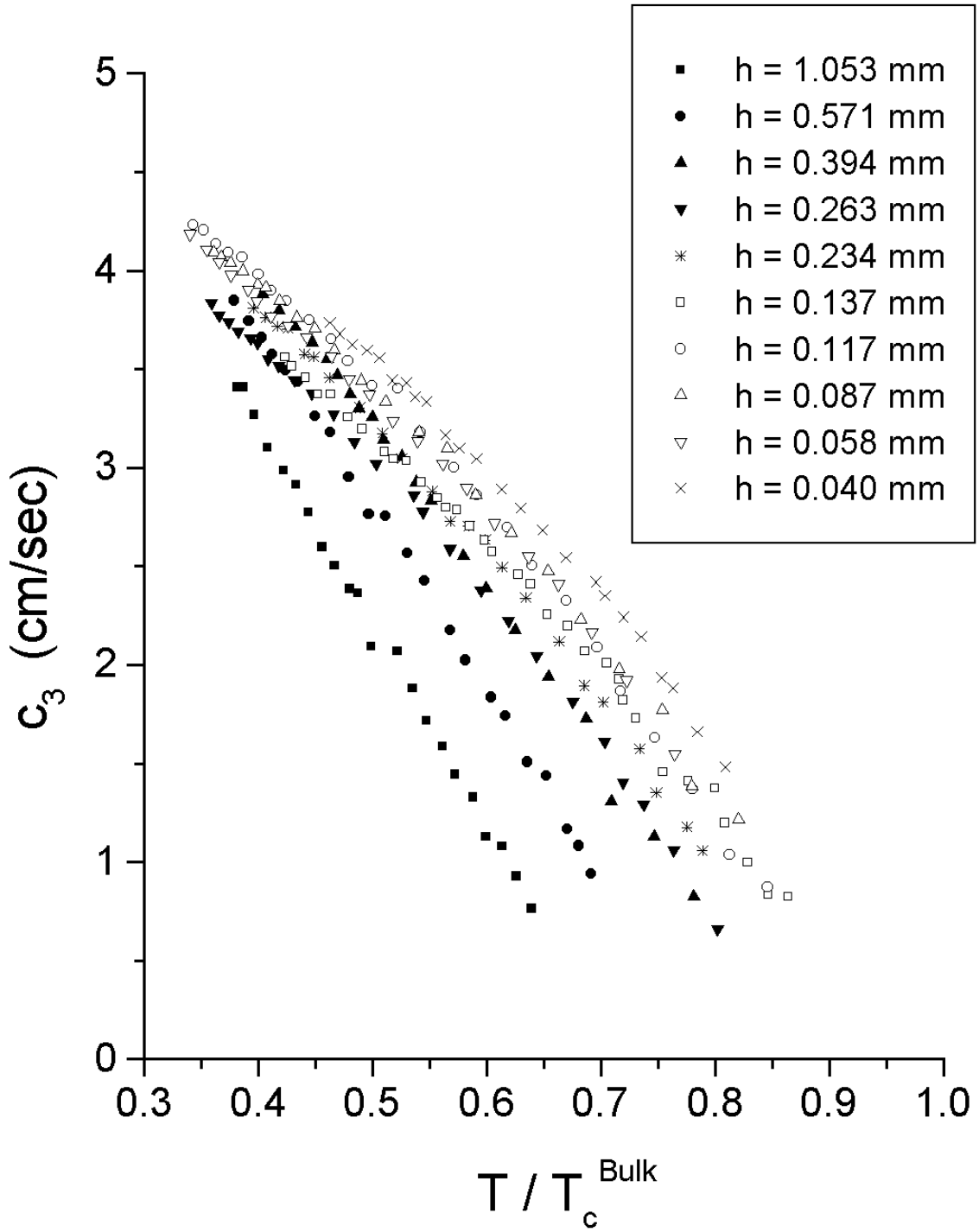


Figure 7.5 The speed of third sound. Calculated from the third sound spectra as described in the text.

film using the capacitive level detector, and used $n = 3.44$ obtained from the experiment in which $h(d)$ is measured continuously. The average superfluid density obtained is shown in Figure 7.6a as a function of the temperature and film thickness.

This graph accords qualitatively with our expectations in several important respects. First, as the temperature falls, the average superfluid density rises for all temperatures. Second, as the films get thicker, the average superfluid density rises. Third, as the films gets thicker, the critical temperature for the onset of superfluidity rises.

However, quantitatively these superfluid densities fail to agree with our expectations, particularly for the thickest films where they equal or exceed the bulk superfluid density and even exceed 1.0 (for the thickest film). The explanation for this inconsistency probably comes from the determination of $h = H_{\text{filling}} - H$. As we discussed in the previous Chapter, if the substrate is slanted with respect to gravity our measured values of h would be too low by a constant which is probably on the order of $\sim 30 \mu\text{m}$. If we recalculate the average superfluid density using $h' = h + 30 \mu\text{m}$, (adjusting the exponent obtained in Chapter 6 to $n = 3.26$), then we obtain the graph in Figure 7.6b. This offset dramatically affects the calculated superfluid densities of the thickest films, but has only a relatively small effect on the thinner films (where the offset is a small fraction of h). In the following section on dissipation, we will use the values for the superfluid density arrived at with h' and $n = 3.26$, since they are more physically reasonable.

We can compare the average superfluid density curves calculated here with the predictions of the Ginzburg-Landau theory, given by equation (2.35). (Equation (2.34) agrees with equation (2.35) very well down to at least $T/T_c^{\text{bulk}} = 0.4$, for film thicknesses less than $5 \xi_T(T)$.) Figure 7.7 shows the superfluid densities determined with the $30 \mu\text{m}$ offset and the Ginzburg-Landau curves for films with thicknesses in multiples of $\xi_T(0) = 50.3 \text{ nm}$, from 100.6 nm to 402.4 nm . (Here we are not comparing a particular value of h with a particular theoretical film thickness, just comparing the overall shapes of the functions.) The superfluid density curve of the thinnest films we studied do not follow the form of the Ginzburg-Landau prediction: for a given intercept T_c^{film} , the slope of the observed data is smaller than the theory would have it. For our thicker films, the data matches the Ginzburg-Landau curves more closely.

Interestingly, when a given theoretical curve matches an observed set of superfluid densities at high temperatures, it will tend to over-estimate them at lower temperatures, an effect which was also observed by Freeman [Freeman 1988].

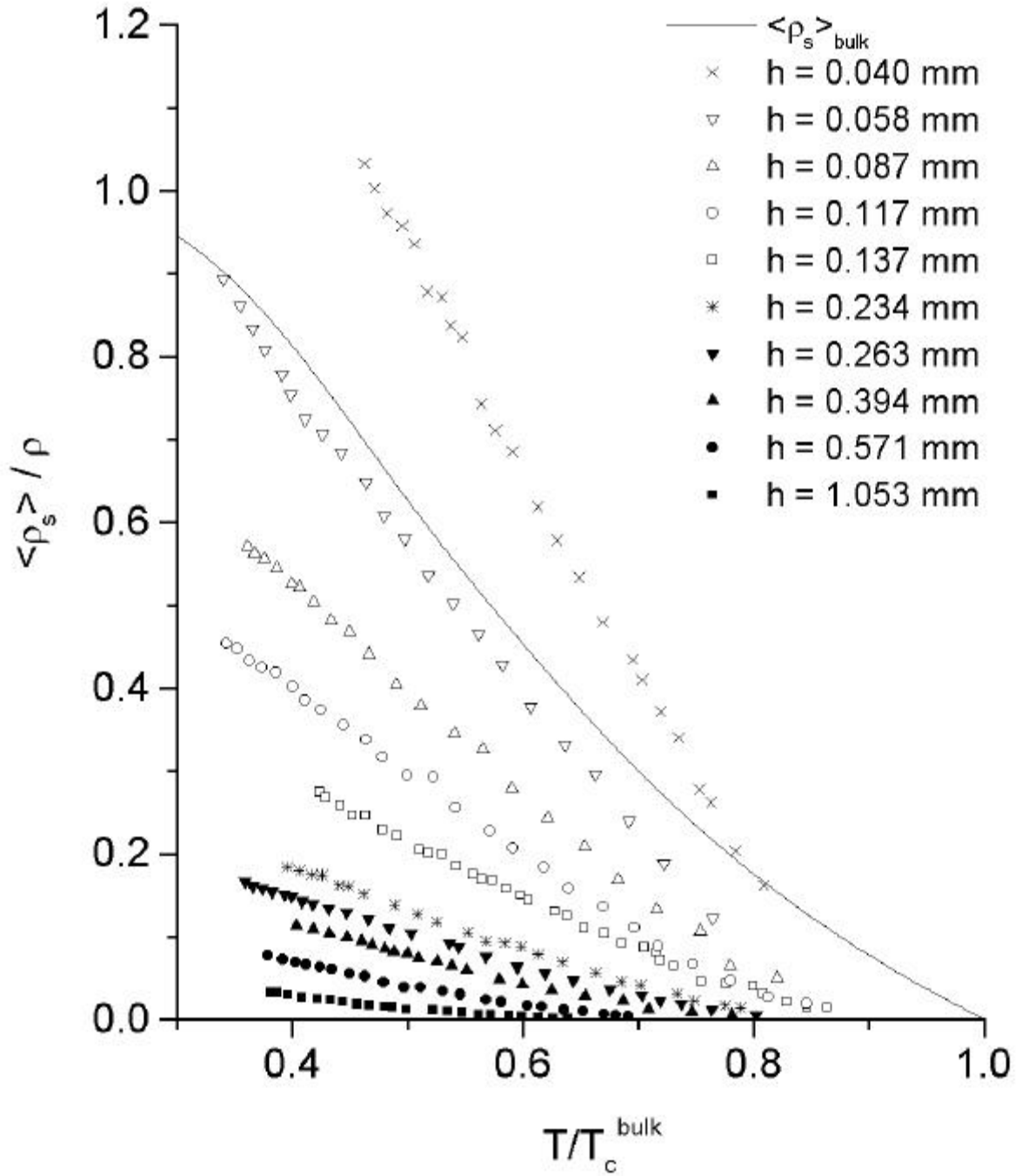


Figure 7.6a The superfluid density calculated using $h = H_{\text{filling}} - H$. The result is quantitatively unphysical for the thickest films.

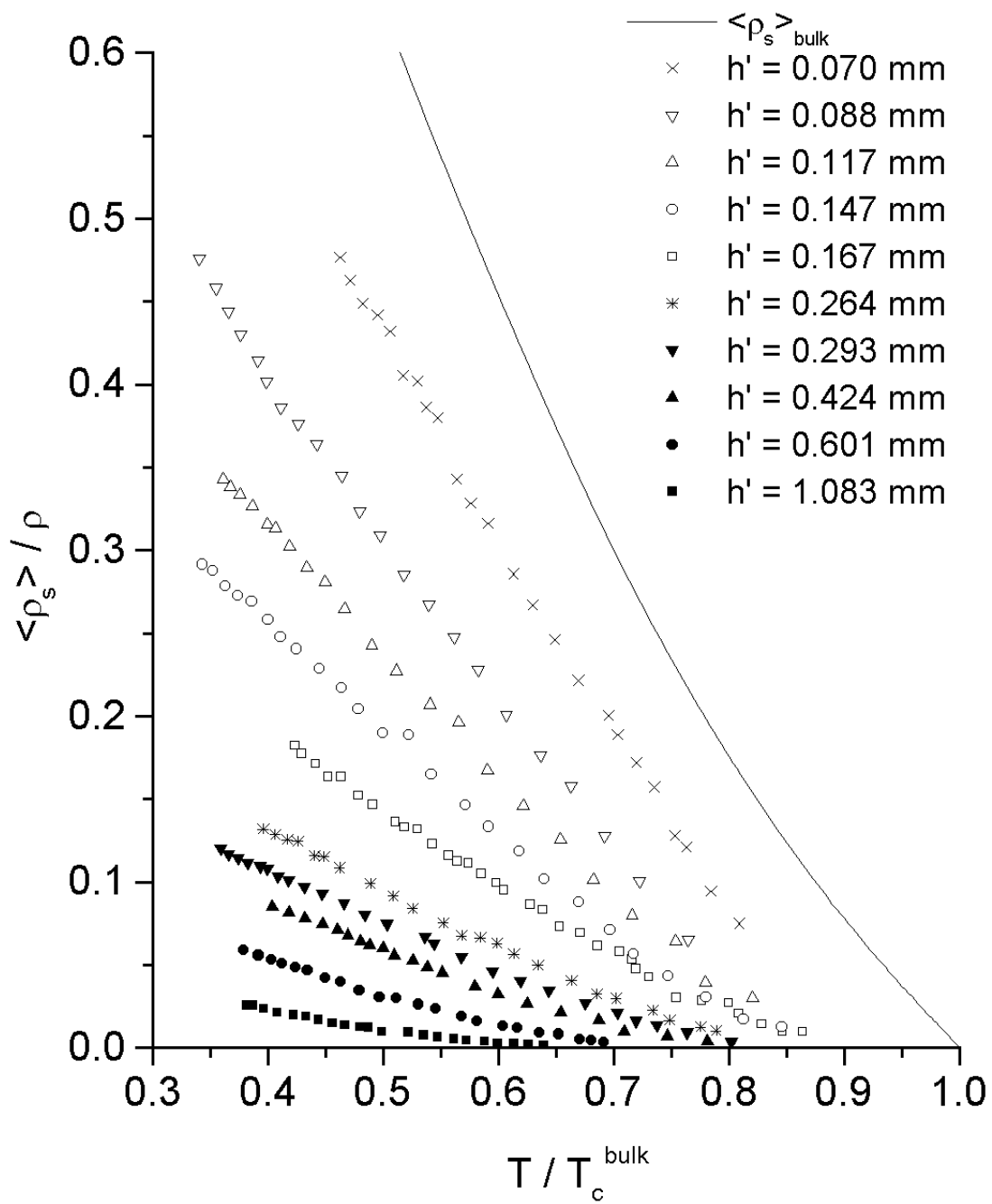


Figure 7.6b The superfluid density calculated using $h' = h + 30 \mu\text{m}$.

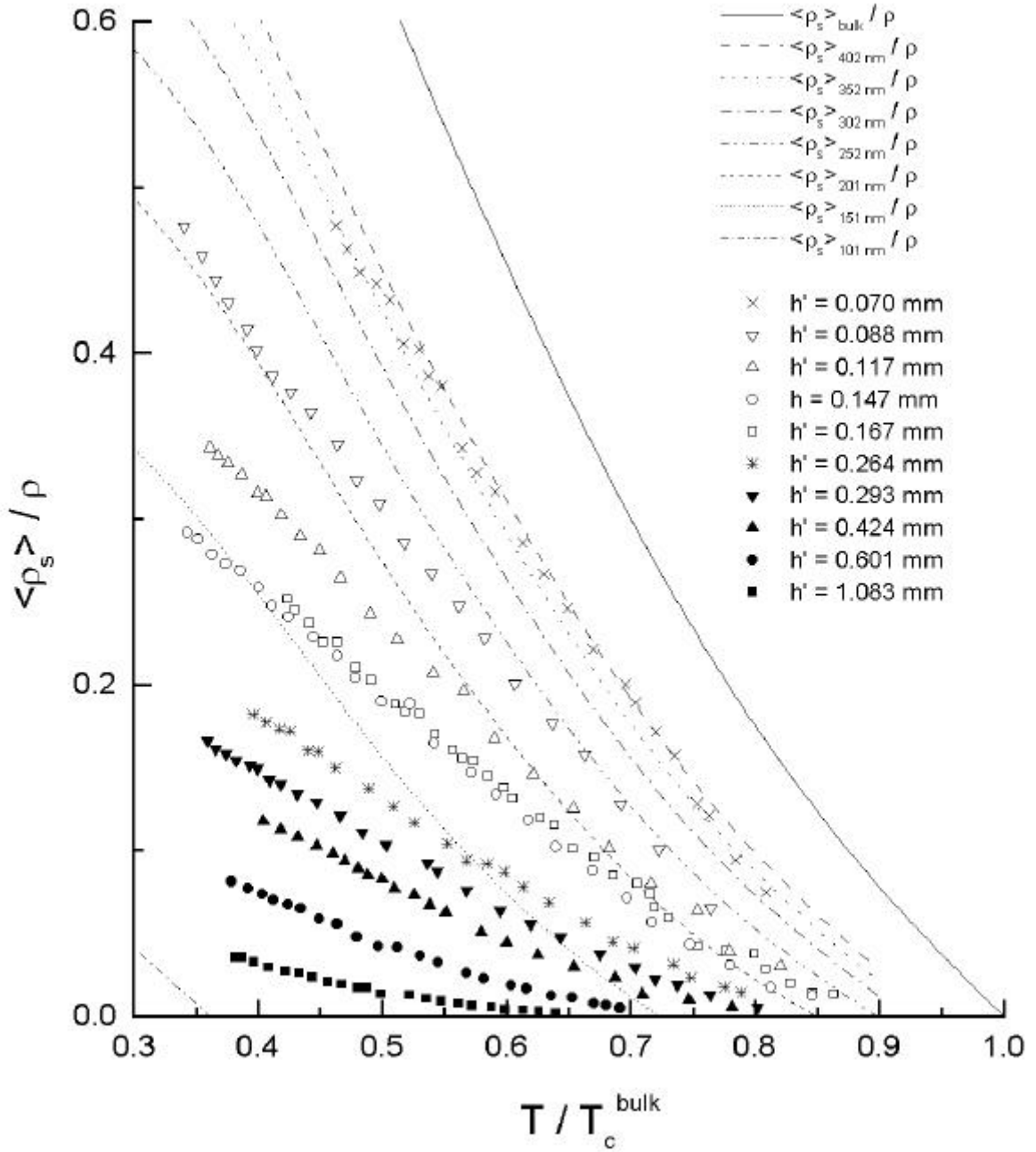


Figure 7.7 Superfluid density and G-L curves. Superfluid density from Figure 7.6b compared with the Ginzburg-Landau theory. This is not meant to be taken as a quantitative comparison, due to the uncertainty on the experimental film thicknesses.

D. Damping of third sound resonances

The resonant spectra of third sound standing waves which we have observed in ^3He is dominated by very strong dissipation, compared to the spectra of ^4He at low temperatures. We will discuss the damping using the most easily characterized mode as an example. In Figure 7.8 we show the linewidths Δf of the mode in thick, cold films which is identified with the α_{01} Bessel zero, as a function of temperature.

We can analyze these linewidths in terms of the quality factor $Q \equiv f/\Delta f$, shown in Figure 7.9 as a function of temperature. The Q 's increase monotonically as the temperature falls, but there is very little variation in the quality factor as a function of the film thickness, despite the height changing from $h = 0.137$ mm to $h = 0.040$ mm. We will consider several different intrinsic mechanisms of dissipation and see if one of them could be responsible for the observed quality factors of these modes: orbital viscosity, thermal currents out of the film, second viscosity, and thermal gradients within the film. Finally, we will consider the damping due to transmission/reflection losses over the boundary at the edge of the substrate.

One difficulty which unfortunately prevents us from reaching firm conclusions about the dissipation is a lack of experimental data on thermodynamic quantities for the ^3He film. It is believed to be in an A-like phase, but at zero pressure. Since the ^3He -A phase does not exist at zero pressure for bulk liquid and the thermodynamic properties involving dissipation tend to be pressure-dependent, we have so far only been able to calculate the theoretical dissipation in an order-of-magnitude manner.

Dissipation from orbital viscosity. As we have discussed, in the ^3He -A phase the superfluid possesses a well-defined orbital angular momentum vector \mathbf{l} . The \mathbf{l} vector points in the direction of the node in the energy gap between the Cooper pair states and the excited quasiparticle states. Any motion of the \mathbf{l} vector forces the normal-fluid quasiparticles in \mathbf{k} -states near this gap to be out of equilibrium; the relaxation process to restore equilibrium produces a viscous torque on the \mathbf{l} vector. The power per volume dissipated by this mechanism is

$$P = \mu (d\mathbf{l}/dt)^2 \quad (7.6)$$

where \mathbf{l} is the unit vector along the angular momentum vector, and μ is the coefficient of orbital viscosity given near T_c by

$$\mu = (\pi^2/128) \tau_N(T_c) N_F (k_B T_c) (\Delta_0(T)/k_B T_c)^2 \quad (7.7)$$

with $\tau_N(T) = 0.82 \mu\text{s} (\text{mK})^2 / T^2$ at zero pressure [Cook *et al.* 1996] is the quasiparticle lifetime, $N_F = m^* k_F / (\hbar/2)^2 = 9.1 \times 10^{50} \text{ J}^{-1} \text{ m}^{-3}$ is the density of states at the Fermi surface for spins of one type, and $\Delta_0(T) = 3.42 k_B T_c (1-T/T_c)^{1/2}$ is the maximum of the energy gap near T_c for the A-phase [Vollhardt and Wolfle 1990]. For more on orbital viscosity, see [Vollhardt and Wolfle 1990 p.482-484] and [Lee and Richardson 1978, p. 442-448].

What is the motion of the \mathbf{l} vector during a third sound wave? There are two cases to consider: the \mathbf{l} vector moves at the frequency of the third sound wave, or the \mathbf{l} vector moves at a higher frequency.

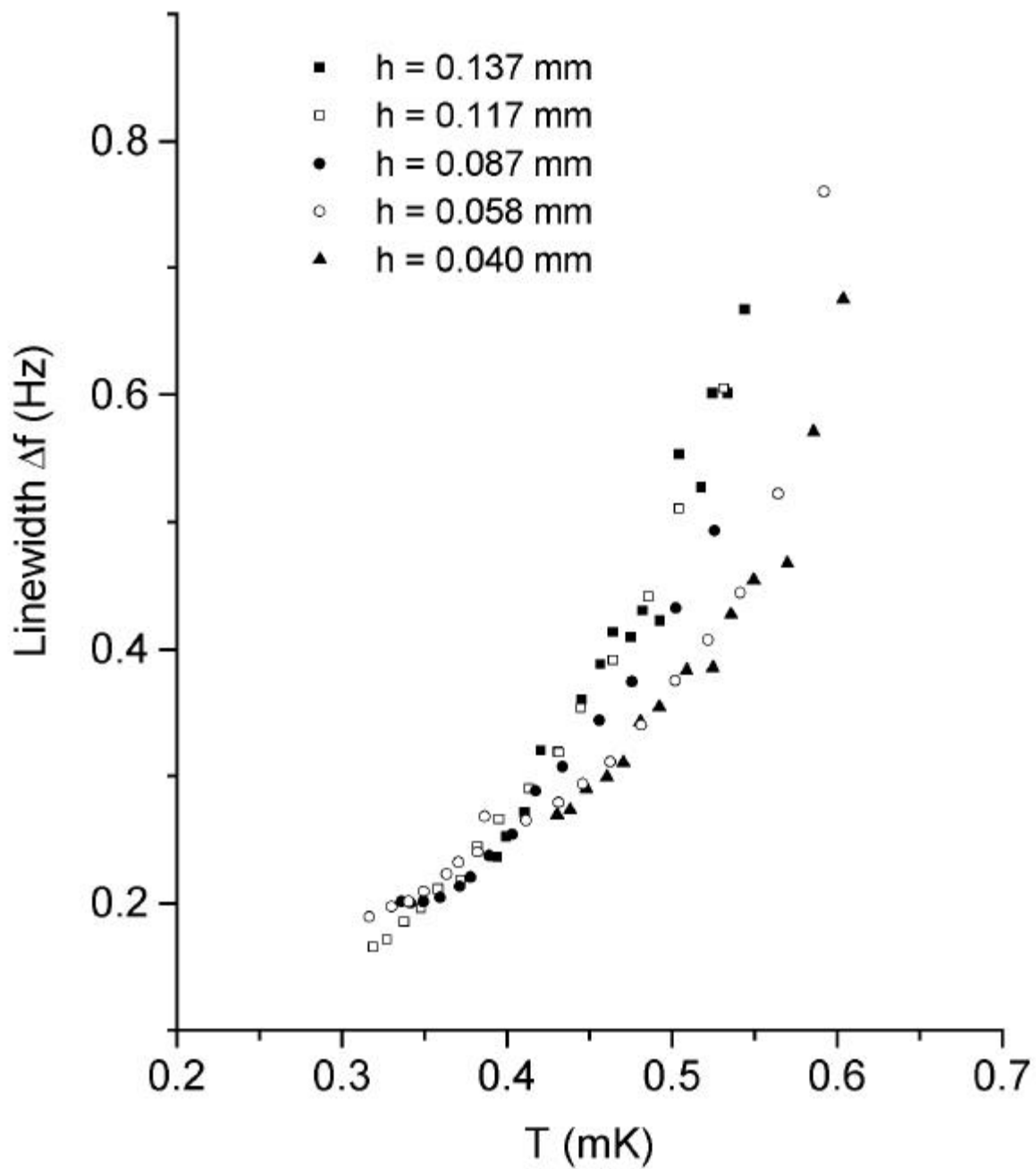


Figure 7.8 Linewidths Δf of the α_{01} mode as a function of temperature.

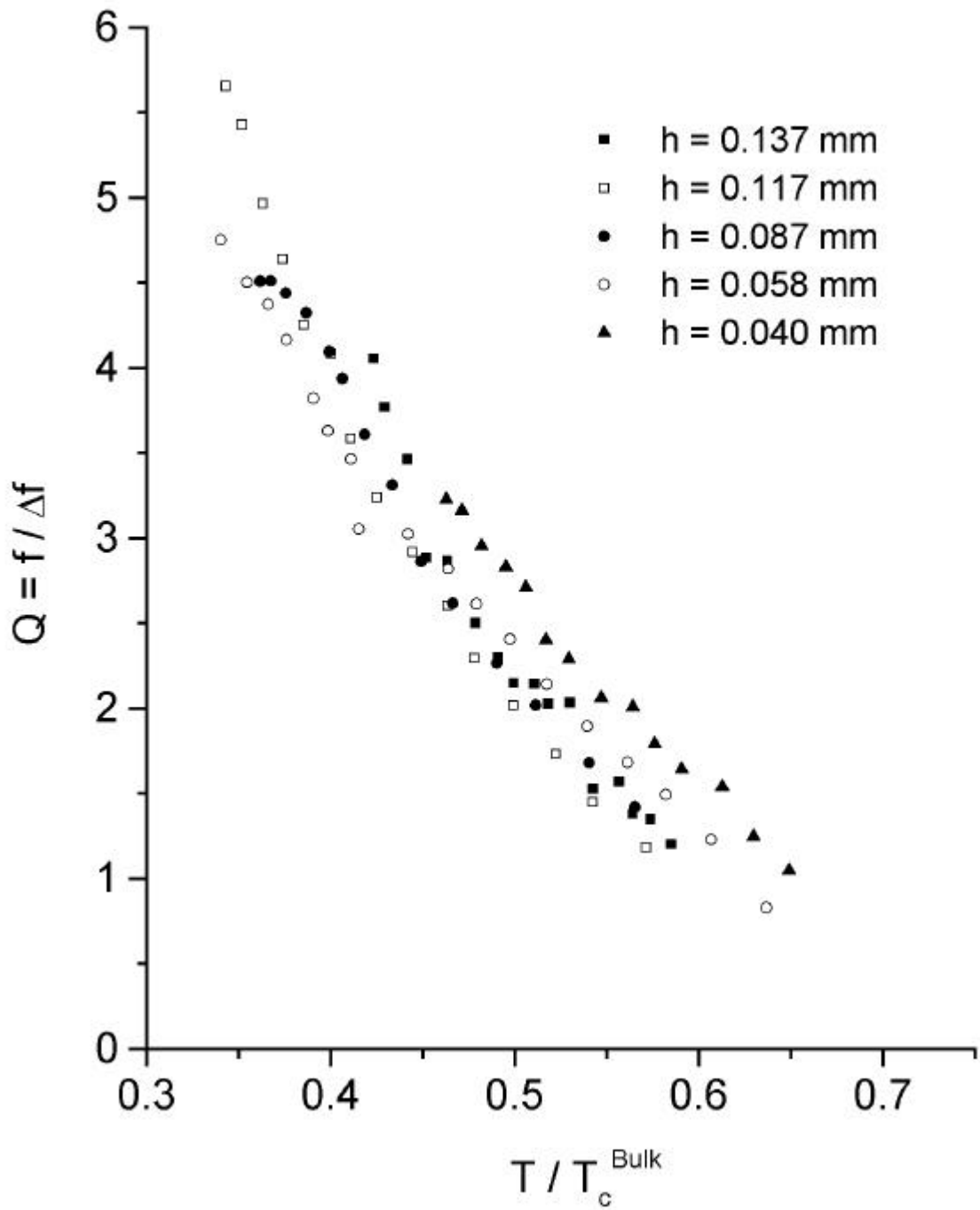


Figure 7.9 Quality factors Q of the α_{01} mode as a function of temperature.

In the first case, the maximum possible dissipation (and minimum Q) will occur when $(d\mathbf{l}/dt)^2 = \omega^2$. (Small oscillations of \mathbf{l} around some fixed axis reduce $(d\mathbf{l}/dt)^2$ by a factor of $\sin^2 x$, where x is the angle between \mathbf{l} and the fixed axis. Since large motions of \mathbf{l} , completely reversing direction during a half-cycle of third sound, violate the desire of the \mathbf{l} vector to remain normal to the substrate, this maximum should be a considerable over-estimate of dissipation due to this mechanism.) The Q is equal to the stored energy in the oscillation divided by the energy lost per radian. The stored energy $2.45 \rho a_{vdw} A^2/k^2$ where A is the amplitude of the standing wave, k is the wavevector, and the 2.45 comes from integrating the Bessel function over the substrate. The energy lost per radian is $\mu\omega^2\pi R^2 d/\omega$, where R is the radius of the substrate and d is the thickness of the film. The quality factor is therefore

$$Q = \rho a_{vdw} A^2 / \pi R^2 d \alpha_{01}^2 \omega \mu \sim 300 (1-T/T_c)^{-3/2} \quad (7.8)$$

which is too large to be the source of the dissipation we observe (not even considering that this is almost certainly an over-estimate). This shows that orbital viscosity at the third sound frequency is not the cause of the damping we observe.

However, we need to consider the second case, where the frequency of the \mathbf{l} vector's motion is much larger than the third sound frequency. For instance, it is possible that the frequency of the \mathbf{l} vector motion would be governed by the size of the chemical potential gradients, for instance, like the Josephson frequency. This would lead to a larger power dissipation from orbital viscosity. Whether this actually occurs must be determined by analyzing the complete equations of motion for the ^3He film to determine the motion (if any) of the \mathbf{l} vector.

Dissipation from dissipative terms in our third sound equations. The other forms of dissipation which we are considering arise directly from the equations of motion which we wrote down in Chapter 5. Following the analysis of Brouwer [Brouwer *et al.* 1995], the complex third sound speed $u_3 = \omega/k$ can be written

$$u_3^2 = c_3^2 + i [\rho_s \zeta_3 \omega + (\rho_s/\rho^2)(s^2 T \kappa / c^2 c_3^2) \omega + (\rho_s/\rho^2 \omega d)(sT/c)^2 \partial J_{out}/\partial T] \quad (7.9)$$

where the speed c_3 is given by

$$c_3^2 = (\rho_s/\rho) [a_{vdw} d + s^2 T/c]. \quad (7.10)$$

Here s is the entropy per unit mass, c is the heat capacity per unit mass, κ is the thermal conductivity of the film, and J_{out} is the entropy current out of the film. For these ^3He films, particularly at low temperatures, the second term in equation (7.9) is negligible. The damping given by

$$Q = [-2c_3 \text{Im}(u_3^{-1})]^{-1} \approx c_3^2 / \text{Im}(u_3^2) \quad (7.11)$$

This complicated expression can be simplified if we consider the three terms in $\text{Im}(u_3^2)$ separately, assuming each in turn is dominant over the others.

Thermal current out of the film. If this were the dominant term, the quality factor would go as

$$Q = c_3^2 \omega d [(\rho_s/\rho^2)(sT/c)^2 \partial J_{\text{out}}/\partial T]^{-1} \quad (7.12)$$

$J_{\text{out}} \equiv J_{\text{thermal}}/T$ is the thermal current out of the film into the substrate at any point, divided by the equilibrium temperature of the film. So, $\partial J_{\text{out}}/\partial T = 1/TR_K$ where R_K is the thermal (boundary) Kapitza resistance between the film and the substrate. R_K is not known to us for the interface between bulk copper and a ^3He film at sub-mK temperatures; however, it is probably larger than the measured value of $R_k = 160 \text{ K}^2\text{W}^{-1} \cdot \text{T}^{-1}$ per unit area found for ^3He on a sintered copper powder [Harrison 1979]. Also, the heat capacity for a superfluid ^3He film, A-like but at $P = 0$, is not known. However, at low temperature in an A-like phase, we can expect the heat capacity to fall as $c = \gamma T^3$, so we can expect the entropy to fall as $s = (\gamma/3)T^3$, making $(s/c)^2 \sim 1/9$. Using these values, the calculated quality factor for the films of Figure 7.8 and 7.9 comes out about 1000 times larger than the observed Q's. Hence, we believe that the Kapitza resistance between copper and ^3He large enough that we can exclude the thermal current into the substrate as a primary component of dissipation.

Second viscosity. The quality factor for the case where second viscosity is the dominant form of damping is

$$Q = c_3^2 / \omega \rho_s \xi_3 \quad (7.13)$$

Here ξ_3 is a coefficient of second viscosity. In $^3\text{He-B}$, for a range of pressures, it has been measured by Hook [Hook *et al.* 1994] from the damping in the motion of a membrane within a bath of superfluid ^3He , finding good agreement with theory. Using this $^3\text{He-B}$ data for ξ_3 , we obtain the curve shown in Figure 7.10, overlaid on the measured values of Q. It is within an order-of-magnitude (though it would actually predict more dissipation than we in fact observe). However, the temperature dependence of the second viscosity coefficient in $^3\text{He-A}$ is expected to have a different temperature dependence than in $^3\text{He-B}$, varying as T^{-2} [Vollhardt and Wolfle 1990]. This leads to the opposite temperature dependence from that which we observe; the Q's would fall as T falls. Based on this, we believe we can exclude second viscosity as a candidate for the primary form of dissipation.

Thermal gradients within the film. If this were the dominant term, the quality factor would go as

$$Q = (c_3^4/\omega) [(\rho_s/\rho^2)(s^2T\kappa/c^2)]^{-1} \quad (7.14)$$

In the $^3\text{He-A}$ phase, the thermal conductivity perpendicular to the \mathbf{l} vector (therefore parallel to the substrate) varies linearly in temperature, $\kappa(T) \sim (T/T_c) \kappa_N(T_c)$ [Vollhardt and Wolfle 1990, p. 482], where $\kappa_N(T_c) \sim 3.8 \text{ mW/K}\cdot\text{m}$ [Wheatley 1975]. Again we can make the argument that the ratio of the entropy to the heat capacity (both per unit mass) should be about $(s/c)^2 \sim 1/9$. This rough calculation obtains a Q several hundred times larger than the observed Q's, but with approximately the same temperature dependence as the observed Q's. Given the uncertainty in the thermodynamic parameters that went into this calculation, thermal gradients remain a candidate to contribute to the third sound dissipation.

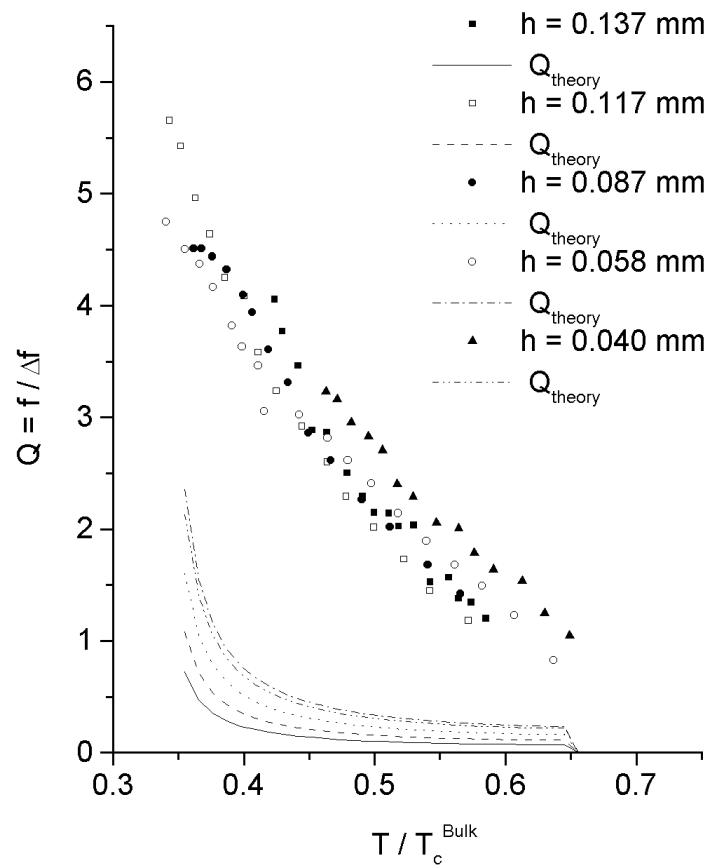


Figure 7.10 Data and 'calculation' of second viscosity damping. The mismatch between the observed quality factors and those calculated for second viscosity-damping using ${}^3\text{He-B}$ data for $\xi_3(T)$.

Transmission/reflection losses at the boundary. A non-intrinsic damping mechanism for the wave is the loss of energy due to transmission of the wave through the boundary at the edge of the film. In this picture, the standing wave on the substrate is viewed as a superposition of out-going waves and reflected in-going waves, which couple to a waves on the other side of the boundary. The loss can be expressed in terms of the reflection coefficient R (ranging from 1 for a free boundary condition to -1 for a fixed boundary condition). In simple one-dimensional models of this problem, the Q for the standing wave resonance created by the reflection can be shown to vary as

$$Q \sim (1+R^2)/(1+R)^2 \quad (7.15)$$

We saw that for our thicker films, there is a transition from a free boundary condition at high temperatures to a fixed boundary condition at low temperatures. Also, the high-Q modes appeared only in the low-temperature limit. These observations match the behavior predicted by equation (7.15): Q increases continuously as R changes from +1 (the free boundary) to -1 (the fixed boundary). In addition, in some of these models the Q depends on the superfluid density as well, rising as the temperature falls. The mechanism by which the reflection coefficient at the edge changes as a function of the temperature is not yet understood; a good model of this behavior would likely explain the observed Q's quantitatively, given the weakness of the intrinsic dissipation mechanisms discussed above. Developing a model to understand the changing boundary condition is a goal of future work.

Chapter 8. Future Directions for Third Sound Research

The existence of third sound in ^3He provides several exciting opportunities to explore new physics in unconventional, 2-dimensional superfluidity. This is an area of much research activity recently due to the belief that the superconductivity in high- T_c cuprates originates in a single 2-dimensional CuO_2 layer. Third sound could be used as a probe of several important phenomena for which no probe was previously available, for instance the generation and decay of 2-D quantized vortices in very thin films. In this last section, we will comment on our first efforts to use ^4He coating of the substrate to enhance the superfluidity of thinner ^3He films, and then describe an experiment which could be done to study 2-D quantized vortices in ^3He films using third sound resonances.

A. Enhance ^3He superfluidity with a ^4He coating of the substrate

As we have discussed, on a diffusively scattering surface the superfluid order parameter for ^3He vanishes at the substrate (or at least the relevant transverse components of the order parameter). Thus, the superfluid density of the film is suppressed within $\xi(T)$ of the substrate. Hence, for films with $d < 100$ nm, the superfluidity is almost completely quenched by the presence of the diffusive surface and T_c^{film} is reduced greatly from T_c^{bulk} . These two effects profoundly hinder our ability to probe very thin (truly 2-dimensional) superfluid films of ^3He . However, as we have also discussed, coating the substrate with a few monolayers of ^4He has been observed to modify the specularly of the surface and enhance the ^3He superfluidity. This was first observed by Freeman in his work using a torsional oscillator loaded with 280 nm slabs of ^3He between Mylar sheets [Freeman *et al.* 1988]. The effect was confirmed by [Harrison *et al.* 1991] in their work on film flow from a self-emptying beaker. Since then, it has been observed repeatedly by a variety of groups [Tholen and Parpia 1991, 1992], [Jiang and Kojima 1992], and [Kim *et al.* 1993].

With this in mind, we added a small amount of ^4He to the cell when it contained a film with $d \sim 150$ nm, sufficient to cover the substrate to a depth of about 2.5 monolayers. This estimate of the ^4He surface coverage is based on the following assumptions. First, we used the density of ^4He monolayers given by Freeman [Freeman 1988] as $18 \mu\text{mole}/\text{m}^2$ for the first layer and $13 \mu\text{moles}/\text{m}^2$ for additional layers. Second, we assumed that the ^4He coated the surfaces in the cell evenly, and that the total surface area inside the cell was given by $140 \pm 3 \text{ m}^2$ given by the BET test. (This assumption requires that the adsorption onto the silver-sinter heat exchangers which dominate the cell's surface area is the same as onto the copper substrate.)

The addition of the ^4He had a large effect on the observed spectra of third sound responses, as illustrated in Figure 8.1. For a given temperature and film thickness, the speed of third sound is dramatically increased. Also, the temperature T_c^{film} at which the film begins to show superfluid motion rose considerably with the addition. These observations are consistent with an increase in the average superfluid density of the film, as shown in Figure 8.2. For a pure ^3He film of this thickness, there is no observable superfluid motion above $T/T_c^{\text{bulk}} = 0.653$; with the addition of the ^4He , this rises to $T/T_c^{\text{bulk}} = 0.876$.

We repeated the experiment for a thinner film, about $d \sim 131$ nm, with the results shown in Figure 8.3, which compares two film thicknesses each with the same ^4He coating. T_c^{film} for the thinner film is reduced from that of the thicker film, as is the third sound speed and the average superfluid density at a given temperature. (The spectra show qualitatively the same features, otherwise.) This is unfortunate, since it implies (for this coverage of ^4He) that going to even thinner films will see a further suppression of T_c^{film} , to the point where it would become impossible to do the experiment. The situation is made clear in the graph in Figure 8.4, which shows the suppression of T_c^{film} as a function of film thickness both with and without the ^4He coating. Without the coating, the measured values of T_c^{film} follow the curve given by the Ginzburg-Landau theory (it is also essentially the same as that of Kjaldman, Kurkijarvi, and Rainer in this thickness regime). The values of T_c^{film} , according to the theory curve, plummet near 150 nm; we were not able to observe third sound responses in any films of pure ^3He thinner than shown on this graph, consistent with the theory. However, with the coating, we were able to observe superfluid third sound responses in a film of thickness $d \sim 131$ nm, where no pure ^3He response was seen. T_c^{film} with the coating is falling as we go to thinner films, but it is not clear from this data how fast it will leave the experimentally accessible region. It is hopeful to note that we were perhaps not using the optimal surface coverage of ^4He in these measurements; the suppression of T_c^{film} in other experiments [Kim *et al.* 1993] was strongly dependent on the thickness of the ^4He layer.

One unfortunate effect of the ^4He coating is to increase dramatically the base temperature to which the ^3He can be cooled, which can be seen in the spectra of Figures 8.1 and 8.3. The ^4He is believed to increase the thermal Kapitza resistance between the silver-sinter heat exchangers and the ^3He in the cell, thus stopping the ^3He from being cooled to very low temperatures. The results we have obtained by coating the substrate with ^4He so far are promising, but to continue the present effort with a reasonable hope of success will require the construction of a better, larger heat exchanger than the one presently being used, in order to counter this effect. An alternative route which could be more profitable would be to go directly to experiments on unsaturated, very thin films of superfluid ^3He with a ^4He coating; a cell using the present nuclear stage heat exchanger could be constructed which would evade this problem as much as possible by having a sealed inner experimental cell surrounded by a bath of pure ^3He .

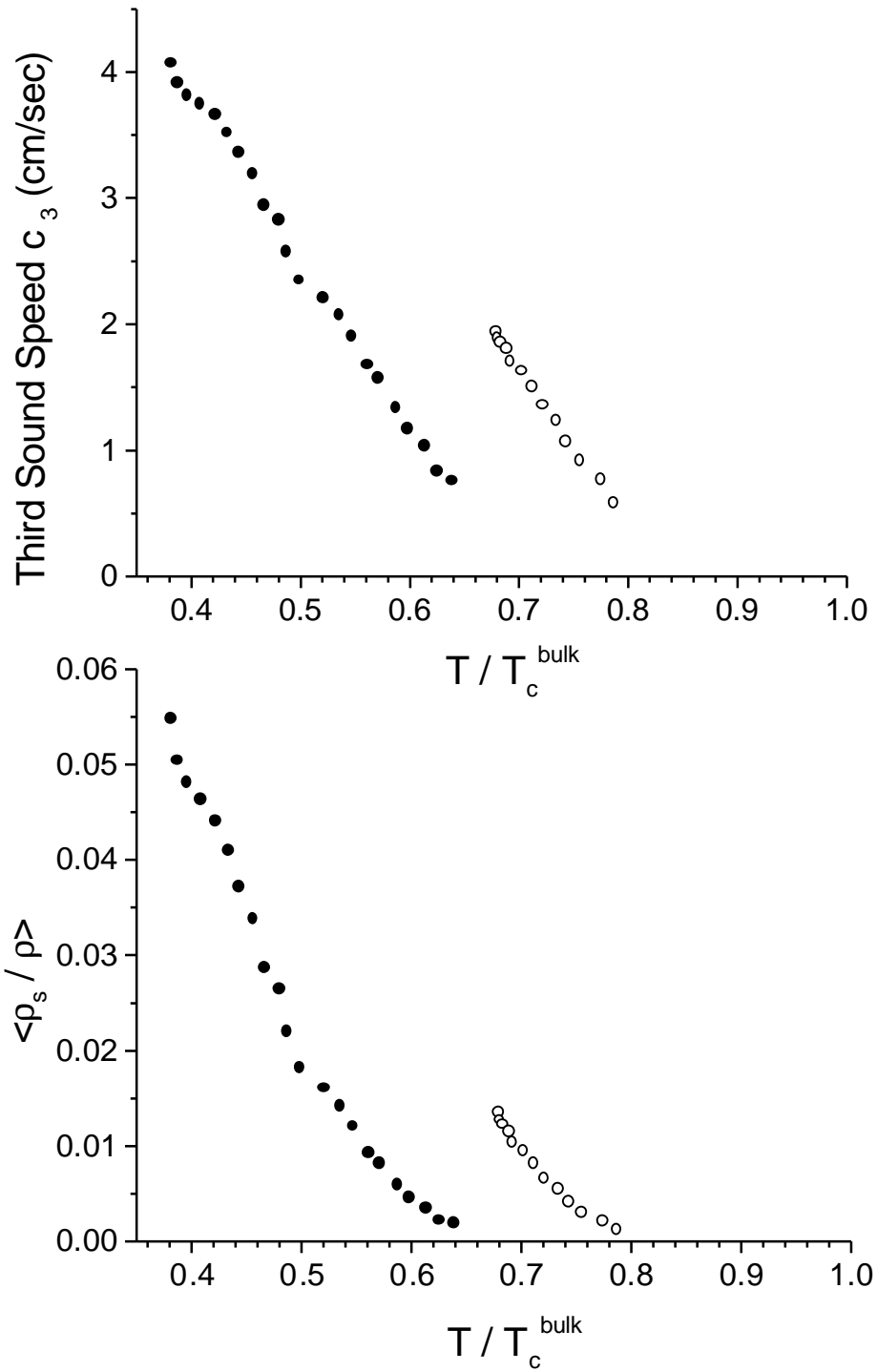


Figure 8.2 c_3 and ρ_s with and without ^4He coating. Third sound speed and average superfluid density, with the pure ^3He data the solid data on the left in each graph and the ^3He with ^4He coating data the hollow data points on the right in each graph.

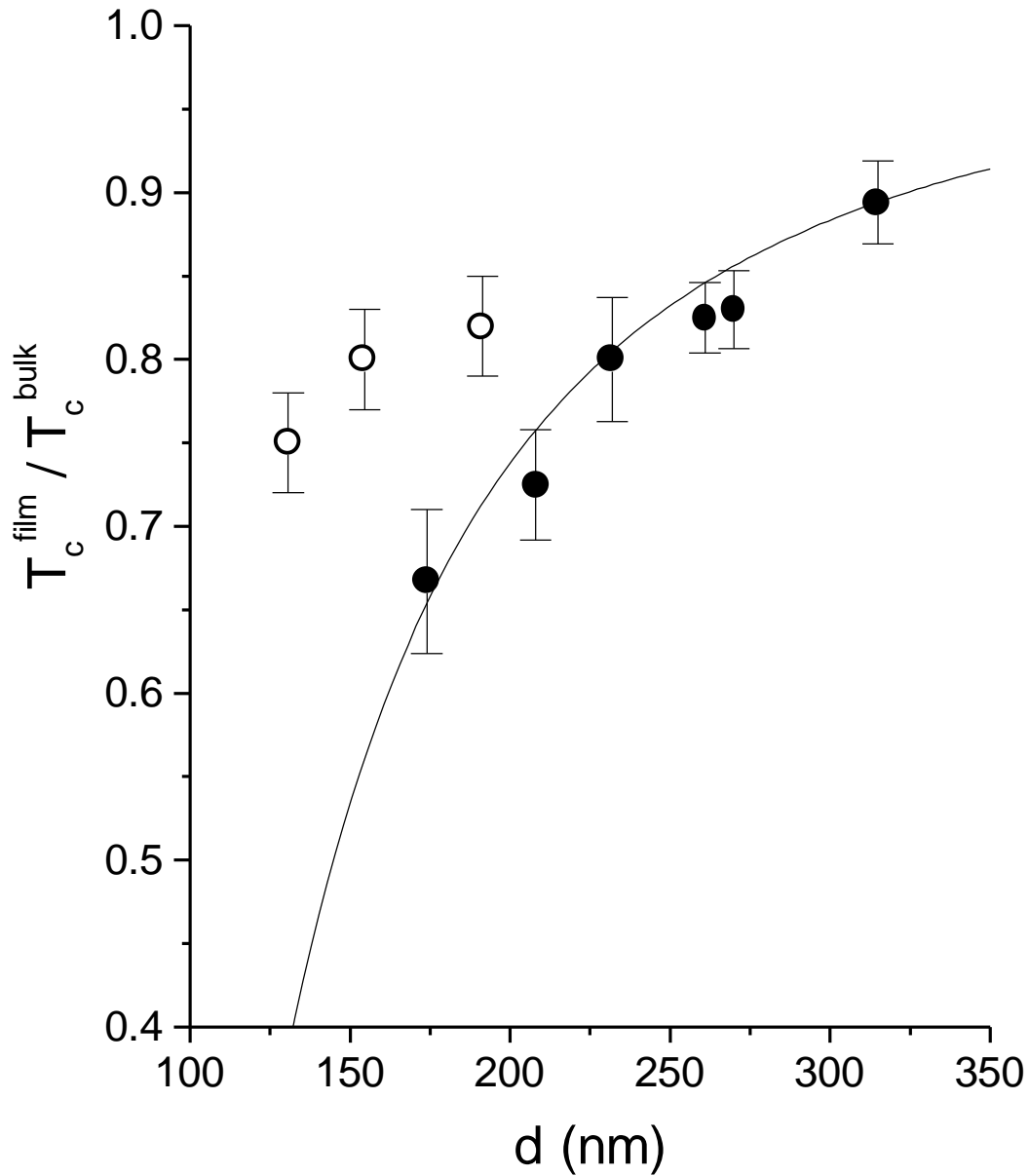


Figure 8.4 Superfluid transition temperature as a function of film thickness. The solid circles are pure ^3He films (with the film thickness estimated from measured values of h using the $n=3.44$ power law dependence between h and d discussed in Chapter 6). The hollow circles are for ^3He films with a ~ 2.5 monolayer coating of ^4He between the film and substrate. The solid line gives the Ginzburg-Landau prediction for T_c^{film} .

B. Swirling ^3He to observe 2D vortices.

As Ellis showed [Ellis and Li 1993], a circular third sound resonator can be used to create quantized vortices in ^4He films by "quantum swirling" of the fluid. Quantum swirling consists of using high-amplitude azimuthal third sound resonances to generate vortices which then remain in the film after the driving force has been removed. The existence of these vortices can be observed due to the Doppler effect which they exert on another azimuthal mode. As shown in Figure 8.5a, the vortices produce a net circulation of fluid around the rim of the substrate. This current causes two degenerate azimuthal modes of the system, one rotating clockwise and the other counter-clockwise, to be Doppler-shifted; hence the frequency shifts to these azimuthal modes measure the presence of vortices in the film. The frequency shift is given by

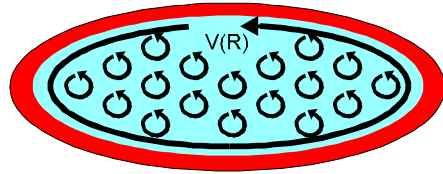
$$\Delta f / f = \gamma v(R) / c_3 \quad (8.1)$$

where γ is a number of order 1 (which varies for different modes) and $v(R)$ is the velocity at the rim caused by the circulation associated with the vortices in the film. This frequency shift for ^3He films should be quite large. Producing vortices in the film should not be a problem since critical velocities in ^3He tend to be a few cm/sec, about the speed of the third sound waves we would use to generate them, and the velocity at the rim would likewise be a few cm/sec, making the fractional frequency shift of order 1.

This experiment could be carried out in the present experimental cell, which has an appropriate circular geometry, with only slight modifications of the upper electrodes. The current plates would need to be replaced with an azimuthally-segmented one such as shown in Figure 8.5b, in order to optimally excite "swirling" azimuthal modes using phase-shifted sinusoidal drives.

This experiment would study the creation and decay of these fundamentally important two-dimensional objects, shedding light on the structure and dynamics of a 2-D superfluid permeated with topological defects. It is likely to provide important insights into the behavior of such systems, particularly their dissipation mechanisms, which is of especially great significance in the context of high- T_c superconductors.

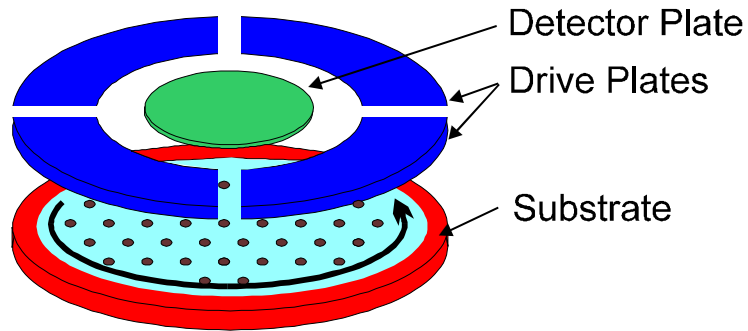
a



^3He Film with
n vortices

Resulting circulation:
 $V(R) = n\kappa_0/2\pi R$

b



Detector Plate

Drive Plates

Substrate

Figure 8.5 Swirling experiment. a) shows schematically how vortices in a ^3He film produce an azimuthal velocity at the perimeter, which then causes a frequency splitting of third sound modes. b) shows a detector/drive electrode configuration which would be appropriate for coupling to the azimuthal third sound modes needed in this experiment.

Bibliography

- [Ambegaokar *et al.* 1974] V. Ambegaokar, P.G. deGennes, and D. Rainer, "Landau-Ginsburg equations for an anisotropic superfluid." *Phys. Rev. A* **9**, 2676-2685 (1974). Erratum: *Phys. Rev. A* **12**, 345 (1975).
- [Atkins 1959] K.R. Atkins, "Third and Fourth Sound in Liquid Helium II." *Phys. Rev.* **113**, (no.4) 962-965, (1959).
- [Bardeen *et al.* 1957] J. Bardeen, L.N. Cooper, and J.R. Schrieffer, "Theory of Superconductivity." *Phys. Rev.* **108**, (no. 5) 1175-1204, (1957).
- [Barton and Moore 1975] G. Barton and M.A. Moore, "Superfluid ^3He in Restricted Geometries." *J. Low Temp. Phys.* **21**, (no.5/6) 489-515 (1975).
- [Backhaus 1998] S. Backhaus, personal communication, 1998.
- [Bauerle, *et al.* 1998] C. Bauerle, Yu.M. Bunkov, S.N. Fisher, H. Godfrin, and G.R. Pickett, "Superfluid ^3He simulation of cosmic string creation in the early universe." *J. Low Temp. Phys.* **110**, (no.1/2) 13-22 (1998).
- [Baym and Pethick 1978] G. Baym and C. Pethick, "Landau Fermi-Liquid Theory and Low Temperature Properties of Normal Liquid ^3He ." in *The Physics of Liquid and Solid Helium, Part II* edited by K.H. Bennemann and J.B. Ketterson (Wiley, New York, 1978).
- [Beelen and Bannink 1983] H. Van Beelen and G. Bannink, "Some Phenomenological Properties of Helium Films." *Physica* **121B**, 30-40 (1983).
- [Bergman 1969] D. Bergman, "Hydrodynamics and Third Sound in Thin He II Films." *Phys. Rev.* **188**, (no.1) 370-384, (1969).
- [Bergman 1971] D. Bergman, "Third Sound in Superfluid Helium Films of Arbitrary Thickness." *Phys. Rev. A* **3**, (no.6) 2058-2066, (1971).
- [Betts 1976] D.S. Betts, *Refrigeration and Thermometry below One Kelvin*, (Sussex University Press, Brighton, 1976).

- [Betts 1989] D.S. Betts, *An Introduction to Millikelvin Technology*, (Cambridge University Press, Cambridge, 1989).
- [Bishop and Reppy 1978] D.J. Bishop and J.D. Reppy, "Study of the Superfluid Transition in Two-Dimensional ^4He Films." *Phys. Rev. Lett.* **40**, (no.26) 1727-1730 (1978).
- [Brand and Cross 1982] H. Brand and M.C. Cross, "Explanation of Flow Dissipation in $^3\text{He-B}$." *Phys. Rev. Lett.* **49**, (no.26) 1959 (1982).
- [Brewer 1978] D.F. Brewer, "Multilayer Adsorbed Helium in Restricted Geometries." in *The Physics of Liquid and Solid Helium, Part II* edited by K.H. Bennemann and J.B. Ketterson (Wiley, New York, 1978).
- [Brisson *et al.* 1991] J.G. Brisson, J.C. Mester, and I.F. Silvera, "Third sound of helium on a hydrogen substrate." *Phys. Rev. B* **44**, (no.22) 12453-12462, (1991).
- [Brooks *et al.* 1978] J.S. Brooks, F.M. Ellis, and R.B. Hallock, "Direct Observation of Third-Sound Mass Displacement Waves in Unsaturated Superfluid ^4He Films." *Phys. Rev. Lett.* **40**, 240-243 (1978).
- [Brouwer *et al.* 1995] P.W. Brouwer, W.A. Draisma, H. van Beelen, and R. Jochemsen, "On the propagation of third sound in ^4He films." *Physica B* **215**, 135-152 (1995).
- [Buchholtz 1986] L.J. Buchholtz, "Fermi superfluids at a rough surface." *Phys. Rev. B* **33**, (no.3) 1579-1584 (1986).
- [Casimir and Polder 1948] H.B.G. Casimir and D. Polder, "The Influence of Retardation on the London - van der Waals Forces." *Phys. Rev.* **73**, (no.4) 360-372 (1948).
- [Cheng and Cole 1988] E. Cheng and M.W. Cole, "Retardation and many-body effects in multilayer-film adsorption." *Phys. Rev. B* **38**, (no.2) 987-995 (1988).
- [Cho and Williams 1995] H. Cho and G.A. Williams, "Vortex Core Size in Submonolayer Superfluid ^4He Films." *Phys. Rev. Lett.* **75**, (no.8) 1562-1565 (1995).
- [Cole *et al.* 1978] M.W. Cole, D.L. Goodstein, and D. Kwoh, "Electrohydrodynamic Instability in a Superthick

- Superfluid Film." *Journal de Physique* **39**, (no.8) C6: 318-319 (1978).
- [Cook *et al.* 1996] J.B. Cook, A.J. Manninen, and J.R. Hook, "First and second viscosity measurements in superfluid $^3\text{He-B}$." *Czech. J. Phys.* **46**, S1 57-58 (1996).
- [Corson *et al.* 1999] J. Corson, R. Mallozzi, J. Orenstein, J.N. Eckstein, and I. Bozovic, "Vanishing of phase coherence in underdoped $\text{Bi}_2\text{Sr}_2\text{CaCu}_2\text{O}_{8+\delta}$." *Nature* **398**, (no.6724), 221-223 (1999).
- [Crooker and Xu 1990] B.C. Crooker and J. Xu, "The Growth of Unsaturated Films of ^3He ." *J. Low Temp. Phys.* **79**, (no.1/2) 67-73 (1990).
- [Daunt *et al.* 1988] J.G. Daunt, R.F. Harris-Lowe, J.P. Harrison, A. Sachrajda, S. Steel, R.R. Turkington, and P. Zawadski, "Critical Temperature and Critical Current of Thin-Film Superfluid ^3He ." *J. Low Temp. Phys.* **70**, (no.5/6) 547-568 (1988).
- [Davis *et al.* 1987] J.C. Davis, A. Amar, J.P. Pekola, and R.E. Packard, "Observations on the Flow Properties of ^3He Films below 1 mK." *Jap. J. App. Phys.* **26**, 147-148, (1987).
- [Davis *et al.* 1988] J.C. Davis, A. Amar, J.P. Pekola, and R.E. Packard, "Superfluidity of ^3He Films." *Phys. Rev. Lett.* **60**, (no.4) 302-304, (1988).
- [Davis 1989] J.C. Davis, "Superfluid ^3He in Simple Restricted Geometries." Ph.D. Dissertation, University of California at Berkeley, 1989.
- [Dzyaloshinskii *et al.* 1961] I.E. Dzyaloshinskii, E.M. Lifshitz, and L.P. Pitaevskii, "The General Theory of Van der Waals Forces." *Adv. Phys.* **10**, 165-209, (1961).
- [Eggenkamp *et al.* 1998] M.E.W. Eggenkamp, V.A. Shvarts, R. Blaauwgeers, A. Storm, R. Jochemsen, and G. Frossati, "On the Possibility of Observing Third Sound in ^3He ." *J. Low Temp. Phys.* **110**, (no.1/2) 299-304 (1998).
- [Eggenkamp 1998] M.E.W. Eggenkamp, "Third Sound on ^3He and ^4He Films." Ph.D. Dissertation, University of Leiden, 1998.
- [Eisenstein, Packard 1982] J.P. Eisenstein and R.E. Packard, "Observation of Flow Dissipation in $^3\text{He-B}$." *Phys. Rev. Lett.* **49**, (no.8) 564-567 (1982).

- [Ekholm and Hallock 1980] D.T. Ekholm and R.B. Hallock, "Third sound and the decay of persistent currents in unsaturated ^3He - ^4He -mixture films." *Phys. Rev. B* **21**, (no.9) 3913-3916 (1980).
- [Ellis 1998] F.M. Ellis, personal communication, 1998.
- [Ellis *et al.* 1981a] F.M. Ellis, J.S. Brooks and R.B. Hallock, "Capacitive transient detector of high sensitivity." *Rev. Sci. Instr.* **52**, (no.7) 1051-1053, (1981).
- [Ellis *et al.* 1981b] F.M. Ellis, R.B. Hallock, M.D. Miller, and R.A. Guyer, "Phase Separation in Films of ^3He - ^4He Mixtures." *Phys. Rev. Lett.* **46**, (no.22) 1461-1464, (1981).
- [Ellis and Hallock 1983] F.M. Ellis and R.B. Hallock, "High-resolution third-sound resonator." *Rev. Sci. Instr.* **54**, (no.6) 751-753, (1983).
- [Ellis and Luo 1989] F.M. Ellis and H. Luo, "Observation of the persistent-current splitting of a third-sound resonator." *Phys. Rev. B* **39**, (no.4) 2703-2706 (1989).
- [Ellis and Luo 1992] F.M. Ellis and H. Luo, "Third sound: Where are the solitons?" *J. Low. Temp. Phys.* **89**, (no.1/2) 115-124 (1992).
- [Ellis and Li 1993] F.M. Ellis and L. Li, "Quantum Swirling of Superfluid Helium Films." *Phys. Rev. Lett.* **71**, (no.10) 1577-1580, (1993).
- [Everitt *et al.* 1962] C.W.F. Everitt, K.R. Atkins, and A. Denenstein, "Detection of Third Sound in Liquid Helium Films." *Phys. Rev. Lett.* **8**, (no.4) 161-163 (1962).
- [Everitt *et al.* 1964] C.W.F. Everitt, K.R. Atkins, and A. Denenstein, "Third Sound in Liquid Helium Films." *Phys. Rev.* **136**, (no.6A) 1494-1499 (1964).
- [Fehl and Dillinger 1974] D.L. Fehl and J.R. Dillinger, "Thickness of the He II film on copper versus surface roughness and saturation." *Phys. Lett. A* **49A**, (no.3) 243-245 (1974).
- [Fetter and Ullah 1988] A.L. Fetter and S. Ullah, "Superfluid Density and Critical Current of ^3He in Confined Geometries." *J. Low Temp. Phys.* **70**, 515-535 (1988).

- [Freeman *et al.* 1988] M.R. Freeman, R.S. Germain, E.V. Thuneberg, R.C. Richardson, "Size effects in thin films of superfluid ^3He ." *Phys. Rev. Lett.* **60**, 596-599 (1988).
- [Freeman 1988] M.R. Freeman, "Size effects in ^3He films." Ph.D. Dissertation, Cornell University, August 1988.
- [Freeman 1990] M.R. Freeman and R.C. Richardson, "Size effects in superfluid ^3He films." *Phys. Rev. B* **41**, (no.16) 11011-11028, (1990).
- [Galkiewicz *et al.* 1977] R.K. Galkiewicz, K.L. Telschow, and R.B. Hallock, "Persistent Currents in Saturated Superfluid ^4He Films on Rough Surfaces in the Presence of Third-Sound Resonances." *J. Low Temp. Phys.* **26**, (no.1/2) 147-163 (1977).
- [Gammel *et al.* 1984] P.L. Gammel, H.E. Hall, and J.D. Reppy, "Persistent Currents in Superfluid $^3\text{He-B}$." *Phys. Rev. Lett.* **52**, (no.2) 121-124 (1984).
- [Gammel *et al.* 1985] P.L. Gammel, T.-L. Ho, and J.D. Reppy, "Persistent Currents and Dissipation in the A and B Phases of Liquid ^3He ." *Phys. Rev. Lett.* **55**, (no.24) 2708-2711 (1985).
- [Gor'kov 1959] L.P. Gor'kov, "Microscopic Derivation of the Ginzburg-Landau Equations in the Theory of Superconductivity." *Sov. Phys. JETP* **9**, (no.6) 1364-69 (1959).
- [Greywall 1986] D.S. Greywall, " ^3He specific heat and thermometry at millikelvin temperatures." *Phys. Rev. B* **33**, 7520 (1986).
- [Harrison 1979] J.P. Harrison, "Review Paper: Heat Transfer Between Liquid Helium and Solids Below 100 mK." *J. Low Temp. Phys.* **37**, (no.5/6) 467-565 (1979).
- [Harrison *et al.* 1991] J.P. Harrison, A. Sachrajda, S.C. Steel, and P. Zawadski, "The Effect of Film Thickness and the Substrate on Superfluid ^3He Film Flow." in *Excitations in Two-Dimensional and Three-Dimensional Quantum Fluids*, ed. by A.G.F. Wyatt and H.J. Lauter (Plenum, New York, 1991)
- [Hoffberg *et al.* 1970] M. Hoffberg, A.E. Glassgold, R.W. Richardson, and M. Ruderman, "Anisotropic superfluidity in neutron star matter." *Phys. Rev. Lett.* **24** (no.14) 775-775 (1970).

- [Hook *et al.* 1994] J.R. Hook, T.D.C. Bevan, A.J. Manninen, J.B. Cook, A.J. Armstrong, and H.E. Hall, "Diaphragm-driven flow in rotating superfluid $^3\text{He-B}$." *Physica B* **210**, 251-266 (1995).
- [Jacobsen and Smith 1987] K.W. Jacobsen and H. Smith, "Critical Current for the Flow of Superfluid ^3He in a Confined Geometry." *J. Low Temp. Phys.* **67**, 83-89 (1987).
- [Jiang and Kojima 1992] Jiang and Kojima, "Magnetic relaxation and ^4He coverage in $^3\text{He-A}_1$." *Phys. Rev. B* **45**, (no.21) 12616-19 (1992).
- [Kagiwada *et al.* 1969] R.S. Kagiwada, J.C. Fraser, and I. Rudnick, "Superflow in Helium Films: Third-Sound Measurements." *Phys. Rev. Lett.* **22**, (no.8) 338-342 (1969).
- [Kawae *et al.* 1998] T. Kawae, M Kubota, Y. Ishimoto, S. Miyawaki, O. Ishikawa, T. Hata, and T. Kodama, "A-B Transition of Superfluid ^3He with a Film Geometry." *J. Low Temp. Phys.* **111**, (no.5/6) 917-935 (1998).
- [Khalatnikov 1989] I.M. Khalatnikov, *An Introduction to the Theory of Superfluidity*, (Addison-Wesley, Redwood City, California, 1989).
- [Kim *et al.* 1993] D. Kim, M. Nakagawa, O. Ishikawa, T. Hata, T. Kodama, and H. Kojima, "Boundary Condition on Superfluid ^3He as altered by ^4He Interfacial Layer." *Phys. Rev. Lett.* **71**, (no.10) 1581-1584 (1993).
- [Kjaldman *et al.* 1978] L.H. Kjaldman, J. Kurkijarvi, and D. Rainer, "Suppression of P-Wave Superfluidity in Long, Narrow Pores." *J. Low Temp. Phys.* **33**, 577-587 (1978).
- [Kosterlitz, Thouless 1973] J.M. Kosterlitz and D.J. Thouless, "Ordering, metastability, and phase transitions in two-dimensional systems." *J. Phys. C* **6**, 1181-1203 (1973).
- [Kurihara 1983] S. Kurihara, "Singlet Superfluidity in ^3He Film on ^4He Film." *J. Phys. Soc. Jap.* **52**, (no.4) 1311-1316 (1983).
- [Landau, Lifshitz 1959] L.D. Landau and E.M. Lifshitz, *Fluid Mechanics*, (Pergamon Press, Oxford, 1959).

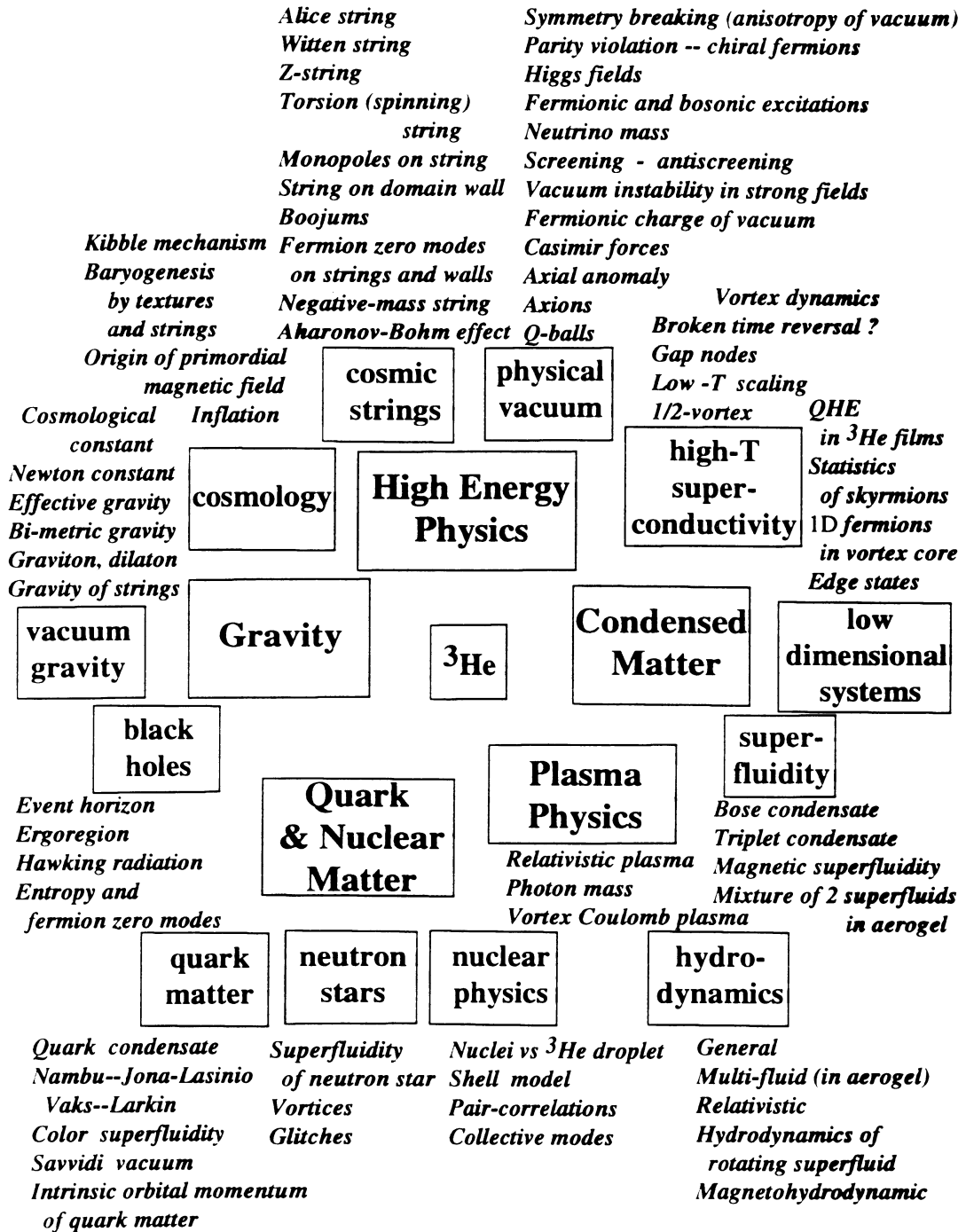
- [Lee 1997] D.M. Lee, "The extraordinary phases of liquid ^3He ." *Rev. Mod. Phys.* **69**, (no.3) 645-665 (1997).
- [Lee and Richardson 1978] D.M. Lee and R.C. Richardson, "Superfluid ^3He ." in *The Physics of Liquid and Solid Helium, Part II* edited by K.H. Bennemann and J.B. Ketterson (Wiley, New York, 1978).
- [Li and Ho 1988] Y.-H. Li and T.-L. Ho, "Superfluid ^3He in very confined regular geometries." *Phys. Rev. B* **38**, 2362-2370 (1988).
- [Lounasmaa 1974] O.V. Lounasmaa, *Experimental Principles and Methods Below 1K*, (Academic Press, London, 1974).
- [Nelson, Kosterlitz 1977] D.R. Nelson and J.M. Kosterlitz, "Universal Jump in the Superfluid Density of Two-Dimensional Superfluids." *Phys. Rev. Lett.* **39**, (no.19) 1201-1205.
- [Manninen, Pekola 1982] M.T. Manninen and J.P. Pekola, "Flow of $^3\text{He-B}$ through narrow channels." *Phys. Rev. Lett.* **48**, (no.12) 812-816 (1982).
- [Mermin, Muzikar 1980] N.D. Mermin and P. Muzikar, "Cooper pairs vs Bose condensed molecules: The ground-state current in superfluid $^3\text{He-A}$." *Phys. Rev. B* **21**, (no.3) 980-989 (1980).
- [Morse and Ingard 1968] P.M. Morse and K.U. Ingard, *Theoretical Acoustics*, (McGraw-Hill, New York, 1968).
- [Osheroff *et al.* 1972] D.D. Osheroff, R.C. Richardson, and D.M Lee, "Evidence for a new phase of solid ^3He ." *J. Low Temp. Phys.* **79**, (no.1/2) 67-73 (1990).
- [Osheroff 1997] D.D. Osheroff, "Superfluidity in ^3He : discovery and understanding." *Rev. Mod. Phys.* **69**, 667-681 (1997).
- [Pekola *et al.* 1984] J.P. Pekola, J.T. Simola, K.K. Nummila, O.V. Lounasmaa, and R.E. Packard, "Persistent-current experiments on superfluid $^3\text{He-B}$ and $^3\text{He-A}$." *Phys. Rev. Lett.* **53**, (no.1) 70-73 (1984).
- [Pekola *et al.* 1987] J.P. Pekola, J.C. Davis, Zhu Yu-Qun, R.N.R. Spohr, P.B. Price, R.E. Packard, "Suppression of the Critical Current and the Superfluid Transition Temperature of ^3He in a Single Submicron Cylindrical Channel." *J. Low Temp. Phys.* **67**, (no.1/2) 47-63 (1987).

- [Pereverzev *et al.* 1997] S.V. Pereverzev, A. Loshak, S. Backhaus, J.C. Davis, R.E. Packard, "Quantum oscillations between two weakly coupled reservoirs of superfluid ^3He ." *Nature* **388** (no. 6641) 449-51, (1997)
- [Pickar and Atkins 1969] K.A. Pickar and K.R. Atkins, "Critical Velocity of a Superflowing Liquid-Helium Film Using Third Sound." *Phys. Rev.* **178**, (no.1) 389-402, (1969).
- [Pines and Alpar 1985] D. Pines and M.A. Alpar, "Superfluidity in neutron stars." *Nature* **316**, (no.6023) 27-32 (1985).
- [Pobell 1992] F. Pobell, *Matter and Methods at Low Temperatures*, (Springer-Verlag, Berlin, 1992).
- [Poole *et al.* 1995] C.P. Poole, Jr., H.A. Farach, R.J. Creswick, *Superconductivity*, (Academic Press, San Diego, 1995).
- [Ratnam and Mochel 1970] B. Ratnam and J. Mochel, "Third-sound resonance." *Phys. Rev. Lett.* **25**, (no.11) 711-714 (1970).
- [Richardson 1997] R.C. Richardson, "The Pomeranchuk effect." *Rev. Mod. Phys.* **69**, (no.3) 683-90, 1997.
- [Roche *et al.* 1997] P. Roche, G. Deville, N.J. Appleyard, and F.I.B. Williams, "Measurement of the surface tension of superfluid ^4He at low temperature by capillary wave resonances." *J. Low Temp. Phys.* **106**, (no.5/6) 565-573 (1997).
- [Rudnick *et al.* 1968] I. Rudnick, R.S. Kagiwada, J.C. Fraser, and E. Guyon. *Phys. Rev. Lett.* **20**, 430 (1968).
- [Rudnick 1978] I. Rudnick, "Critical Surface Density of the Superfluid Component in ^4He Films." *Phys. Rev. Lett.* **40**, (no.22) 1454-1455 (1978).
- [Sabisky, Anderson 1973] E.S. Sabisky and C.H. Anderson, "Verification of the Lifshitz Theory of the van der Waals Potential Using Liquid-Helium Films." *Phys. Rev. A* **7**, (no.2) 790-806, (1973).
- [Sachrajda *et al.* 1985] A. Sachrajda, R.F. Harris-Lowe, J.P. Harrison, R.R. Turkington, J.G. Daunt, " ^3He film flow: two-dimensional superfluidity." *Phys. Rev. Lett.* **55**, 1602-1605 (1985).

- [Schechter *et al.* 1998a] A.M.R. Schechter, R.W. Simmonds, and J.C. Davis, "Capacitive generation and detection of third sound resonances in saturated superfluid ^4He films." *J. Low Temp. Phys.* **110**, 603-608, (1998).
- [Schechter *et al.* 1998b] A.M.R. Schechter, R.W. Simmonds, R.E. Packard, J.C. Davis, "Observation of 'third sound' in superfluid ^3He ." *Nature* **396**, 554-557, (1998).
- [Serene and Rainer 1978] J.W. Serene and D. Rainer, "Response theory for superfluid ^3He ." *Phys. Rev. B* **17**, (no.7) 2901-2914, (1978).
- [Sheldon and Hallock 1994] P.A. Sheldon and R.B. Hallock, "Third sound and energetics in ^3He - ^4He mixture films." *Phys. Rev. B* **50**, (no.21) 16082-16085 (1994).
- [Shirron and Mochel 1991] P.J. Shirron and J.M. Mochel, "Atomically Thin Superfluid Helium Films on Solid Hydrogen." *Phys. Rev. Lett.* **67**, (no.9) 1118-1121 (1991).
- [Steel *et al.* 1994] S.C. Steel, J.P. Harrison, P. Zawadski, and A. Sachrajda, " ^3He Film Flow on a Round Rim Beaker." *J. Low Temp. Phys.* **95**, (no.5/6) 759-788 (1994).
- [Swift 1980] G.W. Swift, "A measurement of the anisotropy of the dielectric constant of ^3He -A." Ph.D. Dissertation, University of California at Berkeley, 1980.
- [Tesanovic and Valls 1986] Z. Tesanovic and O.T. Valls, "Quantum size effects in superfluid ^3He films." *Phys. Rev. B* **33**, 3139-3145 (1986).
- [Tholen and Parpia 1991] S.M. Tholen and J.M. Parpia, "Slip and the Effect of ^4He at the ^3He -Silicon Interface." *Phys. Rev. Lett.* **67**, (no.3) 334-337, (1991).
- [Tholen and Parpia 1992] S.M. Tholen and J.M. Parpia, "Hysteretic Solidification of Surface ^4He Measured by the Modification of the Specularity of ^3He ." *Phys. Rev. Lett.* **68**, (no.18) 2810-2813, (1992).
- [Thuneberg 1987] E.V. Thuneberg, "Ginzburg-Landau theory of vortices in superfluid ^3He -B." *Phys. Rev. B* **36**, (no.7) 3583-3597, (1987).
- [Tilley and Tilley 1986] D.R. Tilley and J. Tilley, *Superfluidity and Superconductivity*, (Hilger, Bristol, 1986).

- [Van Harlingen 1995] D.J. van Harlingen, "Phase-sensitive tests of the symmetry of the pairing state in the high-temperature superconductors - Evidence for $d(x^2-y^2)$ symmetry." *Rev. Mod. Phys.* **67**, (no.2) 515-535 (1995).
- [Vollhardt and Wolfle 1990] D. Vollhardt and P. Wolfle, *The Superfluid Phases of Helium 3*, (Taylor & Francis, London, 1990).
- [Volovik 1988a] G.E. Volovik, "Quantized Hall Effect in Superfluid Helium-3 Film." *Phys. Lett. A* **128**, (no.5) 277-279 (1988).
- [Volovik 1988b] G.E. Volovik, "An analog of the quantum Hall Effect in a superfluid ^3He film." *Sov. Phys. JETP* **67**, 1804-1811 (1988).
- [Volovik 1989] G.E. Volovik, "Fractional statistics and analogs of quantum Hall effect in superfluid ^3He film." AIP Conference Proceedings (no.194) (Quantum Fluids and Solids - 1989) 136-146 (1989).
- [Volz *et al.* 1985] S. Volz, K. Gillis, J.M. Mochel, "Plastic third sound resonator and low-temperature pressure gauge." *Rev. Sci. Inst.* **56**, (no.3) 444-448 (1985).
- [Wheatley 1975] J.C. Wheatley, "Experimental properties of superfluid ^3He ." *Rev. Mod. Phys.* **47**, (no.2), 415-470 (1975).
- [Wilson and Ellis 1995] C. Wilson and F.M. Ellis, "Vortex Creation and Pinning in High Amplitude Third Sound Waves." *J. Low Temp. Phys.* **101**, (no.3/4) 507-512 (1995).
- [Xu 1991] J. Xu, "Superfluidity in Thin ^3He Films." Ph.D. Dissertation, Purdue University, 1991.
- [Xu and Crooker 1990] J. Xu and B.C. Crooker, "Very thin films of ^3He : a new phase?" *Phys. Rev. Lett.* **65**, 3005-3008, (1990).
- [Zieve 1992] R.J. Zieve, "A Study of Superfluid ^3He Dynamics Using a Vibrating Wire Probe: Circulation, Vortex Precession, Depairing, and Textural Dissipation." Ph.D. Dissertation, University of California at Berkeley, 1992.

Appendix A. G.E. Volovik's ³Helio-centric Universe



Appendix B. Mathcad model calculation

